NAVAL POSTGRADUATE SCHOOL

MONTEREY, CALIFORNIA

THESIS

CLOSED LOOP CONTROL OF A CASCADED MULTI-LEVEL CONVERTER TO MINIMIZE HARMONIC DISTORTION

by

Brian E. Souhan

June 2005

Thesis Advisor: Robert W. Ashton
Second Reader: Alexander Julian

Approved for public release; distribution is unlimited

THIS PAGE INTENTIONALLY LEFT BLANK

REPORT DOCUMENTATION PAGE		*Form Approved OMB No. 0704-0188*

Public reporting burden for this collection of information is estimated to average 1 hour per response, including the time for reviewing instruction, searching existing data sources, gathering and maintaining the data needed, and completing and reviewing the collection of information. Send comments regarding this burden estimate or any other aspect of this collection of information, including suggestions for reducing this burden, to Washington headquarters Services, Directorate for Information Operations and Reports, 1215 Jefferson Davis Highway, Suite 1204, Arlington, VA 22202-4302, and to the Office of Management and Budget, Paperwork Reduction Project (0704-0188) Washington DC 20503.

1. AGENCY USE ONLY (*Leave blank*)	2. REPORT DATE June 2005	3. REPORT TYPE AND DATES COVERED Master's Thesis	
4. TITLE AND SUBTITLE: Closed Loop Control of a Cascaded Multi-Level Converter to Minimize Harmonic Distortion		5. FUNDING NUMBERS	
6. AUTHOR(S) Brian E. Souhan			

7. PERFORMING ORGANIZATION NAME(S) AND ADDRESS(ES)
    Naval Postgraduate School
    Monterey, CA 93943-5000
		8. PERFORMING ORGANIZATION REPORT NUMBER	

9. SPONSORING /MONITORING AGENCY NAME(S) AND ADDRESS(ES) N/A		10. SPONSORING/MONITORING AGENCY REPORT NUMBER	

11. SUPPLEMENTARY NOTES The views expressed in this thesis are those of the author and do not reflect the official policy or position of the Department of Defense or the U.S. Government.

12a. DISTRIBUTION / AVAILABILITY STATEMENT Approved for public release; distribution is unlimited	12b. DISTRIBUTION CODE

13. ABSTRACT (maximum 200 words)

As the United States Navy moves toward the all-electric ship, the need for a robust, high fidelity inverter for propulsion motors becomes mandatory. Military vessels require high power converters capable of producing nearly sinusoidal outputs to prevent torque pulsations and electrical noise that can compromise the mission location. This thesis presents a hybrid pulse-width-modulated controller for a 3x3 Cascaded Multi-Level Converter (CMLC). Ancillary results include a simple technique for extracting the reference sine wave from an independent bulk converter and implementing a synchronization technique that coordinates a space vector modulation controller with the switching pattern of a bulk inverter. The algorithms were tested on CMLC hardware that resides in the Naval Postgraduate School Power Systems Laboratory, and the results were compared with a sine-triangle pulse width modulation algorithm. The controller and converter were used to power a quarter-horsepower three-phase induction motor.

14. SUBJECT TERMS Cascaded Multi-Level Converter, Space Vector Modulation, Sine-Triangle Pulse Width Modulation, Neutral Point Clamped, Digital Phase-Locked Loop, Uncoupled Control, DD(X), dSPACE, Integrated Power System, All Electric Ship, Electric Propulsion.			15. NUMBER OF PAGES 105
			16. PRICE CODE
17. SECURITY CLASSIFICATION OF REPORT Unclassified	18. SECURITY CLASSIFICATION OF THIS PAGE Unclassified	19. SECURITY CLASSIFICATION OF ABSTRACT Unclassified	20. LIMITATION OF ABSTRACT UL

NSN 7540-01-280-5500

THIS PAGE INTENTIONALLY LEFT BLANK

**CLOSED LOOP CONTROL OF A CASCADED MULTI-LEVEL CONVERTER
TO MINIMIZE HARMONIC DISTORTION**

Brian E. Souhan
Captain, United States Army
B.S., University of Cincinnati, 1997

Submitted in partial fulfillment of the
requirements for the degree of

MASTER OF SCIENCE IN ELECTRICAL ENGINEERING

from the

**NAVAL POSTGRADUATE SCHOOL
June 2005**

Author: Brian E. Souhan

Approved by: Robert W. Ashton
                 Thesis Advisor

                 Alexander Julian
                 Second Reader

                 John P. Powers
                 Chairman, Department of Electrical and Computer Engineering

THIS PAGE INTENTIONALLY LEFT BLANK

ABSTRACT

As the United States Navy moves toward the all-electric ship, the need for a robust, high fidelity inverter for propulsion motors becomes mandatory. Military vessels require high power converters capable of producing nearly sinusoidal outputs to prevent torque pulsations and electrical noise that can compromise the mission location. This thesis presents a hybrid pulse-width-modulated controller for a 3x3 Cascaded Multi-Level Converter (CMLC). Ancillary results include a simple technique for extracting the reference sine wave from an independent bulk converter and implementing a synchronization technique that coordinates a space vector modulation controller with the switching pattern of a bulk inverter. The algorithms were tested on CMLC hardware that resides in the Naval Postgraduate School Power Systems Laboratory, and the results were compared with a sine-triangle pulse width modulation algorithm. The controller and converter testing was done on a quarter-horsepower three-phase induction motor.

THIS PAGE INTENTIONALLY LEFT BLANK

TABLE OF CONTENTS

LIST OF FIGURES

LIST OF TABLES

THIS PAGE INTENTIONALLY LEFT BLANK

EXECUTIVE SUMMARY

With the commercial maritime industry already making the switch to all electric drive systems, the U.S. Navy has become increasingly interested in the technology. With positive results from past research projects such as the Integrated Power System (IPS) and the DD(X) program, the U.S. Navy is continuing to invest heavily into the development of electric drive technologies.

All power produced aboard an all-electric ship design is in the form of electrical energy. The current standard for ship design is the production of both electrical and mechanical energy. The mechanical energy is used to propel the ship while the electrical energy is used to power all the shipboard systems. An electric ship instead uses an electric drive system to propel the ship, powered by high power, high fidelity converters. The high power, high fidelity converter is a major portion of the electric ship design. This converter is not available from the technological advances in the commercial maritime industry since the commercial industry does not have a requirement for a high fidelity system.

Cascaded Multi-Level Converters (CMLC) offer a promising new avenue to meet the U.S. Navy's need for a high power, high fidelity converter. A CMLC consists of the load connected between two multi-level inverters as shown in Figure E-1.
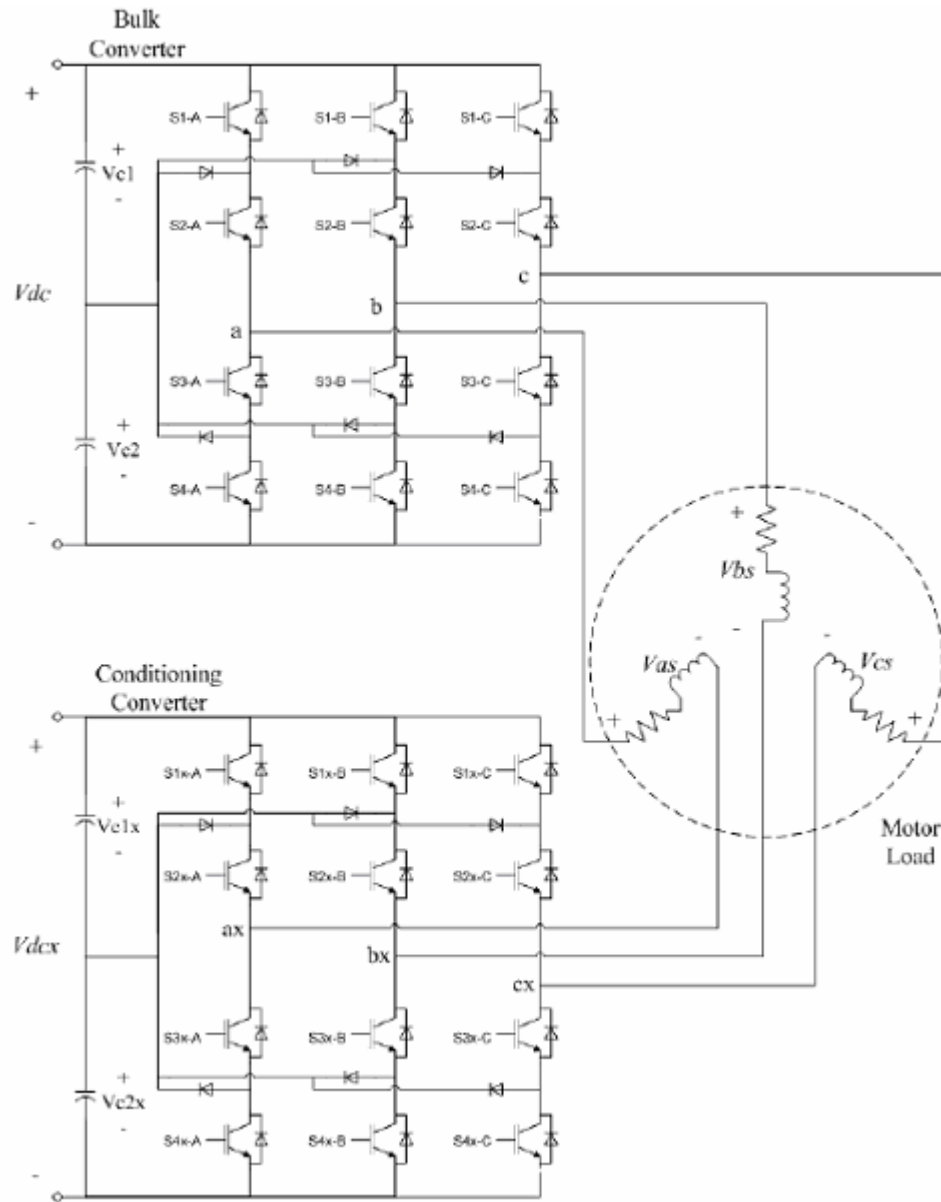
Figure E-1.   3x3 CMLC

Each inverter produces a specified voltage, and the difference between the upper and lower inverter is the voltage applied to the load.

There are two primary techniques to control a CMLC. The first technique is treating the two voltage inverters as one singular unit, and controlling them accordingly. Numerous techniques have been explored to control the inverters jointly, including Space Vector Modulation (SVM), Sine triangle Pulse Width Modulation (SPWM), and funda-

mental frequency control. In addition, control techniques have been introduced which allow for the elimination of the secondary inverter power supply.

The other promising technique that is being explored is uncoupled control of the two inverters. In this technique, the upper converter is controlled as a separate bulk inverter using fundamental frequency switching control, producing a three-level staircase wave from as shown in Figure E-2.
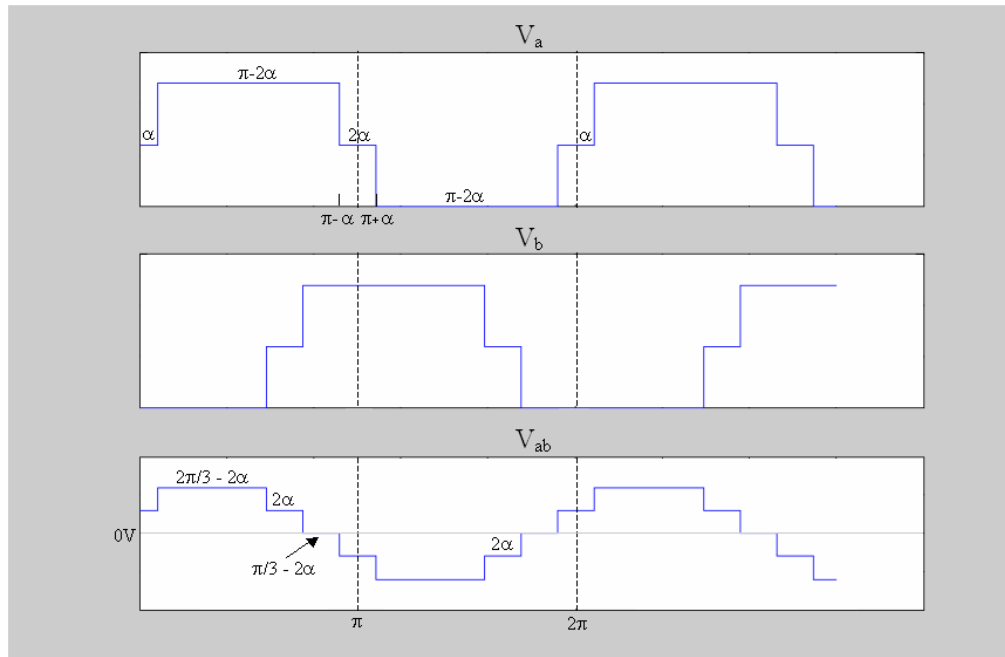
Figure E-2. $V_{dc} = 120$ V for Simulation

The bulk converter provides the high power density, but generates high harmonic content. Commercial drives have been using this technology for electronic propulsion and made many advances. This allows the U.S. Navy to use a Commercial-Off-The-Shelf (COTS) unit, saving cost and design time.

To eliminate the high harmonics from the bulk waveform, the second, lower (conditioning) inverter is used as an active harmonic filter. The second inverter takes the harmonics from the upper inverter and subtracts them out of the waveform. This produces a very clean sinusoidal waveform as show in Figure E-3a and E-3b.
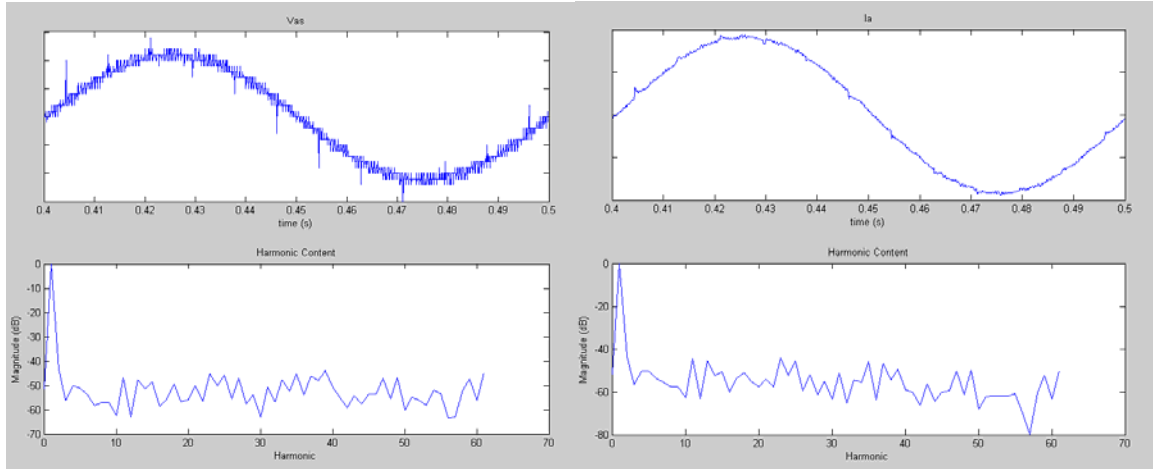
(a)   (b)

Figure E-3.   (a) Output Voltage and (b) Output Current for 3x3 CMLC Simulations

Figure E-3(a) shows the line-to-neutral voltage produced by the combined operation of the two inverters. The voltage spikes are a consequence of controlling the two inverters separately, and can be reduced in total duration by a faster DSP. Figure E-3(b) shows the current for a 12-Ω, 6.6-mH RL load.

Final hardware testing showed excellent results. Figure E-4(a) and E-4(b) show the hardware results for a single phase of the inverter. Figure E-4(a) shows the voltage waveform along with the harmonic content for the first 60 harmonics, and Figure E-4(b) shows a single phase current along with its harmonic content.
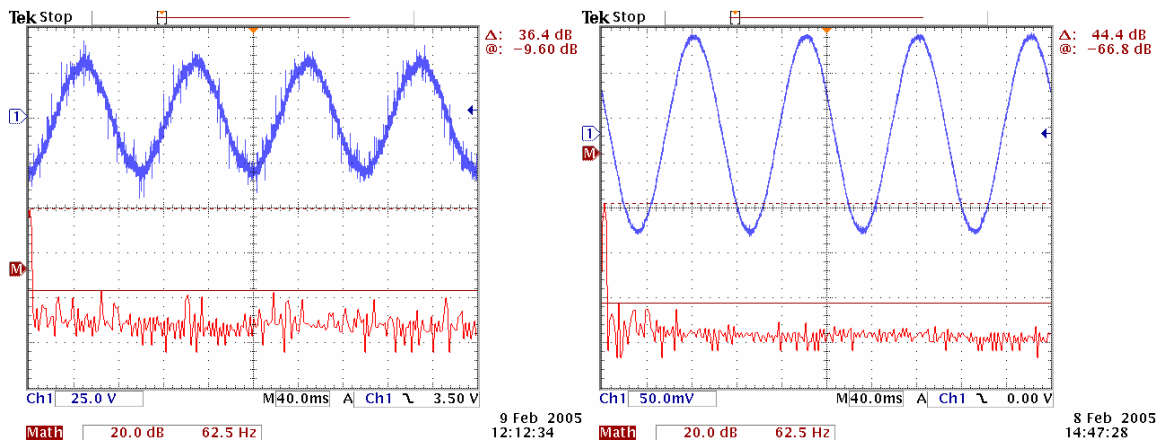
Figure E-4.   (a) Voltage and (b) Current Hardware Test Results with 1/4-HP Three-Phase Induction Motor

The results in Figure E-4 show exceptional performance. The highest harmonic content of the current waveform is over 44 dB less than the fundamental, resulting in a high fidelity current output. The THD for the current was found to be 1.74%.

THIS PAGE INTENTIONALLY LEFT BLANK

I.   INTRODUCTION

A.   NAVAL POWER

Before World War II, most naval vessels were electric drive because of the difficulty in manufacturing high quality gears. However, as manufacturing processes improved and shaft power requirements increased, mechanical drive systems became more advantageous. Currently we are on the cusp of a switch back to electrical from mechanical, but this time for the following reasons:

- Unlock propulsion power for other ship systems (e.g., pulse weapons)
- More efficient power utilization (matches power plant to load)
- Eliminate gearing with direct-drive motors.

The current switch to electric drive systems is being driven less by a lack of quality mechanical drives, and more by the increased electrical power needs of today's destroyers. Future U.S. Navy power applications include pulse weapon systems and ElectroMagnetic Aircraft Launch and Recovery Systems (EMALS and EARS). These loads would easily overwhelm the current ship-service (or hotel) buses on destroyers [1]. Further, incorporating unique dedicated generators for each application may cause the ship to miss its weight and volume targets and become cost prohibitive [1]. Currently, up to 80% of a destroyer's power generation is locked in the mechanical propulsions system. By switching to all-electric propulsion, the ship's propulsion power can also be used for the high power electrical loads. It is important to note that the ship propulsion power is related approximately to the cube of speed [2]. This translates into the ship only using 12% of its total propulsion power when cruising at half speed [2], freeing up the other 88% for high power application use.

Figure 1 depicts the increase in power generation capability in U.S. Navy Destroyers over time. Despite the 1000% growth in power generation since the end of World War II, available power aboard destroyers is still insufficient to supply even a single 30-MW advanced weapon system or launch.

US Navy Destroyers
Installed Electric Generating Capacity
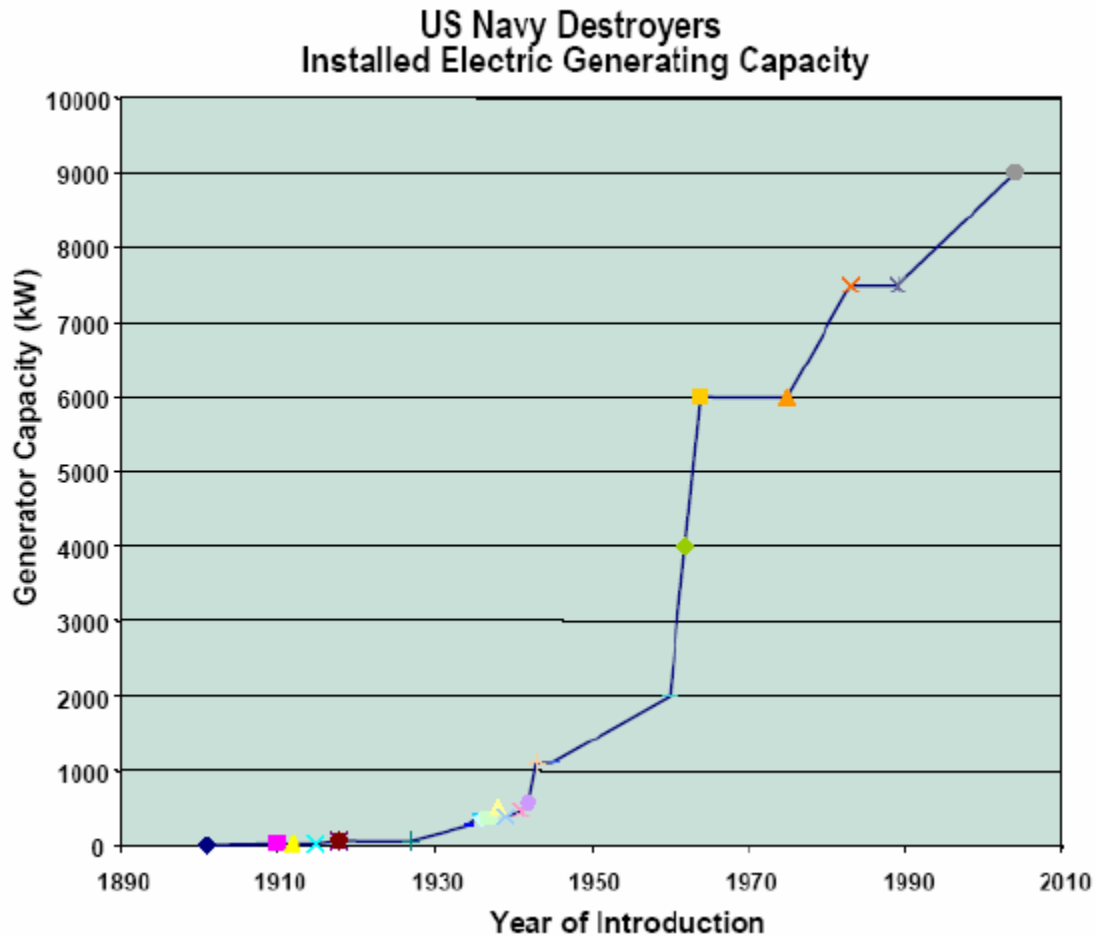
Figure 1.   Electric Power Generating Capacity [From Ref. 3.]

Another major benefit of switching to an Electric Propulsion Drive System
(EPDS) is the ability to more closely match the power generation with the actual power
required by the load. Although unpodded electric drive systems tend to be less efficient
then their comparable mechanical systems, they are still capable of reduced fuel require-
ments due to a better power utilization curve. This is illustrated in Figure 2, which shows
the Integrated Power System (IPS) propulsion power requirements verses speed. The IPS
power plant consists of two Auxiliary Turbine Generators (ATG) and two Main Turbine
Generators (MTG). The generators are only operated when needed as shown in Figure 2.

2
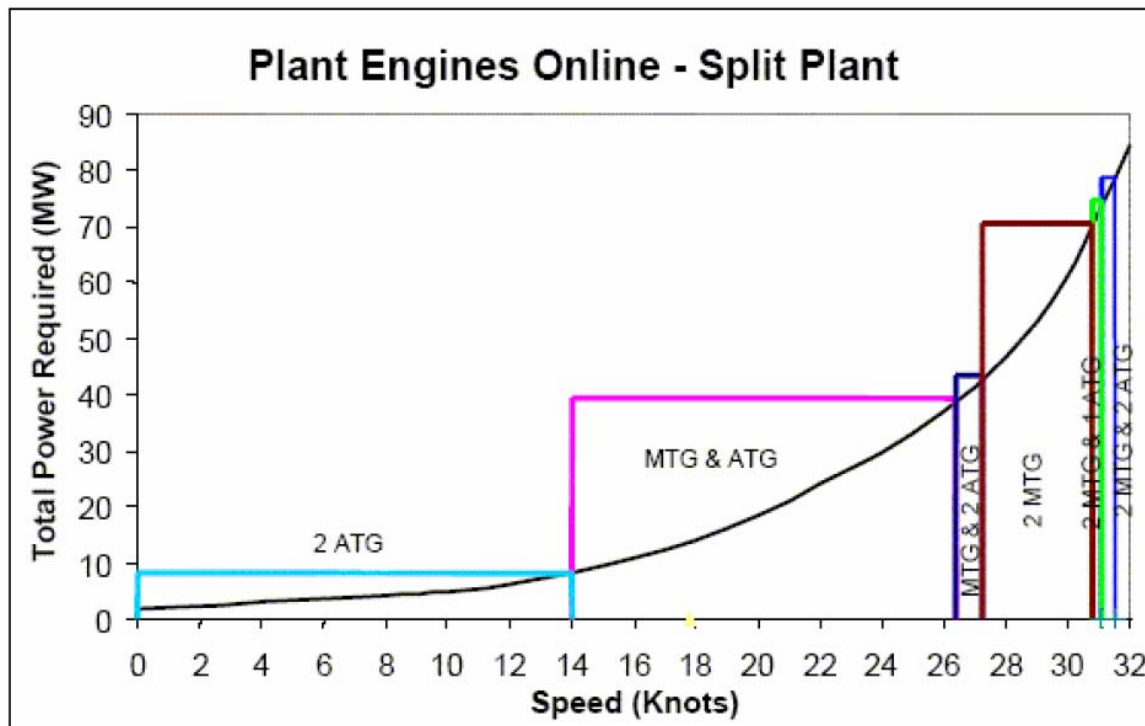
Figure 2. Propulsion Power Requirements vs. Speed [From Ref. 3.]

A U.S. destroyer has a typical cruising speed of 12 to 14 knots. As shown in Figure 2, this requires only the two ATGs. The system was designed to operate the two ATGs at their most efficient point at the most common cruising speed. Mechanical drive systems operate at inefficient turbine points at common cruising speeds and only operate efficiently at full power. Further, the two MTGs are free for high power weapon or launch systems.

A final benefit of switching to electric drive systems is the ability to go to a direct drive motor. This eliminates all gearing and reduces shafting (or eliminates shafting if podded), which increases overall reliability and decreases the required amount of maintenance. With the growth of EPDS in the commercial maritime industry, the technology has matured to a point where the U.S. Navy can start to consider it as a viable alternative to current mechanical drives systems.

B.   PROPULSION REQUIREMENTS

Both the U.S. Navy and the commercial maritime industry look at the same factors when comparing drive systems. These factors are stealth, space, cost, and reliability and maintenance. The commercial industry was able to use electric drive systems that

outperform their mechanical counterparts in all four areas by using podded propulsion [4]. A podded propulsion system mounts the motor in a compact package known as the pod, which is attached outside the hull, and eliminates the need for expensive mechanical drive components. Figure 3 shows an example of a commercially available pod.

Figure 3. ALSTOM 20MW Azimuth Pod (Mermaid^{TM}) [From Ref. 4.]

The U.S. Navy has chosen not to pursue podded propulsion on the DD(X), but it is still being evaluated as a possibility for future naval vessels [5].

1. Stealth

Naval ships need to be stealthy in the water, especially in battle. Unlike the commercial maritime industry, the U.S. Navy is constrained by the overall platform signature performance of their drive systems. This includes both the acoustic and electromagnetic signatures of the entire shipboard power generation and conversion systems. These vital requirements in the ship's signature are becoming more stringent. This is illustrated by the recent reduction of five for a ship's global electromagnetic limit [1].

Stealth to the commercial industry deals with audible drive system noise and overall passenger comfort. By mounting the complete drive systems outside the hull, the commercial maritime industry was able to greatly reduce overall system noise and increase passenger comfort [4]. Unfortunately, the commercial industry is not concerned with underwater acoustic and transmitted electromagnetic signatures. Therefore the podded system and the majority of current commercial propulsion system designs lack military-grade filtering, making them unsuitable for military use.

2. Space

The podded propulsion system has solved the commercial industry's need to save space for passengers and cargo because of its compact outer-hull design [4]. However, the U.S. Navy has chosen not to pursue podded propulsion systems in the current DD(X)

4

design [5]. Initially there were two proposed DD(X) designs, one with podded propulsion and one with an internal power system [5]. The unpodded propulsion system design was chosen because it could easily be converted back to a mechanical system and due to concern of the overall noise of commercial podded systems [5].

Since the U.S. Navy is currently not pursuing podded propulsion, an alternative needs to be developed that maximizes the power density and specific power of the system to reduce overall size. In addition, the stealth requirement inadvertently makes the drive converter larger, due to a need for a high fidelity current waveform. The need for additional passive or active filtering components can become voluminous.

3. Cost

Probably the most crucial area is cost. Since the entire commercial maritime industry is moving towards all-electric propulsion, the cost for these systems has become very affordable. In addition, a commercial podded propulsion system consumes 30% less fuel then a non-podded equivalent [4]. This is the result of a more hydrodynamic hull design optimized by the use of pods [4].

Mechanical drive systems may become prohibitively expensive without any commercial industry backing. With the entire commercial industry moving towards electric propulsion, it is beneficial that the military follow suit.

The small quantity of military specialty drives may not be a factor for the future maritime market. Therefore, for the military to keep expenses down, the U.S. Navy must learn to incorporate commercial items with little or no design modifications. The focus of this thesis is incorporating a commercially available bulk power converter with a smaller, dedicated conditioning converter to create a stealthy system that saves space and cost.

4. Reliability and Maintenance.

The commercial industry has been able to create very reliable and low maintenance systems using podded propulsion. By using direct-drive, gearing and shafting are eliminated from the drive systems, reducing maintenance to only the electric components and the motor itself. These components tend to be very reliable and require little maintenance.

Even without using podded propulsion, the U.S. Navy can still take advantage of the reliability of electric systems and the elimination of gearing, by use of a direct-drive system. However, U.S. Naval systems also have the additional requirement of being battle hardened. Propulsion systems in a naval vessel are going to be subjected to stresses that would not be seen in a commercial ship. In addition to normal operation of a naval ship, naval systems have to handle the extreme conditions that a ship undergoes during battle, including long operational commitments and extreme degrees of shock and vibration. Since this area has more to do with the physical construction and physical isolation of the system, it is not covered in this thesis.

C. PROPULSION SYSTEMS

A propulsion system consists of four parts:

- AC-source: typically a three-phase turbine generator
- Rectification: diode or active front end
- DC link: may be as simple as an LC-filter
- Inversion: various topologies described below.

Figure 4 shows a block diagram of a complete EPDS.
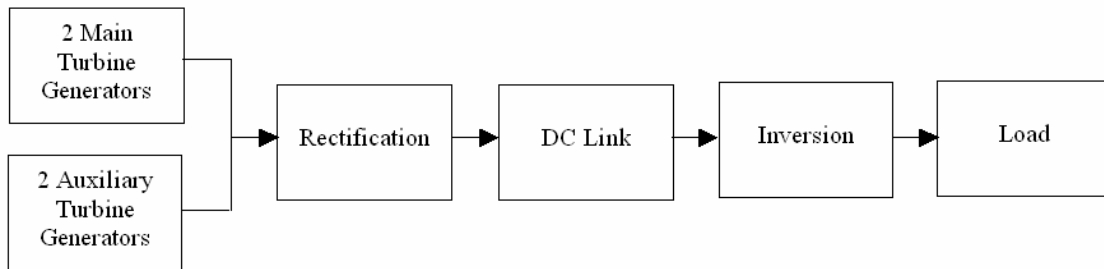
Figure 4. Propulsion System Block Diagram

This thesis concentrates on the inversion portion of the drive, and utilizes a voltage source inverter. However, it is important to keep in mind the other drive components, since cost can be lowered through modular design. A modular design allows for the use of the same structures or building blocks in different parts of the system. For instance, it is common to use the exact same power electronic modules for the "Rectification" and the "Inversion". This philosophy can reduce inventory and maintenance training as well as overall cost.

There are various inverter topologies available that are well suited for modular designs. These include the H-bridge, two-level, Neutral Point Clamped (NPC), multi-level, and Cascaded Multi-Level Converter (CMLC). These topologies are discussed in detail in Chapter II. The focus of this thesis is using a CMLC that consists of a Commercial-Off-The-Shelf (COTS) bulk inverter and a navy specific conditioning inverter. In this form, the CMLC can be controlled in an uncoupled manner, e.g., the bulk inverter operates independently of the conditioning inverter. The bulk inverter utilizes a fundamental-frequency switching control algorithm. The conditioning inverter can utilize any number of control algorithms. Two possible conditioning inverter control algorithms are discussed in detail in this thesis.

D.   THESIS GOAL

The goal of this thesis is to develop and test an uncoupled controlled 3x3 CMLC. This involved developing a control algorithm for the conditioning inverter and an algorithm to extract the reference sine wave information from the bulk inverter. Distortion and transition spikes are used to compare algorithms. Further, dynamic testing was done to determine the tracking accuracy of the output to the reference sine wave.

E.   THESIS OVERVIEW

The next chapter gives a review of common inverter topologies, and introduces the 3x3 CMLC previously built at Naval Postgraduate School (NPS). Chapter III introduces uncoupled control for a CMLC and discusses a simple technique for developing the reference sine wave of the bulk inverter. Chapter IV covers two separate algorithms developed to control the conditioning inverter, one utilizing a modified SVM algorithm and the other utilizing a unique PWM technique that eliminates the need for reference triplen harmonics. Chapter V implements these algorithms in Simulink, and then downloads them into the DS1103 PPC board to do hardware tests. Chapter VI presents the results of the testing, and Chapter VII reports the conclusions.

THIS PAGE INTENTIONALLY LEFT BLANK

II. INVERTERS

A. OVERVIEW

This chapter covers the various inverter topologies available. Control strategies are mentioned, but are covered in more detail in Chapter IV. Finally, the chapter details the previous work done with the 3x3 CMLC currently residing at NPS.

B. INVERTER TOPOLOGIES

There are several types of commercially available voltage source inverters. Basic single-phase topologies include the half-bridge and H-Bridge. Single-phase topologies combine to form multiphase inverters for high power. Multi-phase topologies include the two-level, NPC, multi-level and CMLC. An important direct ac-ac topology known as the cycloconverter is worth mentioning because of its successful application in the Coast Guard Icebreaker Healy [16]. Because of their robustness, they are pegged for a future NPS thesis topic in conjunction with a non-standard high frequency generator. However, cycloconverters are not inverters and not the topic of this thesis.

The half-bridge inverter is generally not used for high voltage applications since its structure underutilizes the source dc bus. However, the H-bridge, which consists of two half-bridges, is a very important topology. The H-bridge inverter is a three-level inverter often used for single-phase systems. It consists of four switches that connect a load to a dc bus. Through switch operation, three distinct voltage levels can be produced across the load, $+V_{dc}$, 0 V, and $-V_{dc}$. Figure 5 shows a block diagram of the H-bridge inverter.
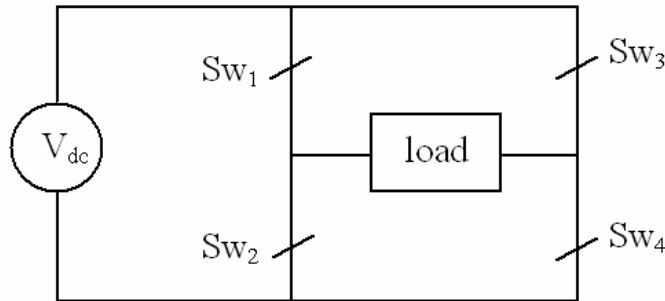
Figure 5.   Single-Phase H-bridge Voltage Source Inverter

9

This topology can be extended to multi-phase loads with isolated individual windings. Many three-phase loads do not have completely accessible windings and require other poly-phase topologies for operation.

The two-level inverter is used for three or higher phase systems. As the name implies, the two-level inverter is capable of producing two distinct voltage levels across each phase leg, V_{dc}, and 0 V. When used in a three-phase systems, this creates three distinct line-to-line voltages, $+V_{dc}$, 0 V, and $-V_{dc}$. Figure 6 shows a three-phase two-level voltage source inverter.
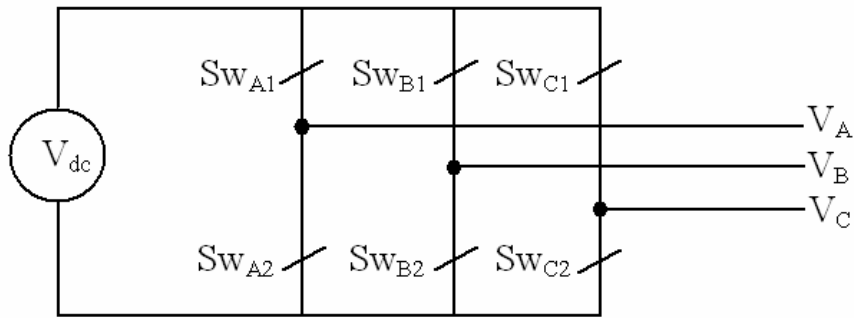
Figure 6.   Two-Level Three-Phase Voltage Source Inverter

The NPC inverter, or three-level inverter, produces three distinct voltage levels per phase. A three-phase NPC is depicted in Figure 7 where each phase can produce $+V_{dc}$, $V_{dc}/2$, and 0 V. The voltage $V_{dc}/2$ is often referred to as E, and the voltage levels for each phase are generally shifted to produce E, 0 V, and $-E$. For a three-phase system, this creates five line-to-line voltage levels: E, $E/2$, 0, $-E/2$, $-E$. The three-level, three-phase voltage source inverter was used as the building block for the CMLC developed in this thesis.

10
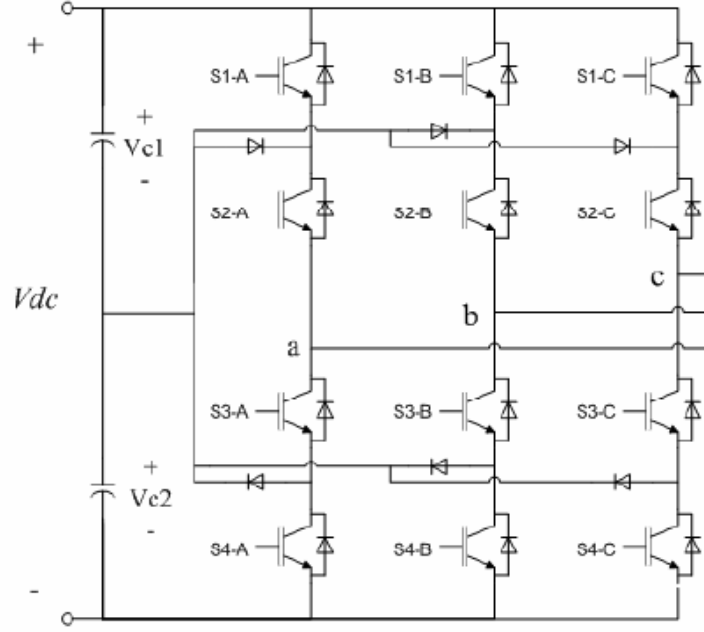
Figure 7.   Three-Level Three-Phase NPC Voltage Source Inverter [From Ref. 7.]

The multi-level inverter topology is an extension of the three-level. By adding more switches, diodes, and capacitors, the DC bus voltage can be divided into more levels. As level count increases, so does the fidelity of the output waveform regardless of controller algorithm. This is analogous to the number of bits in a D/A converter. A higher bit converter is capable of producing a better analog output. As the levels increase, so does the complexity of the hardware and switch mapping control. For an n-level multi-level inverter, there are n distinct voltage levels produced per phase, and ($2n$–1) line-to-line voltage levels. The DD(X) design uses a five-level inverter for its propulsion system [3].

The CMLC is a further extension to the multi-level inverter topology. A CMLC consists of two multi-level inverters cascaded through the load [6] as shown in Figure 8.
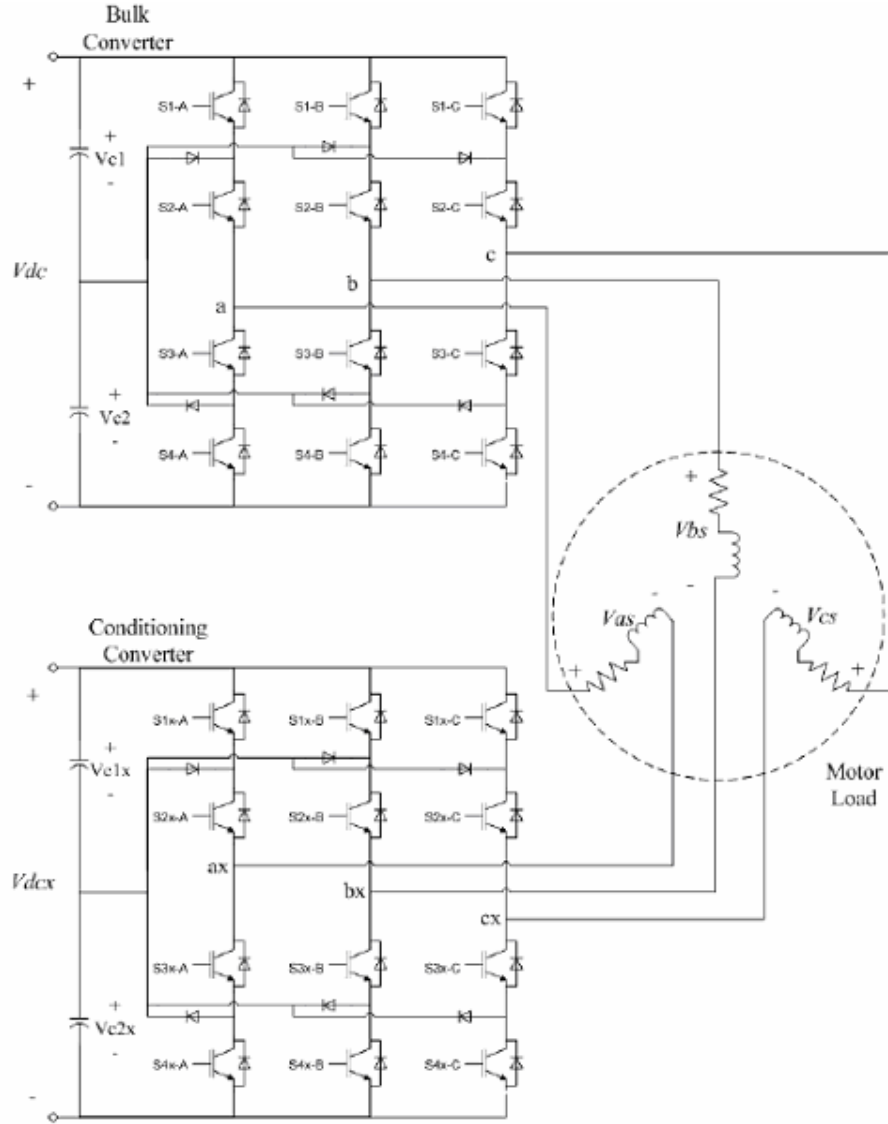
Figure 8.   3x3 Cascaded Multi-Level Converter [From Ref. 7.]

The upper inverter acts as a bulk inverter and supplies the majority of the power to the load, while the lower inverter acts as a conditioning inverter, vastly improving the power quality to the load [2]. CMLCs are classified by multiplying the number of levels of the upper inverter and the number of levels of the lower inverter. For example, a CMLC with an NPC upper inverter and an NPC lower inverter would be called a 3x3 CMLC.

A CMLC can be treated as a single multi-level inverter of equivalent number of levels. This substantially lowers the switch count when compared with a multi-level in-

verter of equal equivalent level. However, the actual number of voltage levels produced by a CMLC varies, based on the ratio of the voltage across the upper inverter (V_{dc}) to the voltage across the lower inverter (V_{dcx}). A useful technique for viewing the different voltage levels produced by a CMLC is to look at the output in the *q-d* reference frame [2, 8] for varying ratios of V_{dc} to V_{dcx}. The *q-d* refers to quadrature-direct and is a transform for simplifying conventional three phase systems. The *q-d* transform takes the three-phase *abc* components and transforms them into an orthogonal two dimensional reference frame. In the case of unbalanced loads, a zero sequence must also be considered; however this thesis focuses solely on balanced loads. The *q-d* reference frame is discussed in more depth in Chapter III.

The first step is to convert the output voltages of the CMLC into line-to-neutral voltages using [2]

$$\begin{bmatrix} v_{as} \\ v_{bs} \\ v_{cs} \end{bmatrix} = \frac{1}{3} \begin{bmatrix} 2 & -1 & -1 \\ -1 & 2 & -1 \\ -1 & -1 & 2 \end{bmatrix} \begin{bmatrix} v_a - v_{ax} \\ v_b - v_{bx} \\ v_c - v_{cx} \end{bmatrix}. \tag{2.1}$$

The next step is to convert the line-to-neutral voltages into the *q-d* stationary reference frame using [2]

$$v_{qs} = \frac{2}{3}\left(v_{as} - \frac{1}{2} v_{bs} - \frac{1}{2} v_{cs} \right) \tag{2.2}$$

and

$$v_{ds} = \frac{1}{\sqrt{3}}\left(v_{cs} - v_{bs} \right). \tag{2.3}$$

By stepping through all possible switching states for the CMLC, a pattern is uncovered, which represents the switching states for the converter in the *q-d* reference frame. Figure 9 shows the available switching states for four different input voltage ratios in the *q-d* reference frame.

Vector plot for $V_{dcx} = V_{dc}$

Vector plot for $V_{dcx} = V_{dc}/2$

Vector plot for $V_{dcx} = V_{dc}/3$

Vector plot for $V_{dcx} = V_{dc}/4$
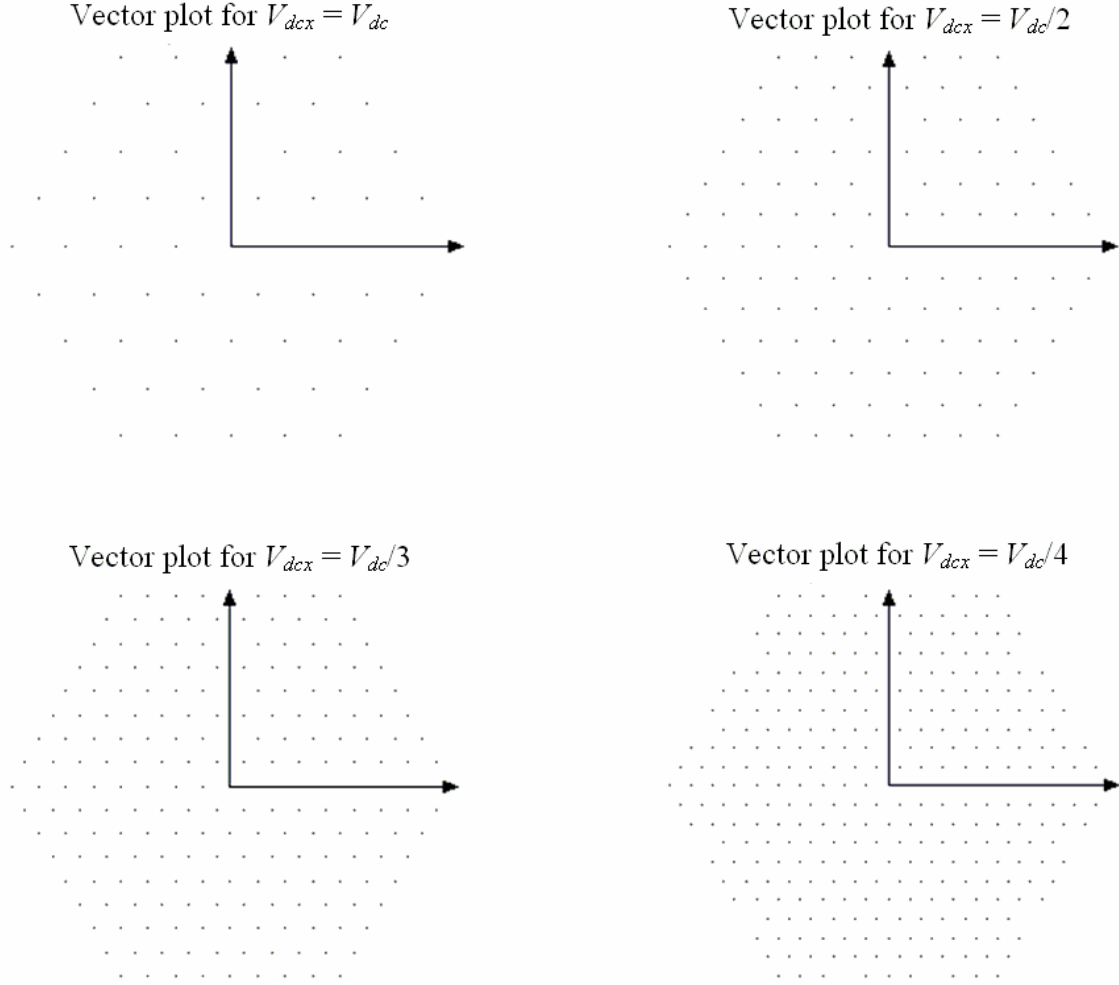
Figure 9.   Vector Plots for Different Voltage Ratios [After Ref. 2.]

The goal is to find the ratio that creates maximal distention. In other words, the ratio that creates the greatest number of equally spaced switching states. As shown above, $V_{dc}/3$ creates the pattern of maximal distention [2]. The point of maximal distention creates an equivalent switching pattern to a multi-level inverter with a level equal to

$$m \; x \; n = 3 \; x \; 3 = 9 \qquad (2.4)$$

where m is the level of the upper bulk inverter and n is the level of the lower conditioning inverter. A CMLC consisting of two NPC inverters was used throughout this thesis.

C.   CONTROL ALGORITHMS FOR INVERTERS

There are several control techniques for multi-level inverters, including: funda-mental-frequency switching control, space vector modulation (SVM), sine-triangle pulse width modulation (SPWM), sub-harmonic PWM methods [9], and switching frequency

14

optimal PWM [9]. Fundamental-frequency switching control, SVM, and SPWM are discussed in detail in this thesis along with a new hybrid algorithm. Information about the sub-harmonic PWM technique can be found in Reference 10, and information about switching frequency optimal PWM can be found in Reference 11.

These control strategies can also be implemented with a CMLC when considered as a single multi-level inverter with equivalent number of levels. However, the primary benefit of the CMLC is the ability to control each inverter separately. Controlling the CMLC as a single equivalent multi-level inverter is referred to as joint control, and controlling the CMLC as two separate inverters is referred to as uncoupled control.

Uncoupled control allows the use of a Commercial-Off-The-Shelf (COTS) bulk inverter utilizing a fundamental-frequency switching control algorithm [6]. Due to the high power density and high specific power of inverters utilizing fundamental-frequency switching control algorithms, the overall footprint of the system is reduced. Further, the use of an uncoupled unmodified COTS inverter reduces overall cost when compared with an equivalent high-power, high-fidelity, Navy-specific solution.

The conditioning inverter is a dedicated inverter specifically built for the U.S. Navy using an advanced control algorithm; however, due to the fact that it operates at 1/3 the bus voltage, it is significantly smaller and less expensive to build, and dissipates less power at high frequency switching than its bulk counterpart. This thesis demonstrates that the pair of inverters is capable of dramatically reducing the Total Harmonic Distortion (THD) of the output waveform (compared to a single COTS unit), which enables stealthy ship propulsion. A final benefit of uncoupled control is system redundancy. As stated earlier, the ship's propulsion power is related to the cube of the ship's speed. If the bulk converter were to be damaged, the conditioning converter could be used to propel the ship, albeit at a reduced speed.

D. NPS-BUILT 3X3 NEUTRAL-POINT CLAMPED CASCADED MULTI-LEVEL CONVERTER

1. Hardware

The inverter used for this thesis was a 3x3 CMLC first constructed for a previous NPS project [7]. The power electronic hardware for a single inverter is shown in Figure 7. As can be seen in the figure, each inverter consists of twelve switching modules (S1A, S1B, S1C, S2A,…,S4C), two capacitors (C1, C2), six diodes (D1-D6), two DC bus bars

($+V_{dc}$, 0 V), and the neutral point bus bar (N) [7]. The DC bus bars provide the power to the inverter and the diodes clamp the neutral point of the inverter. The switches are operated to modulate the output voltage to provide AC output power to the load, and to maintain the neutral point voltage at $V_{dc}/2$.
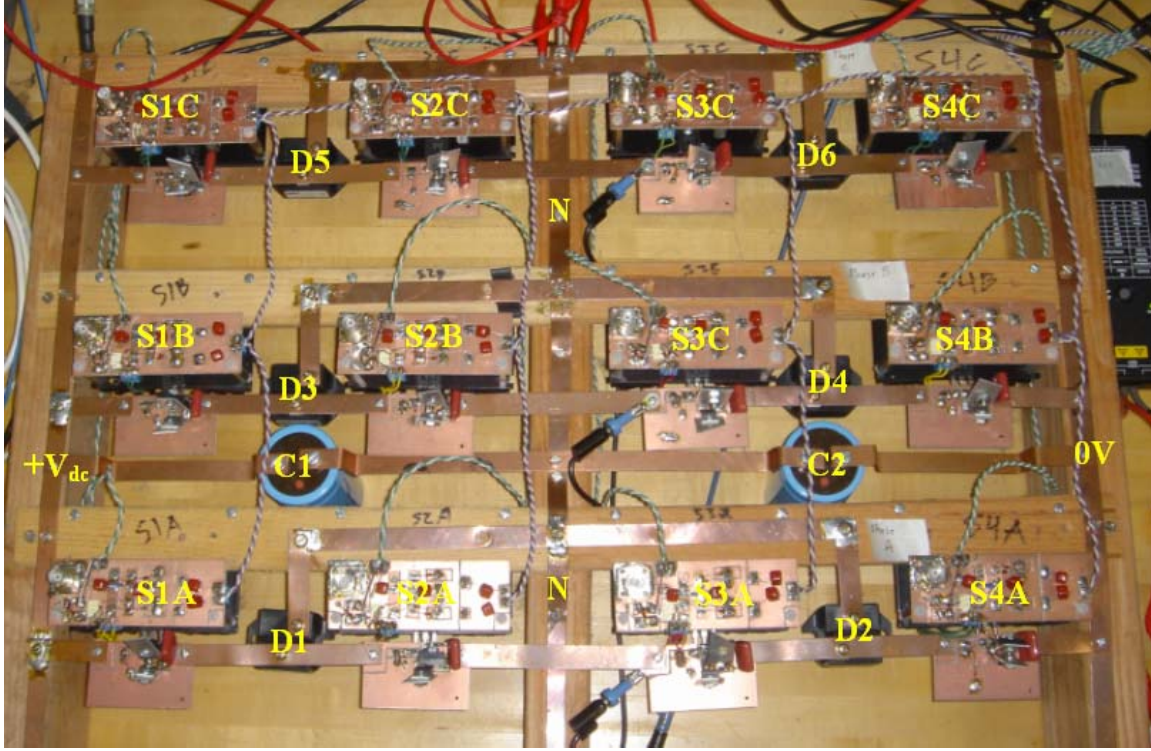
Figure 10. Layout of Single Converter [From Ref. 7.]

The switch modules consist of the snubber card, the gate driver card, and the IGBT switch. The gate driver card was necessary to isolate the IGBT switches from the digital driver logic generated by the dSpace DSP controller card. As specified in Reference 7, the gate driver cards incorporated a switch delay time to assure proper state operation; only one state must exist at a time with no states overlapping.

2. DSP Controller

The DS1103 module produced by dSpace was used as the controller for this CMLC. The module provides easy implementation of Hardware-In-the-Loop (HIL) simulation and Rapid Control Prototyping (RCP) [12]. Prototyping a design is a quick and easy way to develop robust algorithms. However, prototyping requires all of the hardware components to be simulated, which is not always practical [12]. HIL allows for

actual hardware to be connected to the simulation through the DSP interface. The dSpace interface consists of the DSP card, DSP I/O board, and the DSP software interface.

The DS1103 PPC controller board is a single-board system that inserts into a standard Peripheral Component Interconnect (PCI) card slot. The board utilizes a slave Texas Instruments TMS320F240 DSP running at a 20-MHz clock rate. The board contains 4 16-bit ADCs with a 4-µs conversion time, and 4 12-bit ADCs with 0.8-µs conversion time, along with a 32-bit digital I/O bus. Figure 11 shows the controller board.
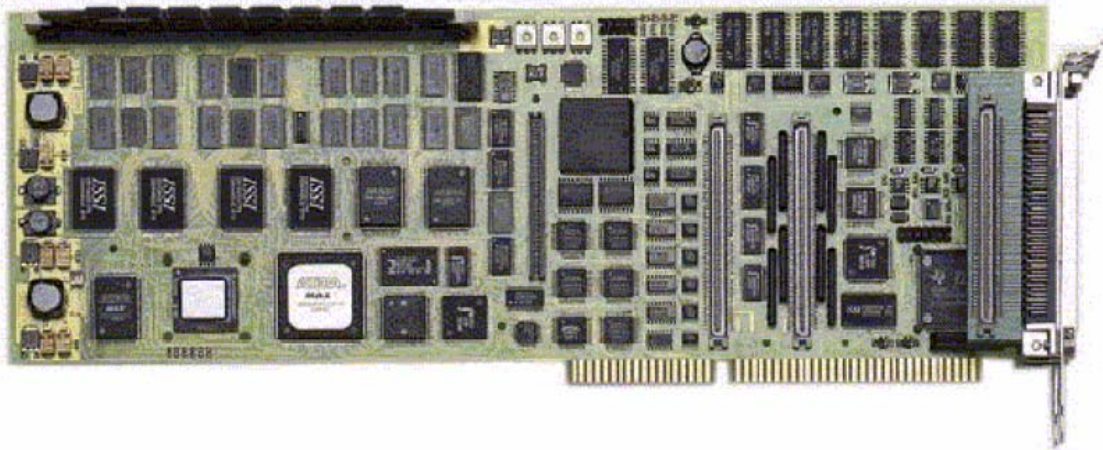
Figure 11.   DS1103 PPC Controller Board [From Ref. 13.]

The dSpace CP1103 I/O Board shown in Figure 12, provides the numerous input and output ports. A 50-pin digital I/O connector was used to connect the CP1103 to the 3x3 CMLC. Four coaxial cables were used to feed the analog inputs into the ADCs.
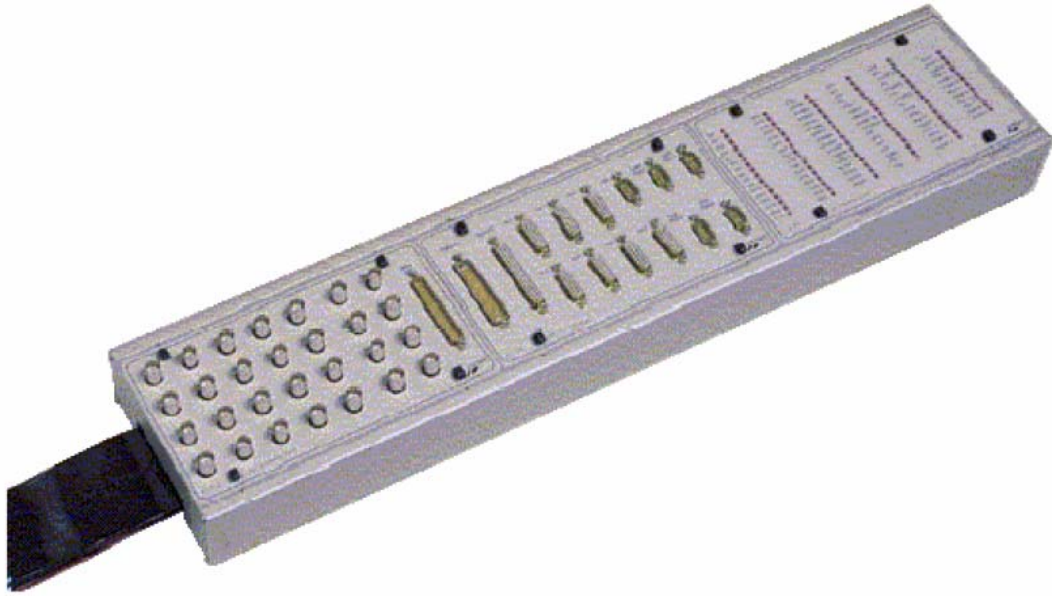
Figure 12.   CP1103 I/O Board [From Ref. 14.]

The DSP software interface consisted of two components. The first component is a Simulink interface with a real-time compiler. This interface allows a software simulation model to be quickly converted to code and downloaded into the DSP card. The second component is the *Control Desk* Interface, which allows the user to compile the Simulink code and load it into the card. The Control Desk has the added benefits of allowing the user to view the signals in the card and change parameters in the simulation during operation. More information on the DSP system can be found in References 12, 13, and 14.

3.   Control Algorithm

The control algorithm chosen to run the hardware in Reference 7 was a simple SPWM algorithm utilizing joint control. SPWM was chosen for the first control algorithm due to its overall simplicity and excellent performance. The algorithm was based on generating a reference sine wave for each phase, and comparing that reference waveform with stacked triangle waveforms operating at the desired switching frequency. The number of stacked triangle waveforms corresponds to the number of levels of the inverter minus one. For a 3x3 CMLC, the total number of equivalent levels is nine, which corresponds to eight stacked triangle waveforms as shown in Figure 13.

18
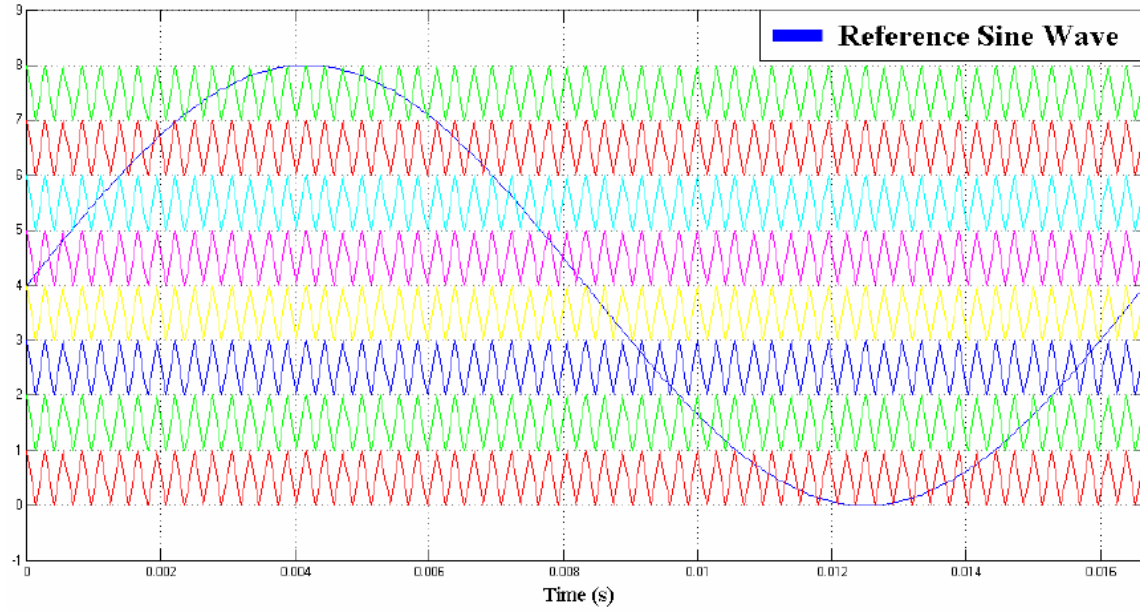
Figure 13.   Sine Triangle Waveform [From Ref. 7.]

Each triangle waveform corresponds to a different switch state. When the reference sine wave is above a given triangle, then the algorithm outputs that given state. For example, switching state "0" exists when the reference sine wave is less than the bottom triangle wave, and state "1" exists when the reference wave is greater than the bottom triangle wave. The switching states are then decoded to determine the position ("on" or "off") of each individual switch in the inverter. Table 1 gives the decoded signals for each switch for a single phase of the 3x3 inverter where S1, S2, S3, and S4 correspond to the upper inverter, and S1x, S2x, S3x, and S4x correspond to the lower inverter.

19

State	S1	S2	S3	S4	S1x	S2x	S3x	S4x
0	0	0	1	1	1	1	0	0
1	0	0	1	1	0	1	1	0
2	0	0	1	1	0	0	1	1
3	0	1	1	0	1	1	0	0
4	0	1	1	0	0	1	1	0
5	0	1	1	0	0	0	1	1
6	1	1	0	0	1	1	0	0
7	1	1	0	0	0	1	1	0
8	1	1	0	0	0	0	1	1

Table 1.   Switch Decoder State Table [From Ref. 7.]

One problem with SPWM is that it does not fully utilize the DC bus voltage. Since three-phase systems eliminate odd triplen harmonics, it is possible to increase the overall voltage output of the system by using these harmonics. Typically a third harmonic is injected into the reference waveform, reducing the peaks of the reference wave, thus allowing for a higher output voltage [6].

Improvements can be made to this system by utilizing an uncoupled control technique [2]. To do this, both a bulk inverter and a conditioning inverter controller must be programmed in the DSP. Furthermore, a technique must be developed to generate a reference sine wave with the same frequency and phase of the bulk inverter. SPWM can be adapted for use in the uncoupled controlled system as the conditioning inverter controller, but was not chosen since it would require the generation of both the reference sine wave and the third harmonic. This would add an additional three sine functions in the DSP, which are time-consuming operations in a DSP.

E.   SUMMARY

This chapter covered the various inverter topologies available. Of the numerous topologies, the CMLC was chosen for further study in this thesis due to its level multiplying and its ability to be controlled as two separate inverters. Chapter III discusses the practical implications of operating the CMLC in an uncoupled manner.

III. UNCOUPLED CONTROL

A. OVERVIEW

This chapter details an uncoupled method of controlling a CMLC. Thus, it presents the ramifications of an autonomous bulk inverter as a part of the cascade. Some limitations of the chosen technique are also discussed. Finally, digital spiking caused by the discrete nature of DSPs is mentioned, but reduction techniques are left to Chapter IV.

B. UNCOUPLED CONTROL

Although a CMLC can be controlled as a single equivalent multi-level inverter, this is undesirable for U.S. Navy purposes. As presented in Chapter II, component count and complexity decrease when a single multi-level is replaced with an equivalent cascaded version. The separability of high power and high fidelity functions allows the use of a COTS bulk converter with a low-power, low-cost, Navy-specific inverter for active filtering. Figure 14 shows the configuration of the CMLC used in this thesis.
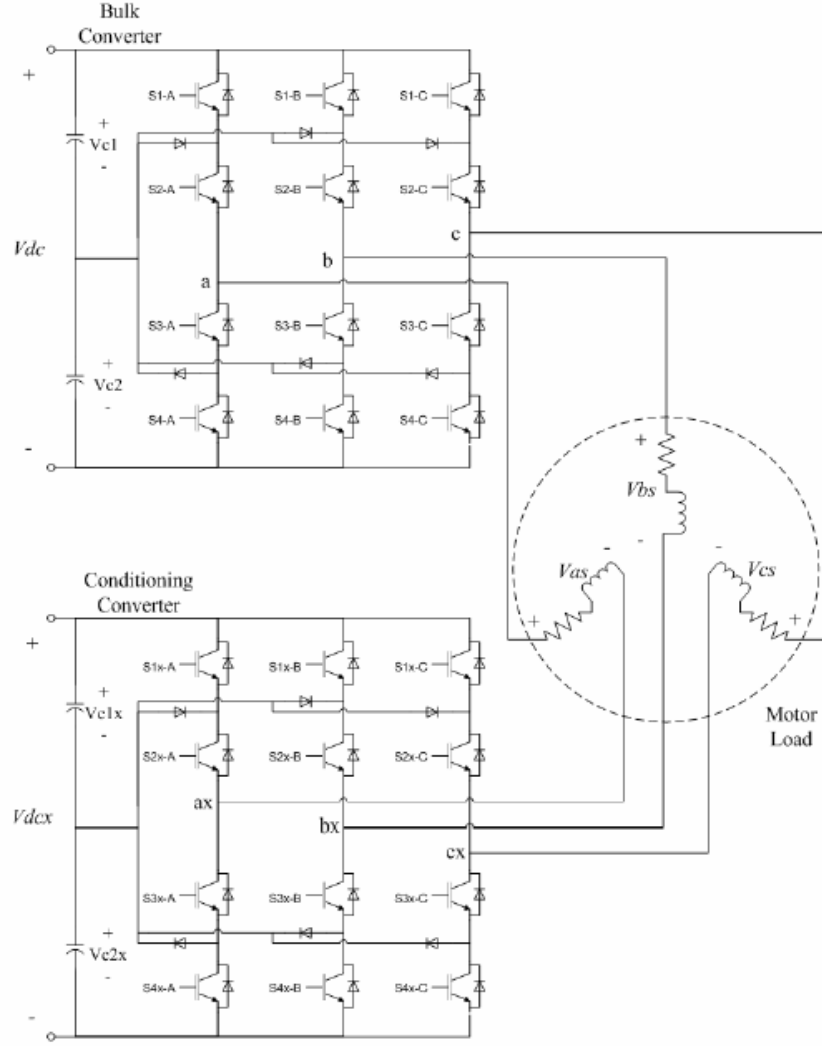
Figure 14.   Cascaded Multi-Level Inverter [From Ref. 7.]

The upper inverter in Figure 14, referred to as the bulk inverter, can be any *n*-level inverter driven by a fundamental-frequency switching controller. The controller algorithm is extremely important in that it provides the maximum power density of any inverter configuration due to the low number of switching events during a cycle. The lower inverter in Figure 14, referred to as the conditioning inverter, can also be any *n*-level inverter, but is controlled using one of the more advanced control algorithms discussed in Chapter IV. This allows it to filter out the harmonic content of the bulk inverter. The conditioning inverter switches at a much higher frequency, but at one-third the voltage since it operates at the maximal distention point. Further, a high bandwidth control loop allows the conditioning inverter to act as an active filter, reducing the output

waveform to a nearly pure sinusoid at the desired frequency. The active filtering with the lower bus voltage requires a power rating of approximately one-tenth that of the bulk converter.

In order to actively filter the harmonic content of the bulk inverter waveform, an error signal representing only harmonic information must be uncovered. This is done by first generating a reference sine wave locked to the frequency of the bulk converter as shown in Figure 15.
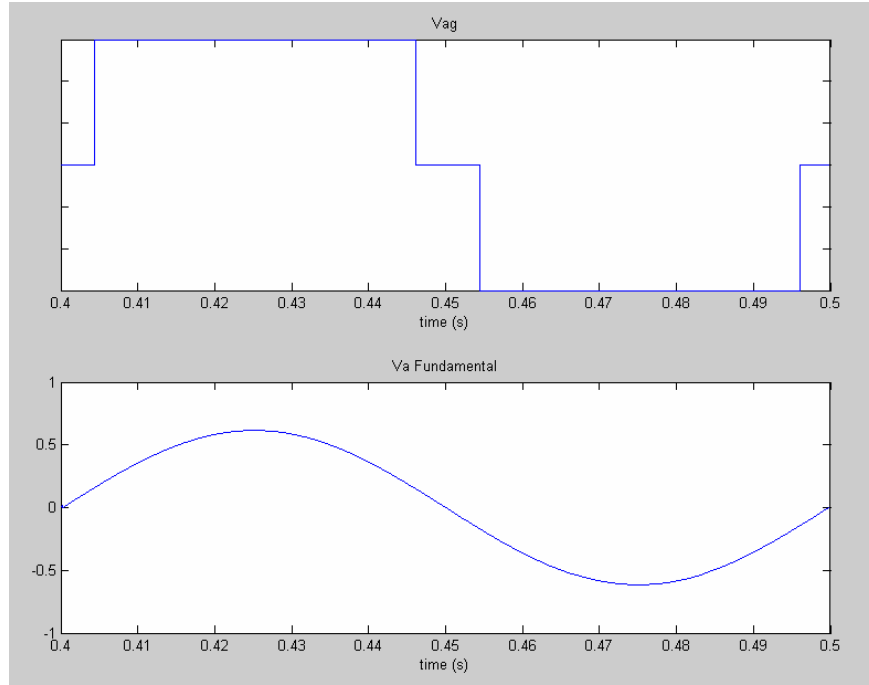
Figure 15.   Bulk Converter Output With Reference Sine Wave

By properly adjusting the magnitude and phase of the reference fundamental, an error signal containing only harmonic information can be extracted by simple subtraction [2].

$$
\begin{aligned}
v_{ag,h} &= v_{ag} - v_{ag,f} \\
v_{bg,h} &= v_{bg} - v_{bg,f} \\
v_{cg,h} &= v_{cg} - v_{cg,f}.
\end{aligned}
\tag{3.1}
$$

The harmonic-only signals (Figure 16) are then used as the command voltages for the conditioning inverter.
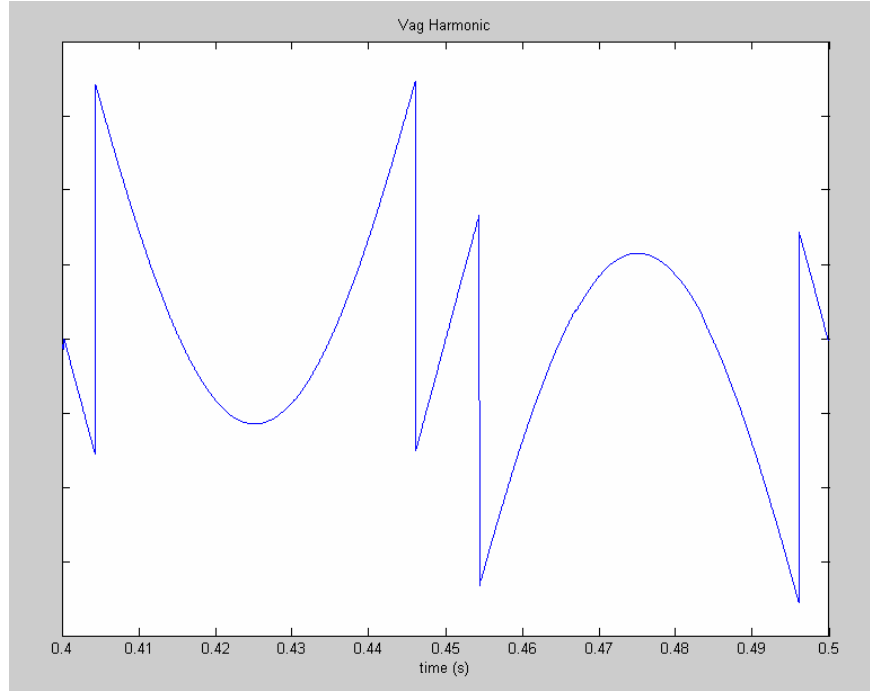
Figure 16.   Harmonic Waveform for Phase A [After Ref. 2.]

C.   BULK INVERTER OPERATION

Figure 19 displays output waveforms for a three-level NPC bulk inverter where v_a and v_b are line-to-ground voltages, and v_{ab} is a line-to-line voltage. The resultant line-to-line voltage appears as a distinct stair-step waveform. The magnitude of the fundamental portion of the phase voltages is controlled via the angle α. All of the CMLC control is derived from the output waveform of the bulk inverter whose only control parameter is the angle α. Thus, the operation of the bulk inverter has the greatest effect on the overall operation of the entire system.

24
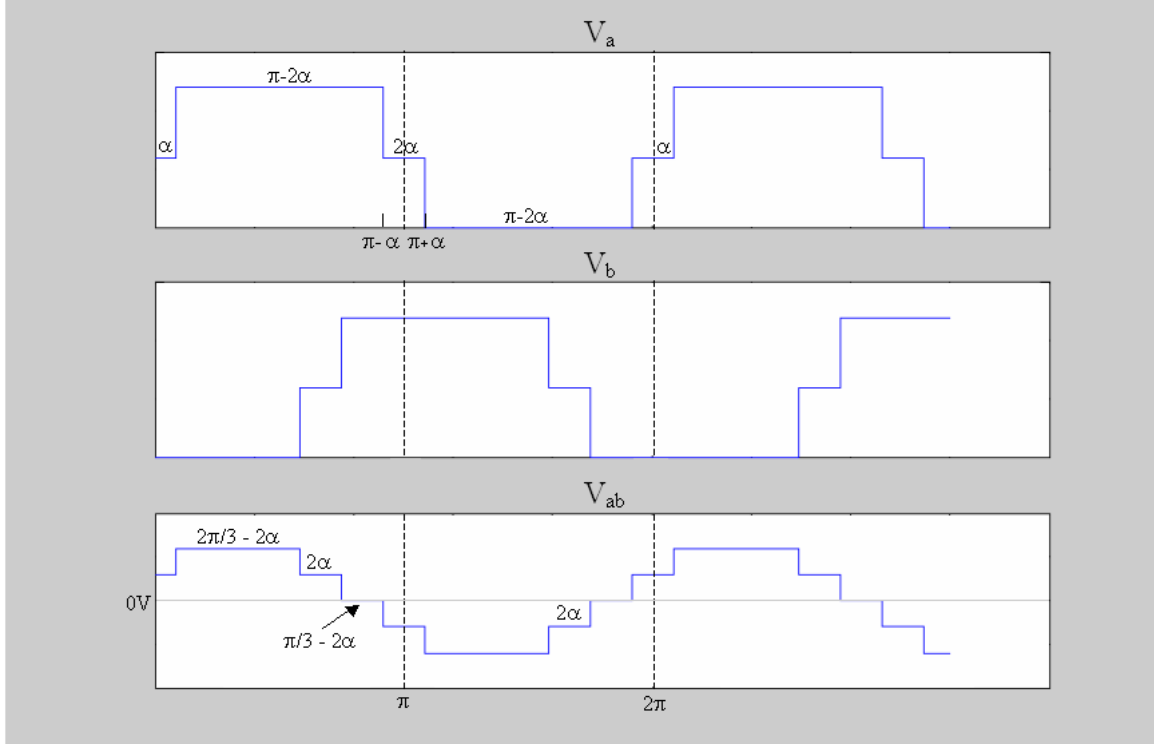
Figure 17.   Bulk Inverter Output Waveform [After Ref. 2.]

The relationship between the peak value of the fundamental v_{fund}, the dc bus voltage V_{dc}, and the control angle α, appears in the following equation [2]

$$v_{fund} = \frac{2V_{dc}}{\pi}\cos(\alpha).\qquad(3.2)$$

The valid control angles are $0° < \alpha < 90°$. As α is adjusted, the commanded magnitude of the output fundamental voltage changes and the CMLC control operators are affected. This is apparent due to a change in the available switching states and a necessary adjustment to the reference sine wave.

The output angle α has an extreme impact on the available output voltage vectors for a CMLC using uncoupled control. By transforming the system into the q-d reference frame as was done in Chapter II, and plotting the available output states of the system for several different angles, the affect of α can be seen. Figures 18, 19, and 20 show the output states for a 3x3 CMLC with $\alpha = 0°$, $\alpha = 15°$, and $\alpha = 45°$, respectively. The blue dots represent the standard switching states available for a jointly controlled 3x3 CMLC. The black circles represent the switching states available for a 3x3 CMLC using uncoupled control with the bulk converter operating with the given control angle α.

25
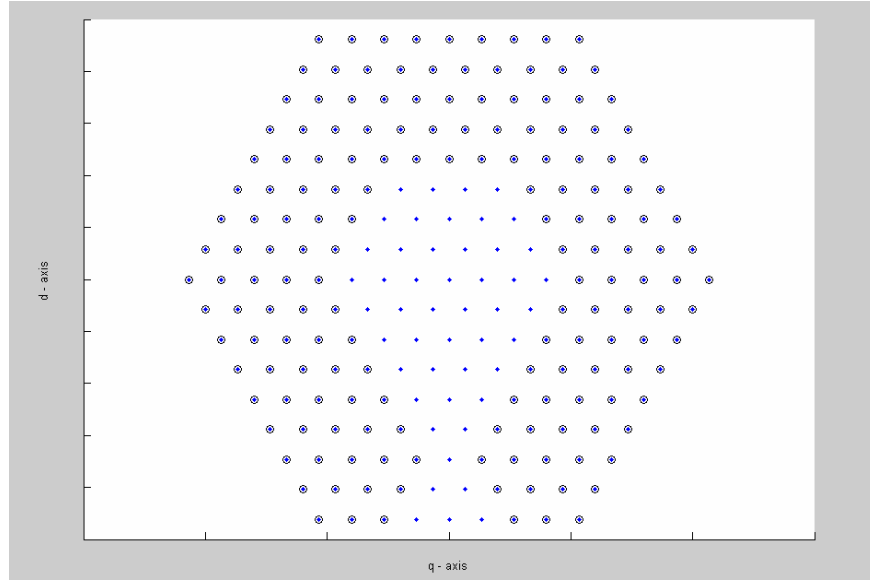
Figure 18.   Available Switching States for $\alpha = 0°$
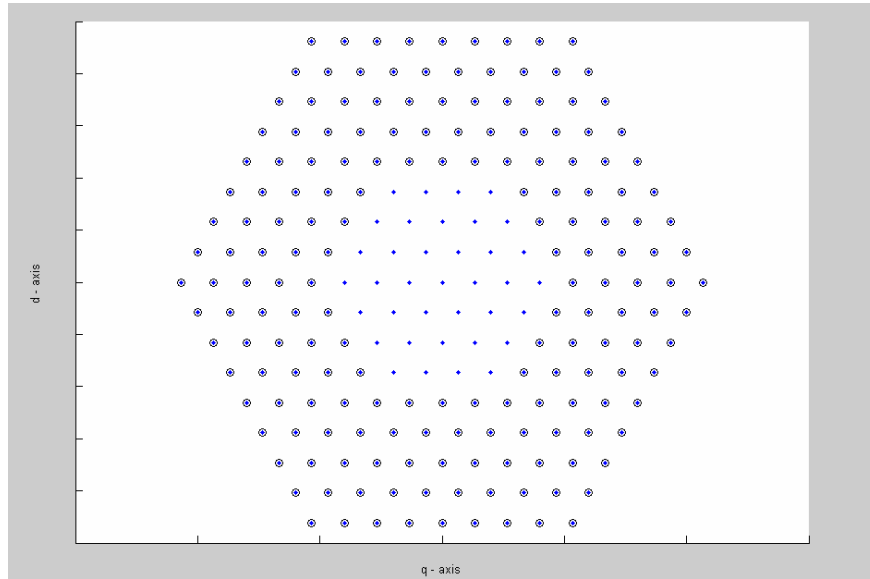
Figure 19.   Available Switching States for $\alpha = 15°$

26
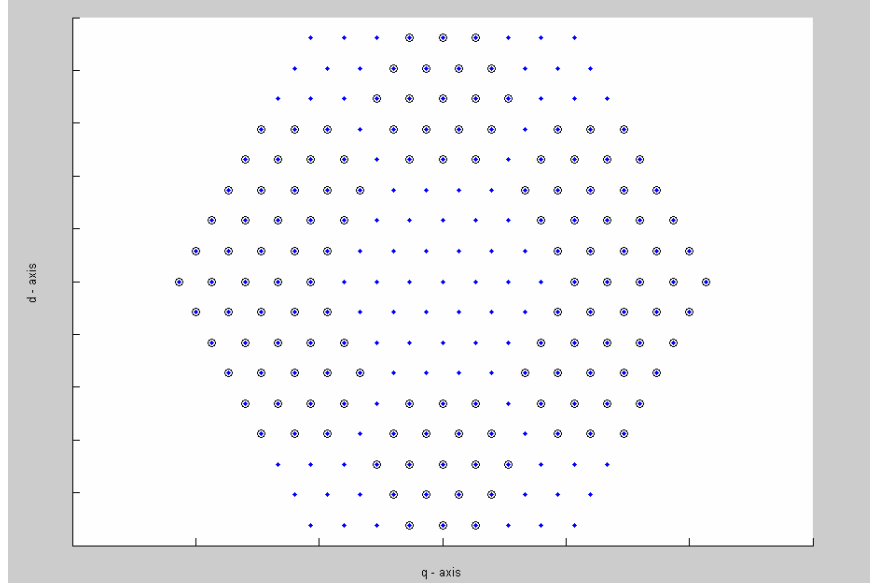
Figure 20.   Available Switching States for $\alpha = 45°$

As seen from these three figures, the available output switching states change drastically as the control angle varies. An α of 15°, which was used in Reference 2, was used throughout this thesis. With this α, the system cannot adequately represent lower voltages due to the lack of switching states. There are two fixes to this. The first is to use the conditioning inverter alone, and the second is to use a controllable DC front end. Operating the conditioning inverter alone reduces the level of the system to three, thus increasing THD. By utilizing a controllable DC front end any voltage can be emulated while employing all the available voltage levels of the inverter, thus producing the highest quality output waveform.

The control angle α also influences the generation of the reference sine wave. There are several ways to generate the reference sine wave. Two methods are evaluated below. One method is independent of α, but involves filtering and complex computations. It continually updates the frequency, but always lags by the filter delay [6]. The other method uses α and an integrator as a timer. It updates the frequency at discrete intervals where the maximum update rate is 12 times per period of the output sine wave.

27
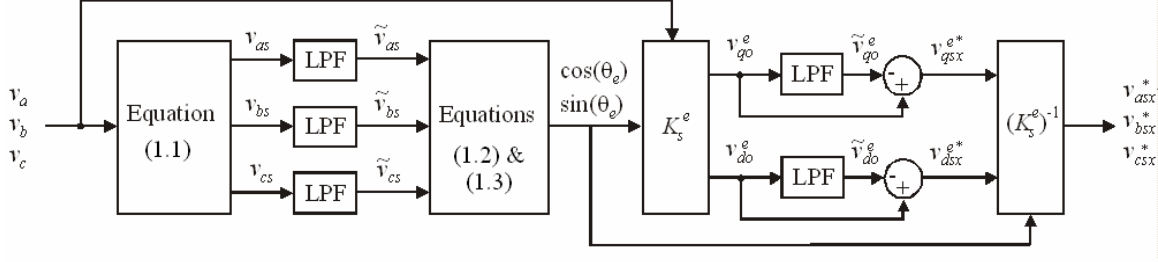
Figure 21.   Block Diagram for *q-d* Reference Sine Wave Generation [After Ref. 6.]

The first method finds the line-to-neutral voltages (v_{as}, v_{bs}, and v_{cs}) utilizing the transformation introduced in Chapter II, Equation (2.1). These voltages are then filtered to create sine waves whose steady-state frequency matches the bulk converter reference sine wave. Once the fundamental components are found, the cosine and sine of the electrical angle can be uncovered using the following equations [6].

$$\cos\left(\theta_e\right) = \sqrt{\frac{3}{2}} \frac{\tilde{v}_{as}}{\sqrt{\tilde{v}_{as}^2 + \tilde{v}_{bs}^2 + \tilde{v}_{cs}^2}} \tag{3.3}$$

and

$$\sin\left(\theta_e\right) = \sqrt{\frac{1}{2}} \frac{\tilde{v}_{cs} - \tilde{v}_{bs}}{\sqrt{\tilde{v}_{as}^2 + \tilde{v}_{bs}^2 + \tilde{v}_{cs}^2}} \tag{3.4}$$

With the cosine and sine of the electrical angle known, the bulk inverter output voltages can be transformed into the synchronous *q-d* reference frame, and then filtered to create the desired output voltages, $\tilde{v}_{qo}^e$ and $\tilde{v}_{do}^e$. The original transformed voltages v_{qo}^e and v_{do}^e are then subtracted from the filtered $\tilde{v}_{qo}^e$ and $\tilde{v}_{do}^e$ voltages. This results in the commanded v_{qsx}^{e*} and v_{dsx}^{e*} voltages, which are then transformed back to the stationary *abc* reference frame. These transformed voltages are then used as the commanded voltages for the conditioning inverter. More detailed information can be found in Reference 6.

The second method does not require any transformations or complex equations, but is dependent on the control angle, α. For this implementation, the frequency is found by using an integrator to measure the time of a bulk inverter output state (refer to Figure 17). With the time *t* found for a single output state, the total period of the bulk inverter waveform can be found. First the proportion *P* of the total period of the output state is found by

28

$$P = \frac{L}{2\pi}, \tag{3.5}$$

where L is the length in radians of output state being timed. The lengths of the different output states are shown in Figure 17, and are dependent on α. From this, the period is found by

$$T = \frac{t}{P}, \tag{3.6}$$

which reduces to

$$T = \frac{2\pi}{L}t. \tag{3.7}$$

Finally, the fundamental frequency is easily extracted,

$$f_{fund} = \frac{1}{T} = \frac{L}{2\pi t}, \tag{3.8}$$

and, the angular frequency is

$$\omega_{fund} = 2\pi f_{fund} = \frac{L}{t}. \tag{3.9}$$

Multiplying the angular frequency with a timer that is reset with the rising edge of each phase of the bulk inverter output and delayed by the control angle α, creates the reference sine wave in phase with the bulk inverter. The actual implementation is discussed in the Chapter IV. This technique was used to generate the reference sine wave throughout this thesis.

D.   DIGITAL SPIKE ELIMINATION

One consequence of uncoupled control is the creation of digital spikes [6]. This anomaly occurs when the bulk inverter switches output states while the conditioning inverter is in the middle of a PWM cycle. Figure 22 shows a simulation of the 3x3 CMLC containing associated spiking.
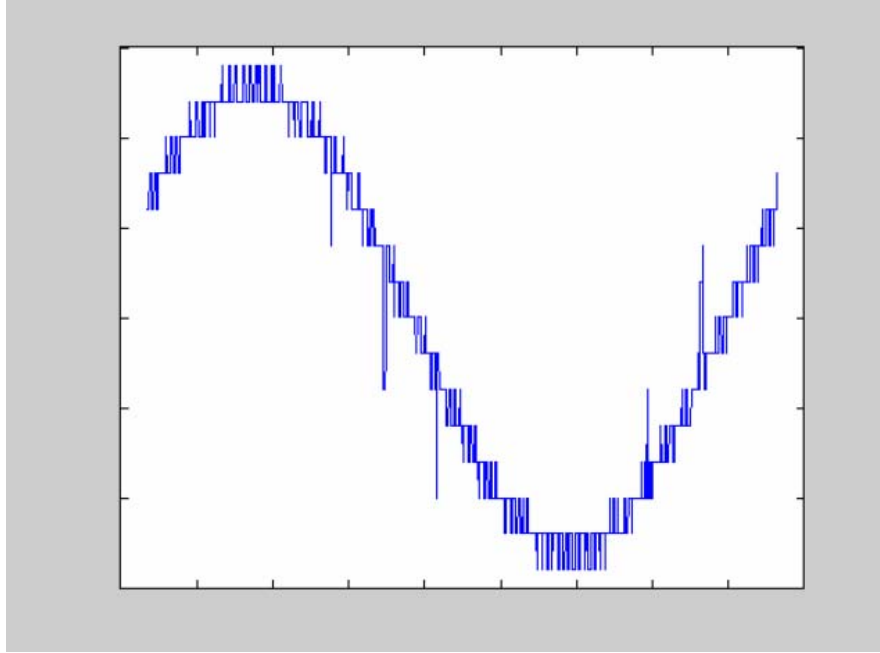
Figure 22.   Simulation Showing Spikes Produced in Output Waveform

This thesis reviews two techniques to reduce overall duration of these spikes. The first technique adds a reset to the SVM algorithm. Ideally this reset would be triggered via a hardware edge detector circuit, signaling a software reset to the PWM cycle. However, for this thesis a software implementation of the edge detector was created for validation purposes. This is discussed further in Chapter IV. A software implementation should decrease the duration of the digital spike to within one or two DSP update cycles, which is typically 10 to 100 times faster than the PWM cycle. It is important to distinguish between a DSP clock cycle and a DSP update cycle. The clock cycle is the actual period of the DSP clock, e.g., 50 ns for our DSP, corresponding to a clock frequency of 20 MHz. The update cycle refers to the time it takes the DSP to complete all calculations and restart. DSP update cycles of 55.6 μs and 33.3 μs are used for this thesis, corresponding to DSP update frequencies of 18 kHz and 30 kHz.

The second technique is inherent to triangle PWM algorithms. Since there are no duty cycle computations and no PWM cycles, the algorithm instantly detects a change in the bulk inverter state and updates accordingly. The hybrid controller algorithm presented in Chapter III takes advantage of this property to reduce the spike widths to within one DSP update cycle.

30

An alternate method to reduce the spikes not used in this thesis is discussed in detail in Reference 6. This technique nearly eliminates the spikes and is independent of the DSP. However, it requires the use of additional hardware and software resulting in a more complex system.

E.   SUMMARY

When operating a CMLC as two separate inverters, the bulk inverter control angle, α, has several effects on the system. This includes the available switching states of the system, the magnitude of the output voltage, and the generation of the reference sine wave. A control angle of 15° was chosen to maximize the output voltage and minimize the harmonic content of the bulk inverter. To generate the reference sine wave from the bulk inverter, a digital timing technique was chosen due to its simplicity. Finally, two techniques were introduced to reduce the digital spiking of the system, and are tested in Chapter V. With the system set up for uncoupled control, Chapter IV examines possible control algorithms for the conditioning inverter.

THIS PAGE INTENTIONNALY LEFT BLANK

IV.   SPACE VECTOR MODULATION

A.   OVERVIEW

This chapter details SVM algorithms. Two algorithms utilizing two different transforms are introduced. The first algorithm is based on the *q-d* reference frame and is shown to be significantly more complex than the second algorithm, which is based on the *g-h* reference frame. Additionally, a hybrid algorithm developed specifically for this thesis is presented. The attributes of the second SVM algorithm and the hybrid algorithm are compared by actual HIL implementation via the CMLC and dSpace controller.

B.   SPACE VECTOR MODULATION

SVM has become a common control technique that can be used for multi-level and cascaded multi-level inverters. All SVM techniques follow the same basic pattern [10, 17, 18]:

- Transform into *q-d* reference frame (or *g-h* frame)
- Detect the three nearest vectors
- Determine the vector duty cycles
- Transform into relevant switching states.

SVM employs a two dimensional transformation to represent the three-phases of high power systems. The two transformations commonly used are the Park's transform, and the *g-h* transform introduced in Reference 17. The Park's equations convert the *abc* time varying phase components into the orthogonal *q-d* reference frame [8]. The *g-h* transform uses a 60° non-orthogonal basis to transform *abc* into the *g-h* reference frame. The *g-h* transform greatly simplifies the detection of the nearest vectors, and reduces duty cycle calculations to simple addition and subtraction when using SVM. Restated, both transforms are generally used to emulate a three-phase power system in a simpler form.

A three-phase voltage supply reduces to a circle in the *q-d* reference frame [2] and an ellipse in the *g-h* reference frame. Figure 23 shows a three-phase sinusoidal reference voltage transformed into the *q-d* reference frame and overlaid onto the space vector plot for a nine-level inverter.
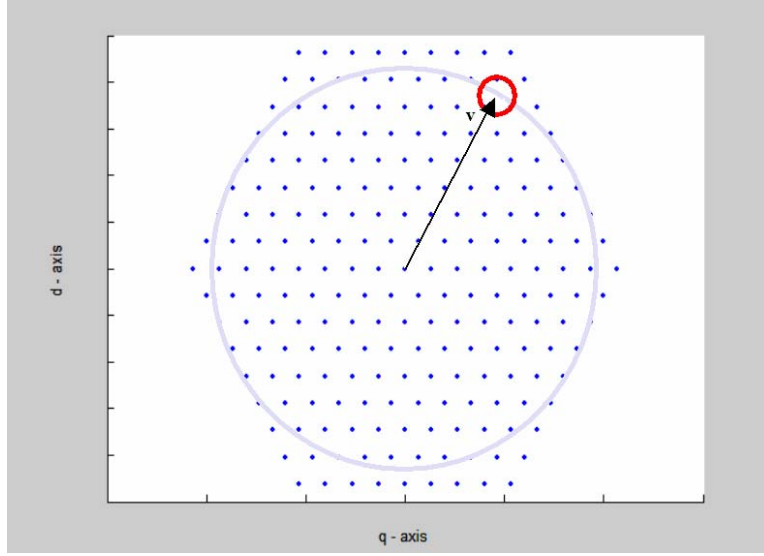
Figure 23.   *q-d* Transform of a Three-Phase Voltage Source

The vector **V** represents the instantaneous voltage at a given time *t*. As *t* increases, the vector continuously rotates counter-clockwise around the circle as shown in Figure 23. SVM algorithms replicate the vector by utilizing the three nearest voltage levels produced by the inverter, and then cycling through those levels with appropriate duty cycles. This can be shown in a volt-second equivalence relationship [10],

$$\mathbf{V}_{ref}T_s = \mathbf{V}_{out1}T_1 + \mathbf{V}_{out2}T_2 + \mathbf{V}_{out3}T_3. \qquad (4.1)$$

Two SVM techniques are introduced below, one based on each reference frame. The *g-h* reference frame SVM algorithm provides a much simpler approach and is used as a basis for the control algorithm of the CMLC conditioning inverter in this thesis. The *g-h* transform also has another property that makes it appealing. It can be used to create a simple hybrid PWM algorithm that is discussed later in this chapter.

C.   SPACE VECTOR MODULATION IN THE *q-d* REFERENCE FRAME

1.   Transform into the *q-d* Reference Frame

The first part of SVM involves transforming the converter voltages into the general *q-d* reference frame by using Equations (2.1), (2.2), and (2.3). For an *n*-level inverter, 2*n*–1 line-to-line voltage levels are produced. For a three-level inverter, there are five voltage levels produced: two positive, two negative, and zero. Plotting all possible inverter output voltages in the *q-d* reference frame gives us the space vector plot shown in Figure 24.

34
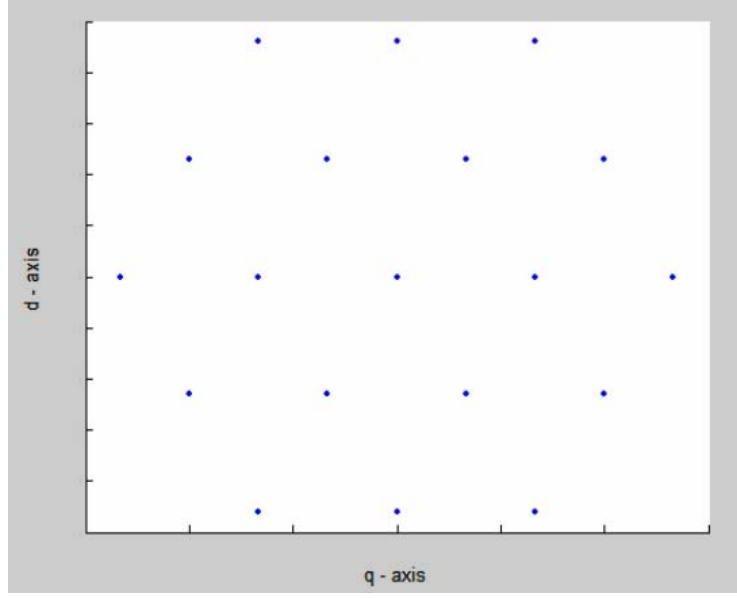
Figure 24.   SVM Plot for a Three-Level Inverter

Space vector plots do not show redundant switching states. For a general n-level three-phase inverter, there are [6]

$$n_{sw} = n^3 \tag{4.2}$$

switching states and [6]

$$n_{vec} = 3n(n-1)+1 \tag{4.3}$$

vectors, as shown in Figure 24. The difference between the number of switching states and the number of vectors leads to redundant switching states. Thus, the number of re-dundant switching states is equal to [6]

$$n_{sw} - n_{vec}. \tag{4.4}$$

These redundant switching states are the result of the common-mode voltage not included in the space vector plot [2]. The redundant states can be used to achieve certain control objectives, such as capacitor voltage balancing, and the elimination of the secondary power supply for the lower inverter of the CMLC [2].

2.   Detection of Three Nearest Vectors

The next step in SVM is the detection of the three nearest vectors. This is simple for a two-level inverter, but becomes more difficult as the level of the inverter increases. There have been several techniques designed to simplify this process, but they are still rather complex. One technique considered for this thesis breaks down the vector into an

35

offset component and a two-level component [10]. Figure 25 shows a three-level space vector plot, with a commanded reference voltage, $\mathbf{V}_{RV}$, which breaks down into an offset reference voltage, $\mathbf{V}_{RV(OFST)}$, and a two-level component, $\mathbf{V}_{RV(twl)}$.
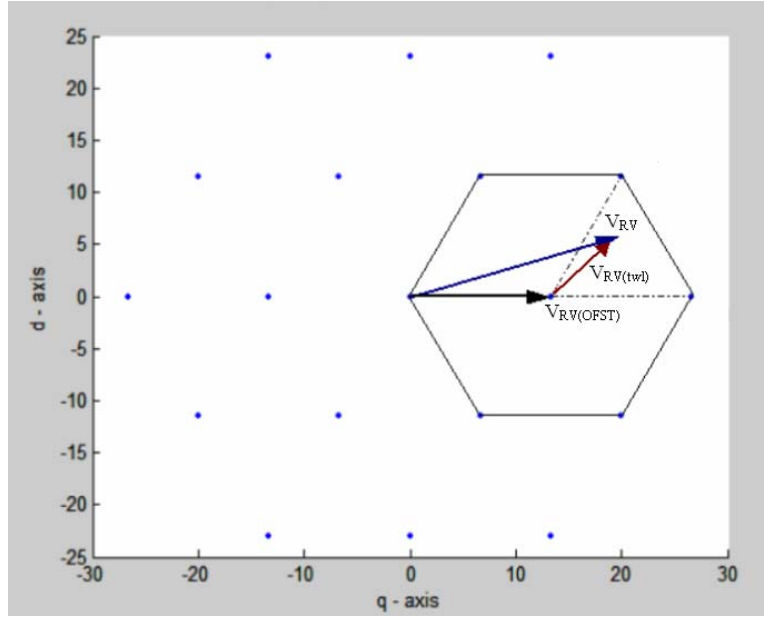
Figure 25.   Reference Vector Breakdown into Two-Level Component and Offset Component

This reduction to an offset reference component ($\mathbf{V}_{RV(OFST)}$) and a two-level component ($\mathbf{V}_{RV(twl)}$) simplifies detection of the three nearest vectors. $\mathbf{V}_{RV(OFST)}$ acts as the zero vector of a two-level system, and is one of the three nearest vectors. One method for determining the other two vectors is by uncovering the angle of the two-level vector with respect to the offset vector. Once the nearest vectors are found for the two-level system, the three nearest vectors for the complete system are $\mathbf{V}_{RV(OFST)}$, $\mathbf{V}_{RV(OFST)}+\mathbf{V}_{RV(twl)1}$, and $\mathbf{V}_{RV(OFST)}+\mathbf{V}_{RV(twl)2}$.

3.   Determination of the Duty Cycle

The next step is to determine the duty cycle for each of the three nearest vectors. First the three-level plot is simplified to a two-level plot by subtracting out the offset vector [10], resulting in Figure 26.

Figure 26.   Break Down of the Three-Level System into Equivalent Two-Level

This simplifies the duty cycle calculations. The dwelling times for each vector are then
calculated using the following equations [10]

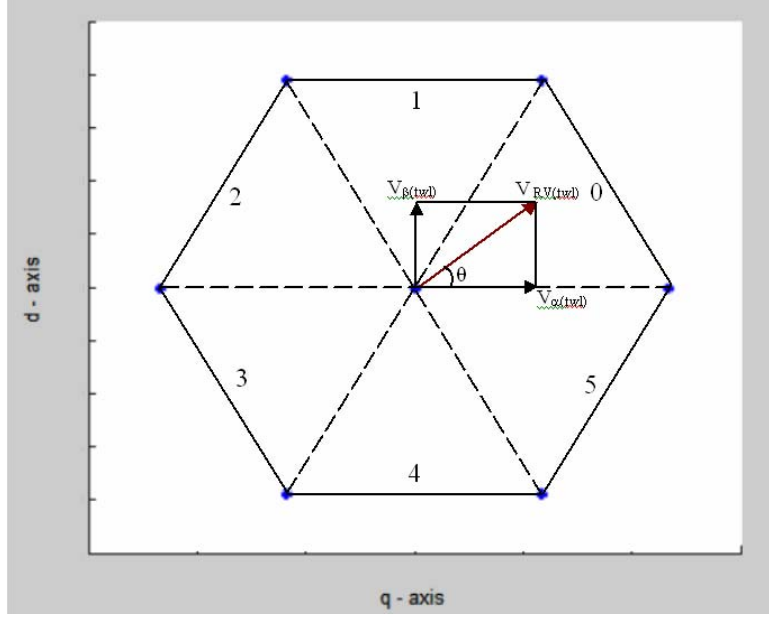$$T_2 = \begin{cases} \dfrac{2}{\sqrt{3}} T_s \left| V_{RV(TWL)} \right| \sin\left[\dfrac{\pi}{3} - (\theta - k_{\text{sec}} \dfrac{\pi}{3}) \right] & k_{\text{sec}} = 0,2,4 \\[4mm] \dfrac{2}{\sqrt{3}} T_s \left| V_{RV(TWL)} \right| \sin(\theta - k_{\text{sec}} \dfrac{\pi}{3}) & k_{\text{sec}} = 1,3,5 \end{cases} \tag{4.5}$$

$$T_3 = \begin{cases} \dfrac{2}{\sqrt{3}} T_s \left| V_{RV(TWL)} \right| \sin(\theta - k_{\text{sec}} \dfrac{\pi}{3}) & k_{\text{sec}} = 0,2,4 \\[4mm] \dfrac{2}{\sqrt{3}} T_s \left| V_{RV(TWL)} \right| \sin\left[\dfrac{\pi}{3} - (\theta - k_{\text{sec}} \dfrac{\pi}{3}) \right] & k_{\text{sec}} = 1,3,5 \end{cases} \tag{4.6}$$

and

$$T_1 = T_s - T_2 - T_3 , \tag{4.7}$$

where k_{sec} = 0,1,2,3,4,5 is the sector number as shown in Figure 26, and T_s is the total
switching period. Despite the simplification in calculating the duty cycle for each vector,
it still requires computationally expensive functions.

4.   Transform into Relevant Switching States

For higher-level inverters, there are multiple switching states that can represent
the same switching vector. A redundant switching state is selected based on one or more
control objectives that may include capacitor balancing and secondary bus supply elimi-

nation [2, 6]. A proposed switching state strategy based on zero-sequence components is discussed in detail in Reference 17.

D. SPACE VECTOR MODULATION *g-h* REFERENCE FRAME

The *q-d* reference frame is the most studied reference frame for developing SVM control algorithms. Unfortunately, algorithms based on the *q-d* reference frame have traditionally been complex and difficult to implement [18]. Another simplification that has been introduced is the *g-h* reference frame [17]. The *g-h* reference frame is based on a 60° non-orthogonal coordinate system as shown below in Figure 27 (where the voltages are normalized to bus voltage V_{dc}).
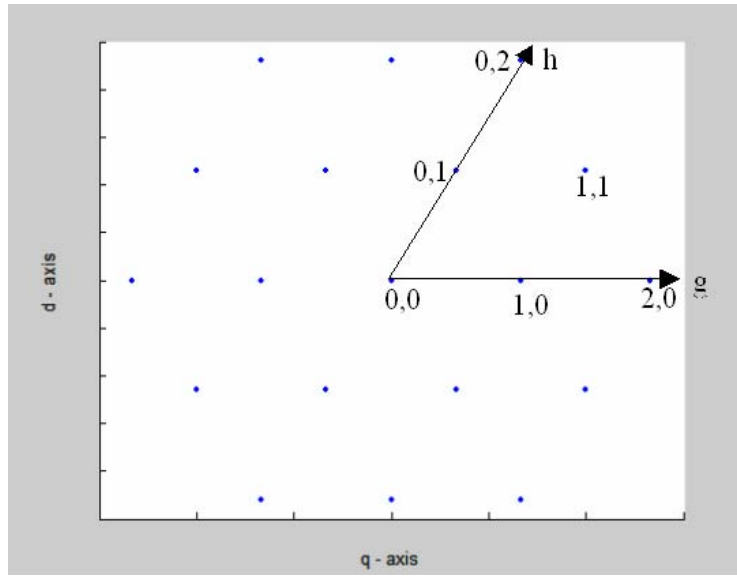
Figure 27.   *g-h* Reference Frame (normalized) Overlaid on *q-d* Reference Frame

Using the *g-h* reference frame still follows the same basic steps as using the *q-d* reference frame, but requires less programming.

1. Transformation to *g-h* Reference Frame

The transform equations for the *g-h* reference frame for a multilevel converter are [17]

$$\mathbf{V}_g = \frac{2v_{ab} - v_{bc} - v_{ca}}{3V_{dc}},\tag{4.8}$$

and

$$\mathbf{V}_h = \frac{-v_{ab} + 2v_{bc} - v_{ca}}{3V_{dc}}.\tag{4.9}$$

Because of the normalization with the bus voltage V_{dc}, the switching state vectors in the *g-h* coordinate system have only integer components [17].

2. Determination of Three Nearest Vectors

By viewing a reference vector in the *g-h* reference frame (as shown in Figure 28),
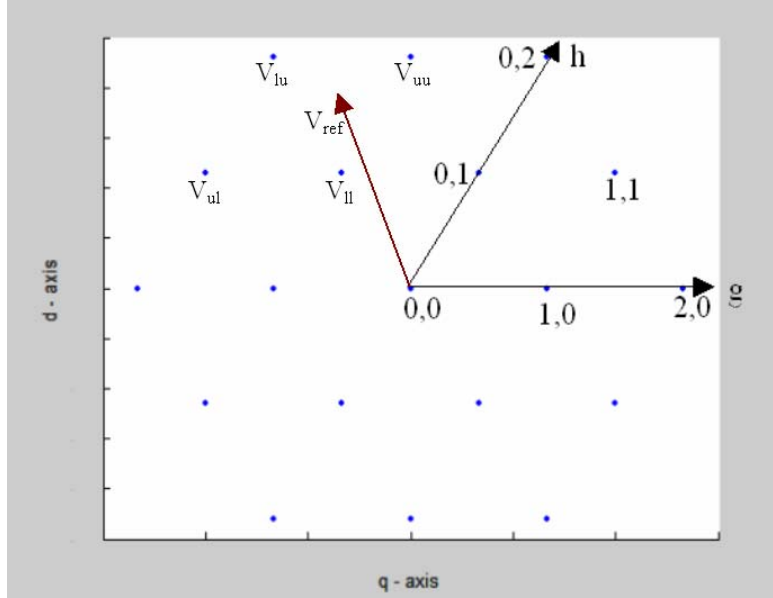
Figure 28.   Reference Vector in g-h Reference Frame

it can be seen that the four nearest vectors are simple combinations of upper and lower rounded integer values of the reference vector [17]. The four nearest vectors can be uncovered via the following equations [17]

$$\mathbf{V}_{ul} = \begin{bmatrix} \lceil \mathbf{V}_{refg} \rceil \\ \lfloor \mathbf{V}_{refh} \rfloor \end{bmatrix} = \begin{bmatrix} -1 \\ 1 \end{bmatrix}, \tag{4.10}$$

$$\mathbf{V}_{lu} = \begin{bmatrix} \lfloor \mathbf{V}_{refg} \rfloor \\ \lceil \mathbf{V}_{refh} \rceil \end{bmatrix} = \begin{bmatrix} -2 \\ 2 \end{bmatrix}, \tag{4.11}$$

$$\mathbf{V}_{uu} = \begin{bmatrix} \lceil \mathbf{V}_{refg} \rceil \\ \lceil \mathbf{V}_{refh} \rceil \end{bmatrix} = \begin{bmatrix} -1 \\ 2 \end{bmatrix}, \tag{4.12}$$

and

$$\mathbf{V}_{ll} = \begin{bmatrix} \lfloor \mathbf{V}_{refg} \rfloor \\ \lfloor \mathbf{V}_{refh} \rfloor \end{bmatrix} = \begin{bmatrix} -2 \\ 1 \end{bmatrix}, \tag{4.13}$$

39

where $\mathbf{V}_{*g}$ refers to the g component of the $\mathbf{V}_*$ vector, $\mathbf{V}_* = \mathbf{V}_{ul}, \mathbf{V}_{lu}, \mathbf{V}_{uu}, \mathbf{V}_{ll}$, or $\mathbf{V}_{ref}$, depending on the calculation, and $\lceil \bullet \rceil$ is the ceiling function and $\lfloor \bullet \rfloor$ is the floor function.

Next, one of the four nearest vectors is eliminated, leaving only three. Two of the three nearest vectors are always $\mathbf{V}_{ul}$ and $\mathbf{V}_{lu}$, and thus are not eliminated. That leaves $\mathbf{V}_{uu}$ or $\mathbf{V}_{ll}$ to be eliminated. The eliminated vector is determined by evaluating the sign of [17]

$$\mathbf{V}_{refg} + \mathbf{V}_{refh} - (\mathbf{V}_{ulg} + \mathbf{V}_{ulh}) . \tag{4.14}$$

If the sign of Equation (3.14) is positive, then $\mathbf{V}_{ll}$ is eliminated; if the sign is negative, $\mathbf{V}_{uu}$ is eliminated.

3.   Determination of the Duty Cycle

Although the determination of the three nearest vectors was simplified, the real value of this transform becomes apparent from a reduction in the duty cycle calculations. The new duty cycle calculations involve only simple addition and subtraction, eliminating the need for computationally hungry function calls such as sine and square root. The duty cycle calculations are expressed below [17].

If Equation (4.14) is negative,

$$d_{ul} \; = \; \mathbf{V}_{refg} - \mathbf{V}_{llg} \tag{4.15}$$

$$d_{lu} \; = \; \mathbf{V}_{refh} - \mathbf{V}_{llh} \tag{4.16}$$

$$d_{ll} \; = \; 1 - d_{ul} - d_{lu} \tag{4.17}$$

else, if Equation (4.14) is positive,

$$d_{ul} \; = \; -(\mathbf{V}_{refg} - \mathbf{V}_{uuh}) \tag{4.18}$$

$$d_{lu} \; = \; -(\mathbf{V}_{refg} - \mathbf{V}_{uug}) \tag{4.19}$$

$$d_{uu} \; = \; 1 - d_{ul} - d_{lu} . \tag{4.20}$$

4.   Transform Into Relevant Switching States

The final step is transforming the three nearest vectors back to usable switching states. Since the original transformation normalized the switching vectors to V_{dc}, $\mathbf{V}_{*g}$, and $\mathbf{V}_{*h}$ are elements of the set $\{-(n-1)\ldots, -1, 0, 1, \ldots, n-1\}$, where * represents either ul, lu, uu, or ll. The switching states are then solved for by satisfying the following equations [17]

40

$$S_A = k \qquad\qquad \text{where } k \in \{0, 1, ..., n-1\} \qquad (4.21)$$

$$S_B = k - \mathbf{V}_{*g} \qquad\qquad \text{where } k - \mathbf{V}_{*g} \in \{0, 1, ..., n-1\} \qquad (4.22)$$

and

$$S_B = k - \mathbf{V}_{*g} - \mathbf{V}_{*h} \qquad \text{where } k - \mathbf{V}_{*g} - \mathbf{V}_{*h} \in \{0, 1, ..., n-1\}, \qquad (4.23)$$

where S_A, S_B, S_C are the relevant phase switching states, and k is a free variable that is chosen to ensure that S_A, S_B, and S_C are $\in \{0, 1, ..., n–1\}$. Similar to the q-d reference frame, redundant switching states may be used for additional control parameters. Future work will involve eliminating the conditioning inverter power supply. Chapter V discusses the actual implementation of the equations.

E.   HYBRID ALGORITHM

Due to the complexity of SVM algorithms, a new hybrid control algorithm was created based on the g-h transform. In addition to being simpler than SVM, the hybrid algorithm also greatly reduces the digital spiking caused by DSPs in uncoupled control. Furthermore, while comparable in complexity to SPWM techniques, the hybrid algorithm has no requirement to generate the odd triplen harmonics to fully utilize the DC bus.

The hybrid algorithm is a cross between SVM and PWM. The desired waveform is transformed into the g-h reference frame. Once in the g-h reference frame, the next step is a direct conversion into an analog form of switching states S_A, S_B, and S_C. This is accomplished by dividing up the g-h reference frame into three equal sized sectors as shown in Figure 29.
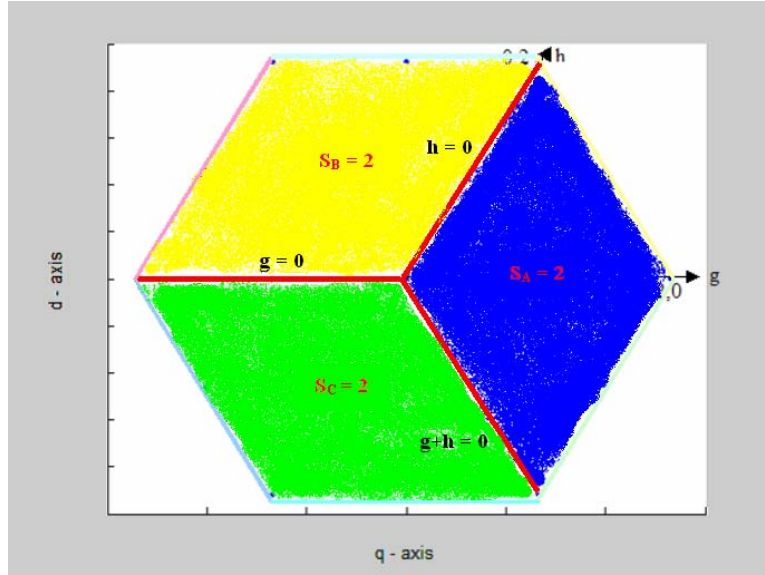
Figure 29.   Switch State Selection for Hybrid Algorithm

Each sector represents a different transform from the *g-h* vector to switching states. In each sector, one switching state is held constant while the other switching states are determined with Equations (4.22) through (4.24). However, instead of limiting the switching states to integer values, they can be continuous from 0 to *n*–1. These continuous switching states are then pulse-width modulated using stacked triangle waveforms to replicate the desired reference voltage vector.

The primary improvement of this algorithm over a SVM algorithm is continuous updating and ease of implementation. The proper output state is resolved within one DSP update cycle of the controller. This reduces digital spiking as discussed in Chapter III. Additionally, the primary improvement over straight SPWM is apparent with full DC bus utilization without the generation of reference odd-triplen harmonics.

F.   SUMMARY

This chapter covered two SVM algorithms and a hybrid algorithm that can be used to control multi-level inverters. The *g-h* based SVM control algorithm and the hybrid algorithm introduced in this chapter are both used to control the conditioning inverter of the 3x3 CMLC built at NPS. Chapter V goes into the actual implementation of the algorithms utilizing the dSpace controller and Simulink software.

V. IMPLEMENTATION OF ALGORITHMS

A. OVERVIEW

This chapter discusses in detail the programming of the system. The program is broken up into three sections: the bulk inverter controller, the conditioning inverter controller, and the hardware interface. The hardware interface refers to both the hardware simulations and the hardware communications. Since dSpace was used, all programming was done using Simulink. This provided a fast way to test various models and make easy program changes.

B. BULK CONVERTER CONTROLLER

1. Bulk Converter

Since there is only one dSpace module, the bulk inverter controller was part of the same Simulink program as the conditioning inverter controller. Although the programs were run by the same DSP, they did not communicate with each other inside the program blocks, ensuring the validity of uncoupled control. Figure 30 shows the bulk inverter block diagram in Simulink for phase A.
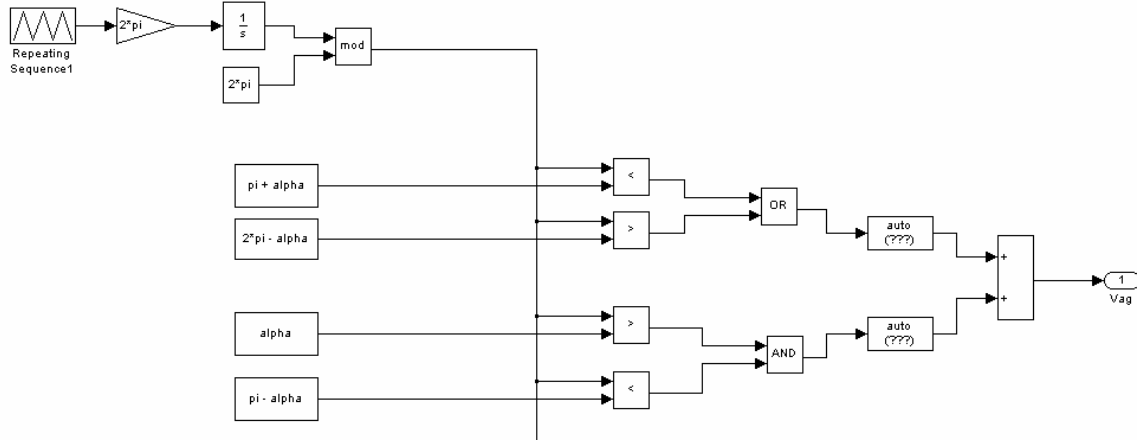

Figure 30. Bulk Converter v_{ag} Switch State Generator

The desired bulk inverter frequency was fed into an integrator to create a timer. This bulk inverter frequency could be either a steady state frequency or a varying frequency. To create a varying frequency, which was used to test the tracking ability of the reference sine-wave generator, the input frequency was a repeating sequence that created a triangle waveform varying between 10 and 20 Hz over a period of 1 s as shown in Fig-

ure 30. The mod function was then applied to the timer output to create a sawtooth wave-

form that went from 0 to 2π at the input frequency. This allowed the switching states of

the bulk inverter to be selected through simple comparisons. Figure 31 shows the output

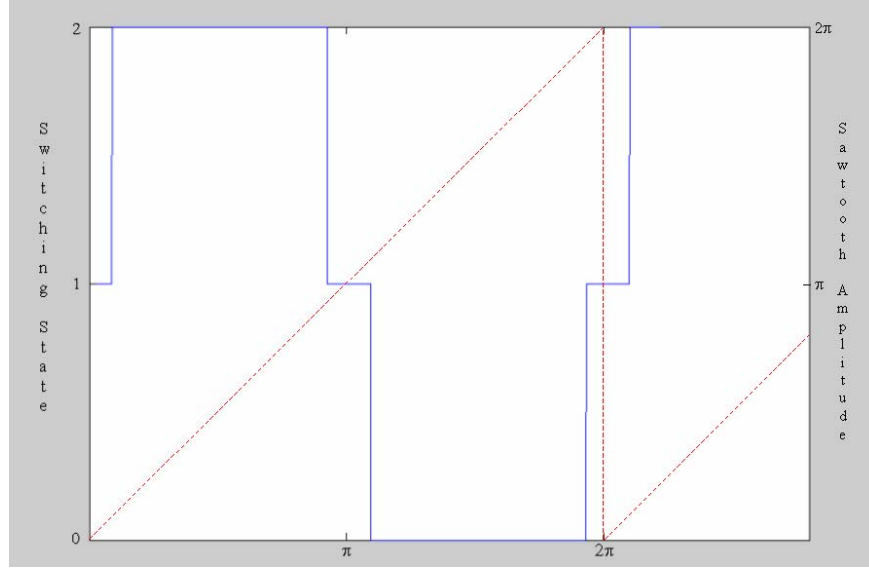waveform for v_{ag} and the generated saw tooth waveform.

Figure 31.   Bulk Converter v_{ag} Output with Overlying Control Saw tooth

The desired output is chosen based on the Table 2 below.

Range	Output State
$0 - \alpha$	1
$\alpha - (\pi - \alpha)$	2
$(\pi - \alpha) - (\pi + \alpha)$	1
$(\pi + \alpha) - (2\pi - \alpha)$	0
$(2\pi - \alpha) - 2\pi$	1

Table 2.   Bulk Converter Output States for Phase

The rest is simple logic. The auto blocks automatically convert data passing from one

block to another into the right type (i.e., Boolean to Floating Point in this case). Finally,

the summer block was used to simplify the logic and create an integer output from 0 to 2.

Phase B and Phase C are built using the same logic, except with a phase delay of 120º

and 240º, respectively. For the software simulations, the switching states were converted

to voltages by multiplying the output state for each phase voltage by $V_{dc}/2$.

2.   Reference Sine Wave Generation

Although not explicitly part of the bulk controller, the reference sine wave gen-

erator is discussed here because it operates on the bulk inverter output. As discussed in

44

Chapter II, generating the reference sine wave from the bulk inverter is key to operating the CMLC as an uncoupled system. Instead of filtering the bulk inverter output, an integrator was used to time specific switching states. The time t was then used to calculate the frequency. By doing this, the reference sine wave frequency can be updated up to twelve times during a single bulk inverter period. By updating the frequency more often, better dynamic response is gained. However, this also leads to less accurate calculations because the error of the calculations increase when shorter output states are timed. Conversely, the error can be reduced by either updating the frequency less often, resulting in longer timed sections, or by using a faster DSP. In order to try to maximize the response, and minimize the error of the calculations, the reference sine wave frequency was updated six times in one period for this thesis, twice per phase as shown in Figure 32.
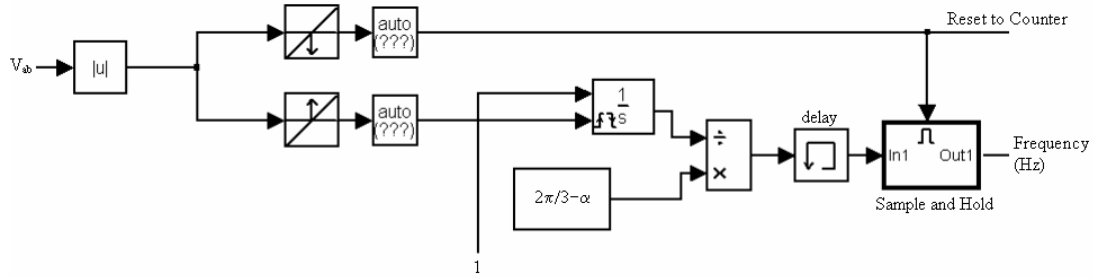

Figure 32.   Frequency Calculation

The above figure is only for v_{ab} but is identical for v_{bc} and v_{ca}. First, the absolute value of the normalized line-to-line voltage is found, creating the waveform shown in Figure 33.
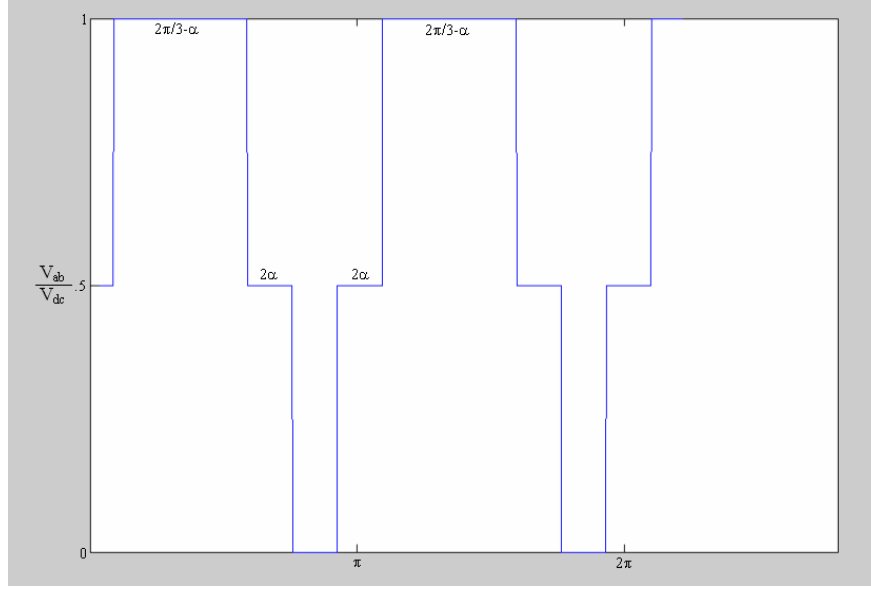
Figure 33.   Absolute Value of Normalized Line-to-Line Voltage

The next step detects a rising and falling edge at a value of 0.7. The value of 0.7 was chosen to prevent noise from triggering the edge detectors. At this point, the rising edge detector resets the integrator and starts timing the bulk inverter output state. The falling edge detector acts as a trigger to a sample-and-hold block. This block captures the frequency calculated by Equation (3.8). There is one additional block; this is a single- cycle delay. It was found that the sample-and-hold trigger would capture the frequency value a cycle too late. This resulted in an erroneous frequency, thus the single cycle delay was added.

The falling edge detector for v_{ab} is also used to reset a counter which keeps track of the phase (A, B or C) providing the frequency. The remaining two falling edge detectors (on the other line-to-line voltages) act as a clock for the counter. Figure 34 shows the counter and multiport switch that select the most up-to-date calculated frequency.
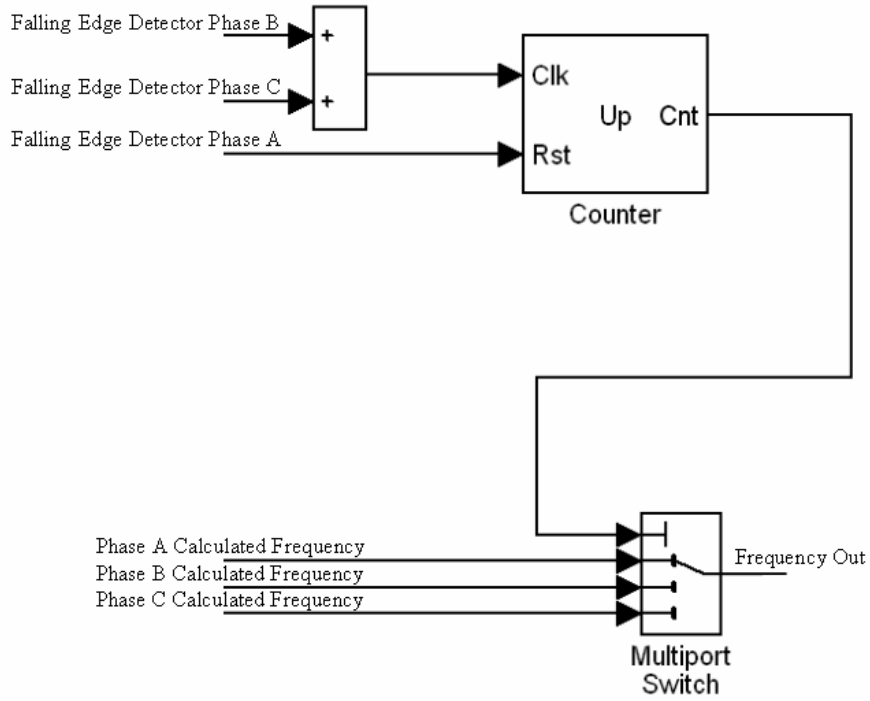
46

Figure 34.   Frequency Selection

The counter is reset with a falling edge of phase A. This sets the output to zero, which corresponds to the first input of the multiport switch. Next the phase B detector triggers, which sets the counter output to "1", and selects the phase B calculated frequency. This process repeats for phase C, and then resets with the second falling edge of phase A. Calculating the frequency for a single phase multiple times would have been a simpler implementation. However, with a slow DSP, the frequency calculations for shorter output states ($V_{ab}/V_{dc} = 0.5$ or 0) would not be as accurate.   Optionally, the system could be set up to update the frequency three times per cycle, once per phase. This option would result in a better steady-state response due to longer timed states (less error in the calculations), but less dynamic response due to fewer frequency updates. To minimize the error and maximize the dynamic response, the frequency was updated six times per cycle.

With the frequencies calculated, the final step is generating the sine wave and putting it in phase with the bulk converter waveform. This is illustrated in Figure 35.
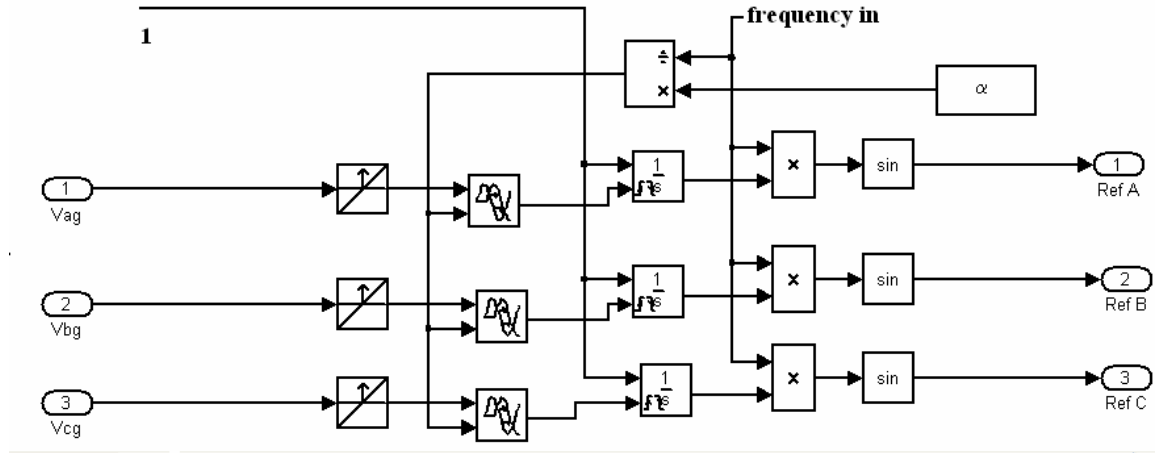
47

Figure 35. Generation of In-Phase Sine Wave

The rising edge of the bulk inverter line-to-ground voltages is used to trigger an integrator. As in previous blocks, the integrator is employed as a timer. The integrator output is multiplied by the calculated frequency ω. This product is then operated on by a sine function, resulting in the desired sine wave. Since the timer starts with the rising edge of the bulk converter, it is out of phase by the control angle α. This is fixed by using a variable phase delay block on the triggers. Since the bulk inverter frequency can change, the time delay is found by dividing α (in radians) by the calculated ω. With the sine wave generated, it is then normalized to the commanded output voltage. Since the maximum output of the CMLC is related to the control angle α by Equation (3.1), the sine wave is multiplied by the value of Equation (3.1). This is done with a simple gain block not shown above.

C.   CONDITIONING CONTROLLER CONVERTER

Three algorithms were considered for use with the conditioning converter; their theory is discussed in Chapter III. However, due to the complexity of implementation of the SVM algorithm in the *q-d* reference frame, only two were implemented. The first is an SVM algorithm in the *g-h* reference fame with a reset that resets the SVM cycle when the bulk inverter changes state. The second is the hybrid algorithm based on the *g-h* transform. The SVM algorithm is presented first. Even with the simplification by using the *g-h* reference frame, it is still complex when compared with the hybrid algorithm.

1. SVM Algorithm

Since both algorithms use the *g-h* transform, the transform block is only presented in this section. Chapter III discussed the transform in detail, but the implementation is slightly different since both the bulk inverter output voltages and the reference sine waves were normalized to V_{dc}. Figure 36 shows the transform.
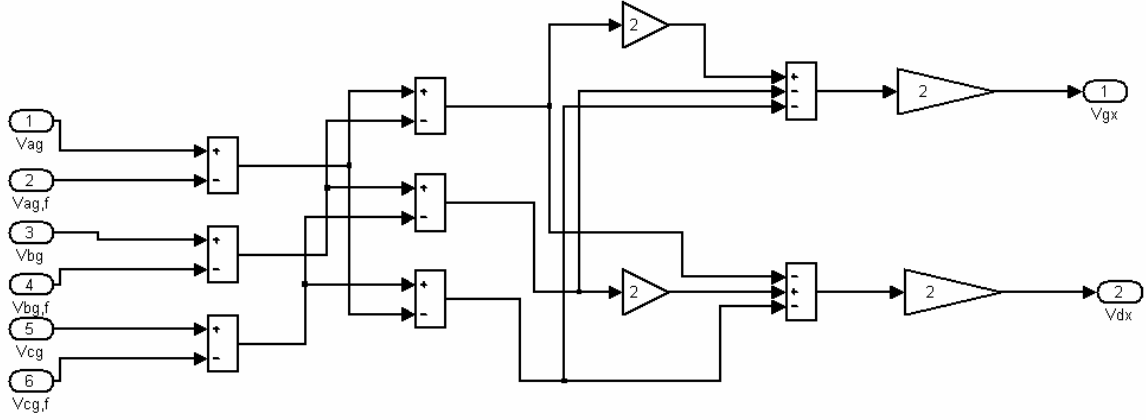

Figure 36.   *g-h* Reference Frame Transform

The commanded voltage for the conditioning converter was found by [2]

$$v_{*g} - v_{*g,f} = v_{*x} \tag{5.1}$$

where v_{*g} is the bulk inverter phase voltage , $v_{*g,f}$ is the reference sine wave, and v_{*x} is the conditioning inverter commanded phase voltage. Once the commanded phase voltages are known, the voltages are then converted into line-to-line voltages. With the commanded voltages in line-to-line terms, they are then transformed according to Equations (4.7) and (4.8) to find the *g-h* values. An additional gain of two was necessary since the line-to-ground voltages were used vice the line-to-neutral voltages. Finally, V_{gx} and V_{dx} are used as the commanded inputs for the conditioning inverter SVM and hybrid algorithms.

The next block is the software reset block, which was used to demonstrate the ability to reduce the digital spiking. Ideally, an edge detector circuit tied to the bulk inverter outputs would be used as the reset signal. Since an edge detector circuit was not readily available, a software-reset block was created to validate the concept. Figure 37 shows the software interrupt block.
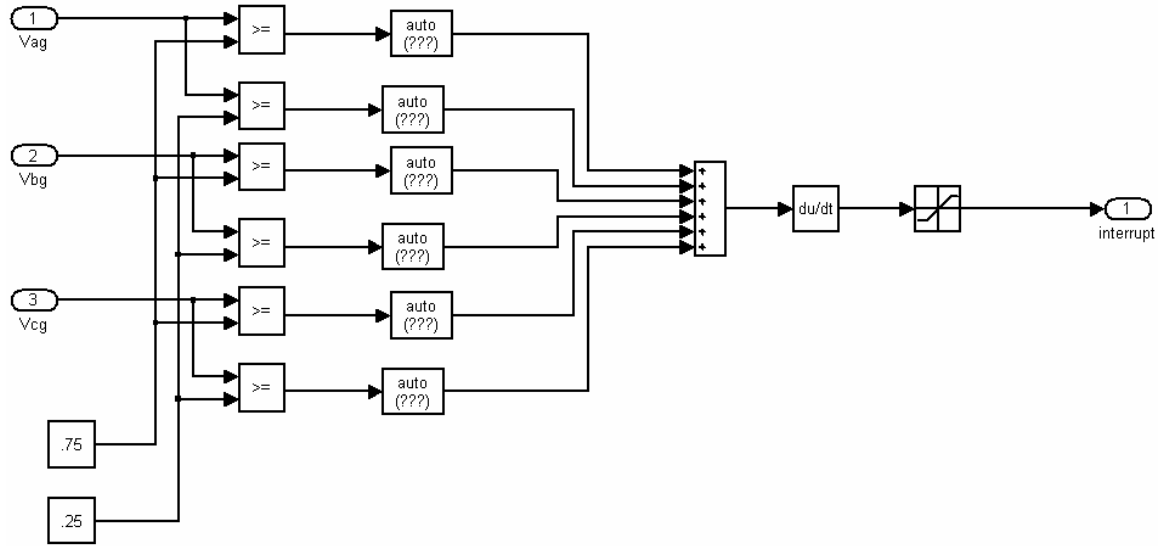
Figure 37.   Software-Reset Block

To create the reset signal, the normalized bulk inverter outputs were ran through comparators set to detect output voltage changes. The comparator outputs were then summed together and run through a derivative block. The derivative block creates a digital pulse for each change in voltage. The output of the derivative is limited to between 0 and 1. This signal is then used to reset the SVM cycle when the bulk inverter changes state.

With the basics done, the next step involved the actual SVM algorithm, which starts with the detection of the three nearest vectors. This is done exactly as it was shown in Equations (4.9) through (4.13). Figure 38 shows the Simulink code for detecting the vectors.
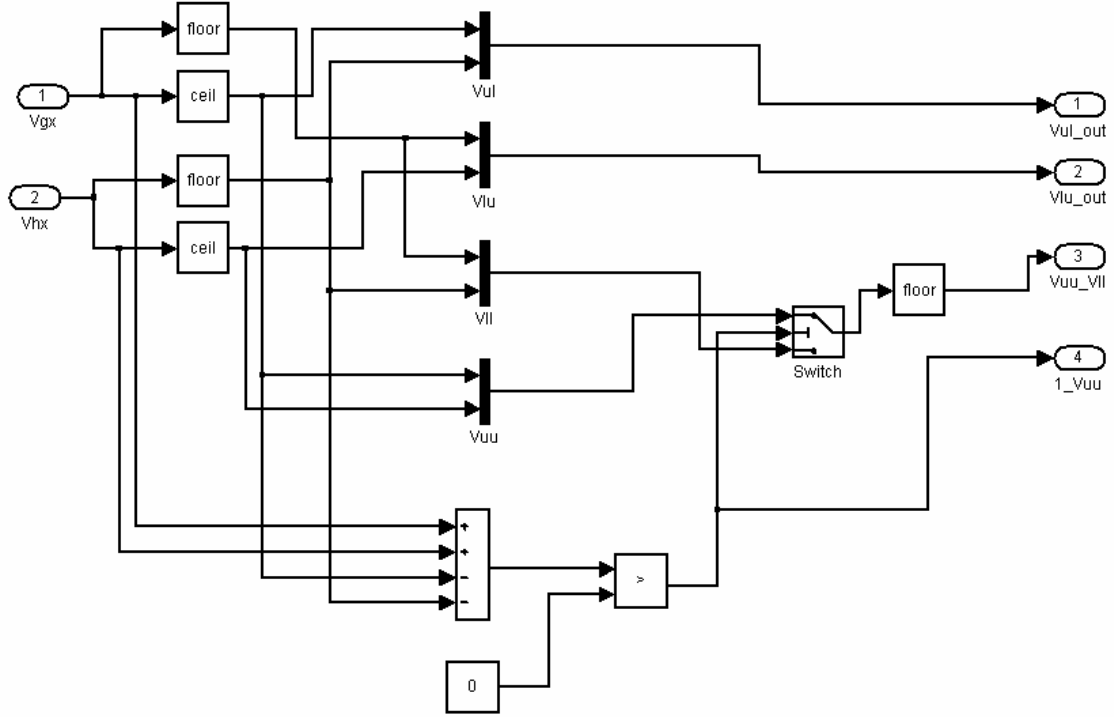
Figure 38.   Three Nearest Vector Detection

There are four outputs: V_{ul_out}, V_{lu_out}, $V_{uu\_}V_{ll}$, and 1_V_{uu}. V_{ul_out} and V_{lu_out} are self-explanatory and represent two of the three nearest vectors. $V_{uu\_}V_{ll}$ is either the V_{uu} or V_{ll} vector depending on the sign of Equation (4.14). The 1_V_{uu} output holds a value of "1" if the $V_{uu\_}V_{ll}$ vector is V_{uu}, and a value of "0" when the $V_{uu\_}V_{ll}$ vector is V_{ll}. This is important for the duty cycle calculations. If the value is "1", Equations (4.18) through (4.20) are used to calculate duty cycles, otherwise, Equations (4.15) through (4.17) are used. Figure 39 shows the code for calculating the duty cycles.
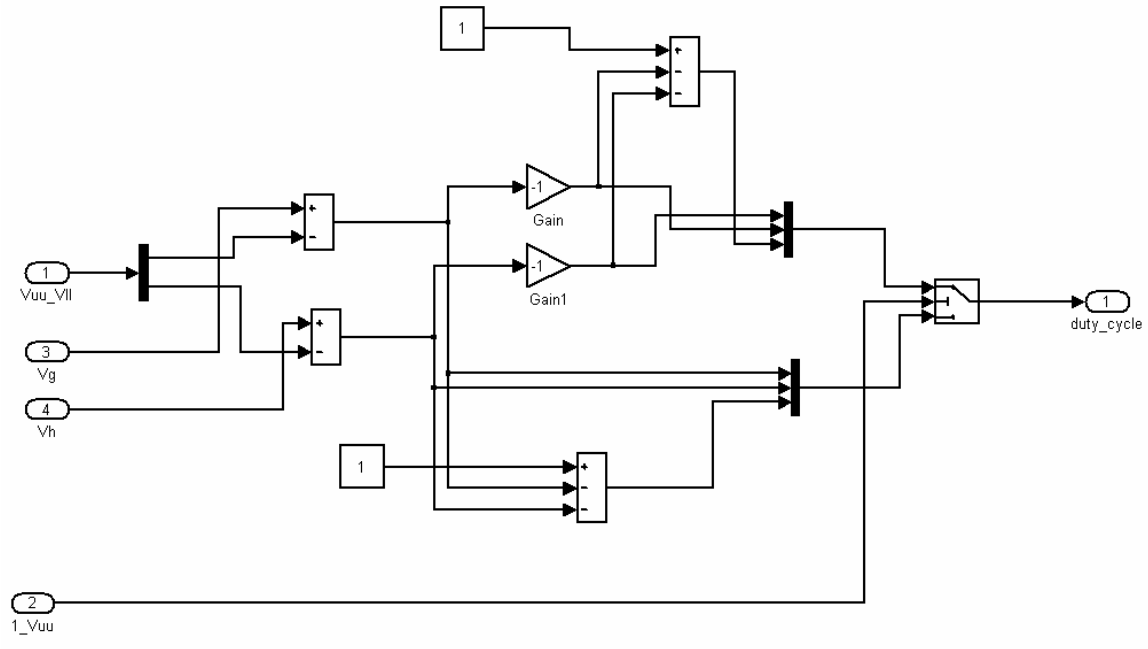
Figure 39.   Calculation of Duty Cycles

Once again, the Simulink blocks were programmed to precisely follow the equations. The duty cycle is output as a vector of $[d_{ul}\ d_{lu}\ d_{ll}\_d_{uu}]^{T}$. It is important to note that these duty cycle calculations are continuously updated at the DSP update rate, and not the SVM frequency. This fact, in conjunction, with the reset allows a near instantaneous change in the conditioning inverter output when the bulk inverter switches state.

In order for SVM to work, the duty cycle vector and the output vectors must be held constant for the duration of the SVM period. This is accomplished by utilizing two triggered output blocks as shown in Figure 40a and Figure 40b. Figure 40a is the vector hold block and Figure 40b is the duty cycle hold block.

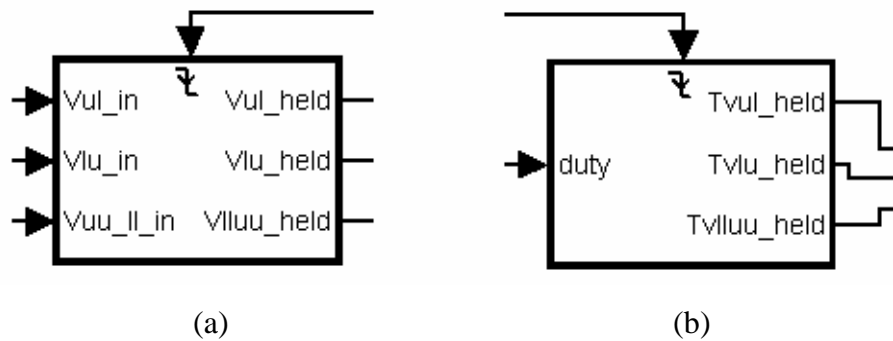(a)   (b)

Figure 40.   (a) Vector Hold Block and (b) Duty Cycle Hold Block

The blocks are triggered by either one of two sources. The first trigger source is the SVM clock. The second source is the reset signal generated by the software-reset block.

   With the signals generated, the appropriate switch states need to be selected and modulated accordingly. To do this, the individual duty cycles were compared to a saw tooth waveform (PWM ramp) operating at the SVM frequency. Figure 41 shows the code used to compare the individual duty cycles with the PWM ramp.
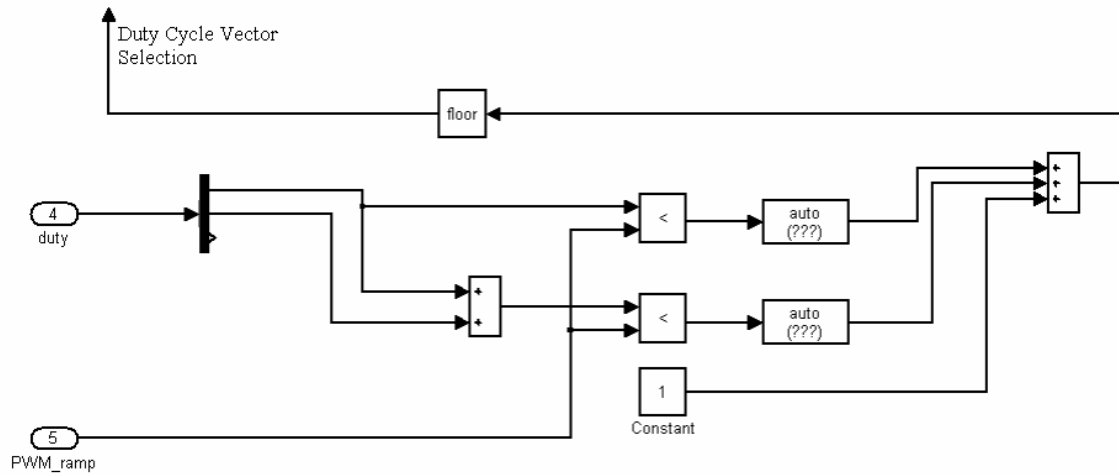

Figure 41.   Duty Cycle Vector Selection

   The three vectors ($\mathbf{V}_{ul}$, $\mathbf{V}_{lu}$, and $\mathbf{V}_{uu\_ll}$) were input into a multiport switch, shown in Figure 42. The *Duty Cycle Vector Selection* output of Figure 41 is used as the switch selector. The output is initially set to "1", which selects the first input, $\mathbf{V}_{ul}$. When the PWM ramp exceeds the value of d_{ul}, the comparator output changes to $\mathbf{V}_{lu}$. After the PWM ramp rises above the value of d_{lu}, the other comparator switches, causing the multiport switch to output the $\mathbf{V}_{uu\_ll}$ vector. When the PWM ramp reaches "1", it resets to "0", forcing the output back to the initial vector, $\mathbf{V}_{ul}$.

   Converting the vectors from the *g-h* reference frame into valid *abc* reference frame switch states was a little more complex. Figure 42 shows the switch state selection.
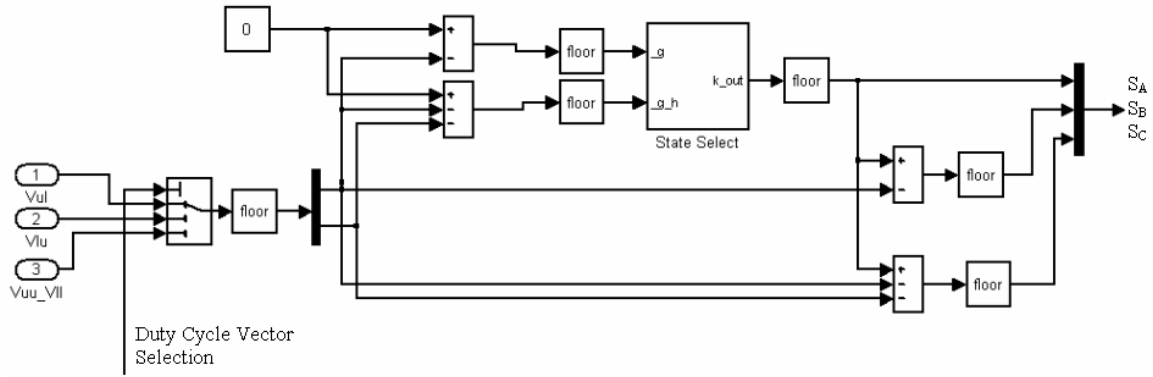
53

Figure 42.   Switch State Selection

Once the multiport switch selects the vector, the vector is broken up into its *g* and *h* components. The next step is to find *–g*, and *–g–h*, which is done using simple addition/subtraction blocks. The values of *–g* and *–g–h* are used to uncover the initial output for S_A. It was found that S_A (or *k*) can be easily found by evaluating *–g* and *–g–h* as follows.

If

$$-g \text{ and } -g-h \le 0 \text{ then } S_A = 2, \tag{5.2}$$

else if

$$-g \text{ and } -g-h \ge 0 \text{ then } S_A = 1, \tag{5.3}$$

else

$$S_A = 0. \tag{5.4}$$

The state select block makes the above evaluations. Once S_A is known, S_B and S_C are found simply by using Equations (4.23) and (4.24).

With the switching states known, they are then decoded to uncover the actual switch "on/off" values using a switching state decoder that is discussed in the last section of this chapter. This decoder was also detailed in Reference 7. The decoded values are used to operate the CMLC switches. Figure 43 shows the complete layout in Simulink of the SVM algorithm.
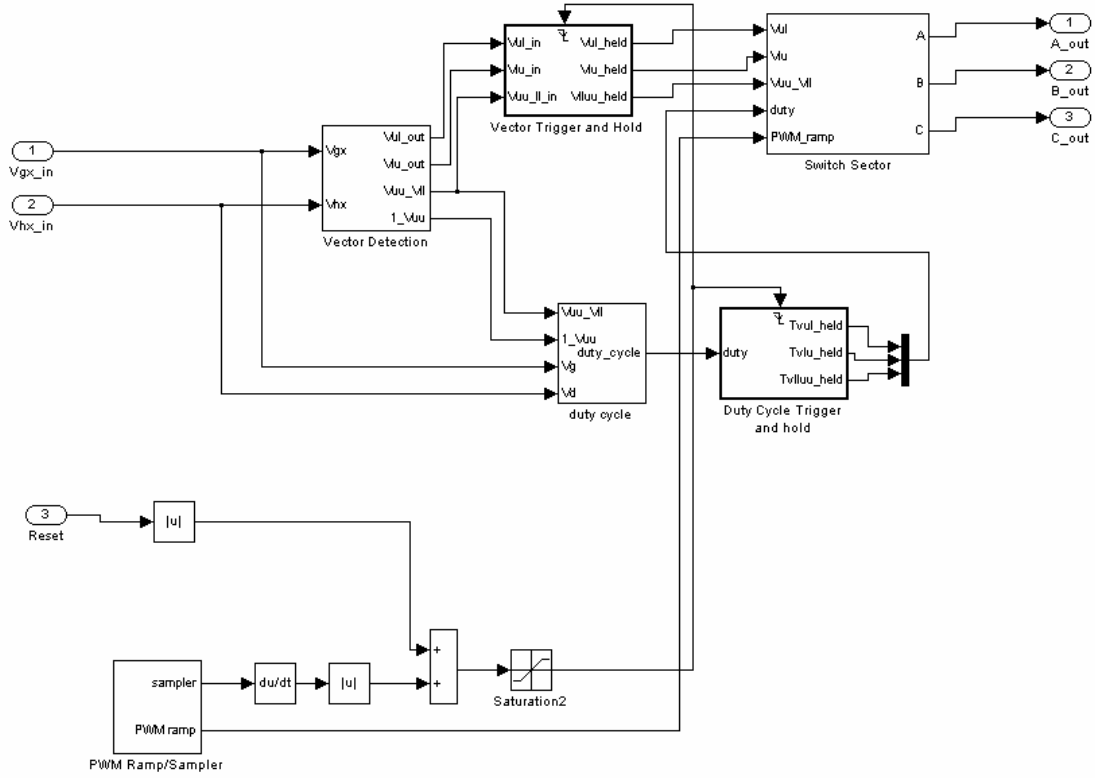
Figure 43.   Block Diagram for the SVM Algorithm

2.   **Hybrid Algorithm**

The hybrid algorithm is simpler to implement when compared with the SVM algorithm. It combines the simplicity of SPWM with the benefits of SVM. The key to using this algorithm is the *g-h* transform, which was described in Chapter III. After transforming into the *g-h* reference frame, the next step is to determine the sector of the operational reference as described in Chapter III. Figure 44 shows the sector detection code.
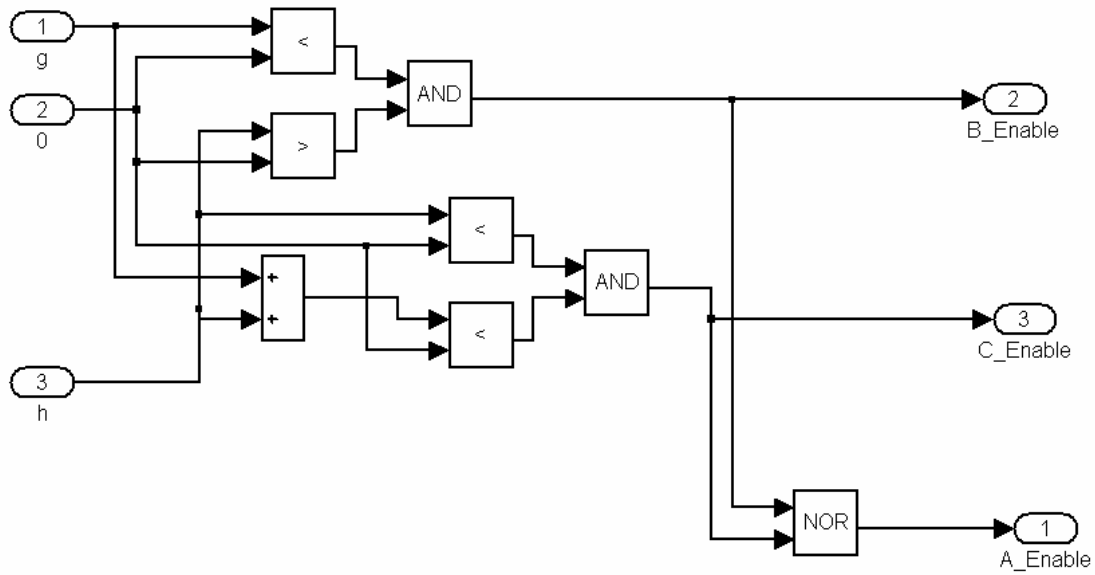
Figure 44.   Sector Selection

This is an easy evaluation since the three line equations are $g = 0$, $h = 0$, and $g+h = 0$. By comparing the reference vector with these equations, the sector can be determined. Depending on the sector, one of the outputs (*A_Enable*, *B_Enable*, or *C_Enable*) is set to one.

With the enables determined, the next step is finding the analog values of the switching states. Figure 45 shows the layout for determining the analog switching states.
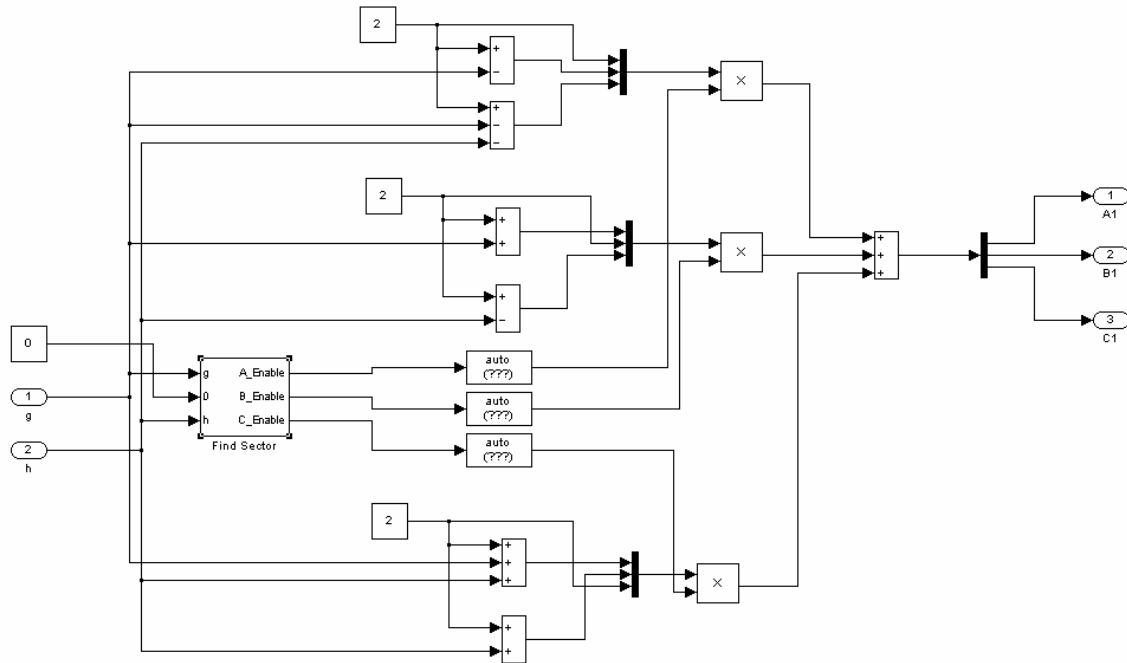
Figure 45.   Hybrid Algorithm

The analog switching states are created by setting each switch to two, and then calculating the others using Equations (4.22) through (4.24). The enables from Figure 44 only allow one set of the switching states to the outputs, *A1*, *B1*, and *C1*. These values are then utilized for the PWM, as shown in Figure 46.
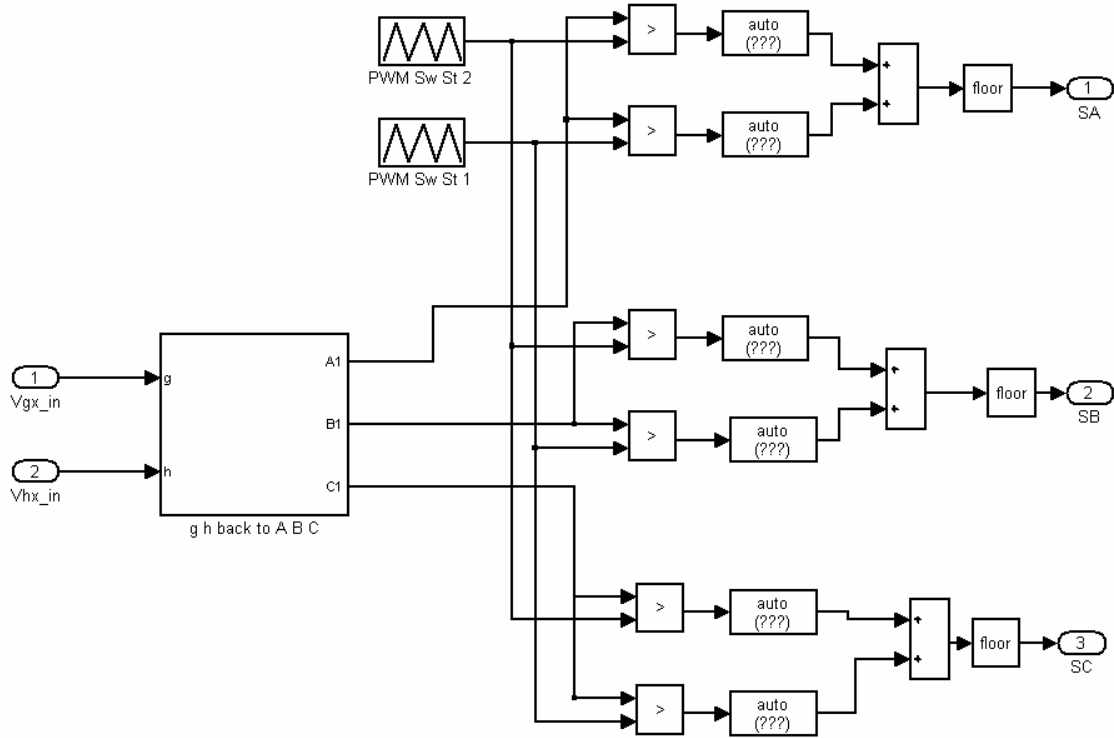
Figure 46. Hybrid Algorithm Pulse Width Modulation

The outputs, *A1*, *B1*, and *C1* are then PWM using triangular waveforms as was done for the SPWM technique discussed in Chapter II. This PWM output is then fed into the switching state decoder blocks discussed later in this chapter. The decoded values are used to operate the CMLC switches.

D. HARDWARE INTERFACE

1. Hardware Communications

In order to implement the two algorithms, the bulk inverter output voltages and the DC bus voltage had to be read in. The bus voltage V_{dc} was needed for two things. First, V_{dc} is used to normalize the bulk converter phase voltages, v_{ag}, v_{bg}, and v_{cg}. Second, V_{dc} is important for implementing capacitor voltage-balancing strategies and eliminating the secondary power supply. Neither capacitor voltage balancing nor secondary power supply elimination was done in this thesis, but will be implemented in a follow-on thesis.

dSpace provides its own toolbox of Simulink tools. This made it simple to read in the analog voltages from the dSpace DSP I/O Board. Figure 47 shows the dSpace Simulink A/D communication blocks.
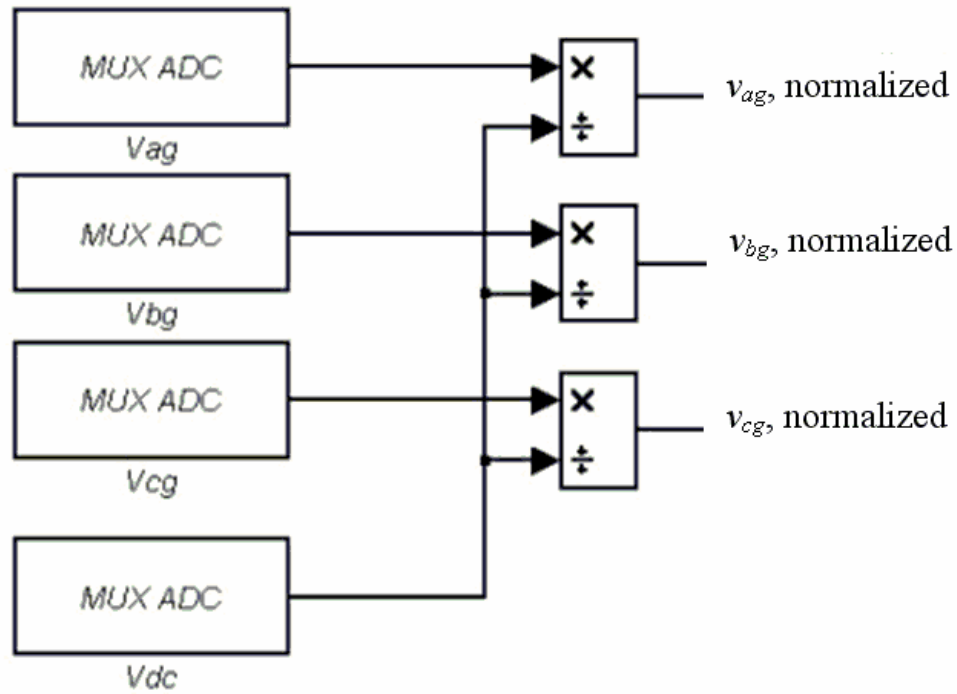
58

Figure 47.   dSpace ADC Interface Blocks.

The switch state decoder used in Reference 7 was also needed. Figure 48 shows the outer block for switch state decoding. This is only discussed briefly here since it is covered in detail in Reference 7.
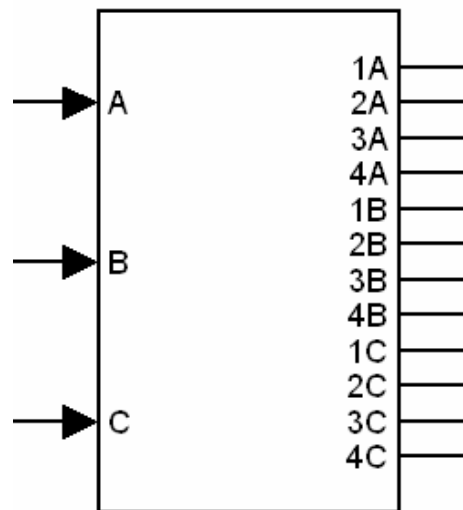

Figure 48.   Switching State Decoder

The inputs, *A*, *B*, and *C*, correspond to the three phases of the system. Since the switching state decoder block was designed for the NPS 3x3 CMLC, the inputs accept values of "0", "1", or "2". This block takes the three inputs, and decodes them into actual switch on/off states. Because there are four switches per phase per converter, there are four outputs per phase. These outputs are either "1" or "0", corresponding to "on" or "off". Table 1 of Chapter I shows the relation between switching states and switch values for a nine-level inverter. Table 3 below shows the relation between switching state and switch values for a single converter phase of the NPS 3x3 CMLC.

State	Switch 1	Switch 2	Switch 3	Switch 4
0	0	0	1	1
1	0	1	1	0
2	1	1	0	0

Table 3.   Switching State Decoder Table

With the switching states decoded into binary, they were then output through the dSpace I/O board. Fortunately, dSpace provided a block to communicate with the digital I/O board. Figure 49 shows the dSpace block used.
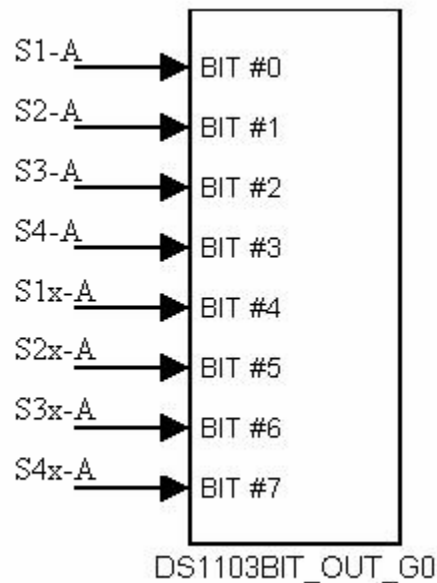

Figure 49.   Phase A Switch Interface for Bulk and Conditioning Inverter.

60

This block is only for a single phase of both the bulk inverter (*S*A*) and the conditioning inverter (*S*xA*). Two additional blocks were also used for both phase B and phase C.

2. Hardware Simulation

To simplify the simulations, ideal components were used. Figure 50 shows the CMLC simulation block.
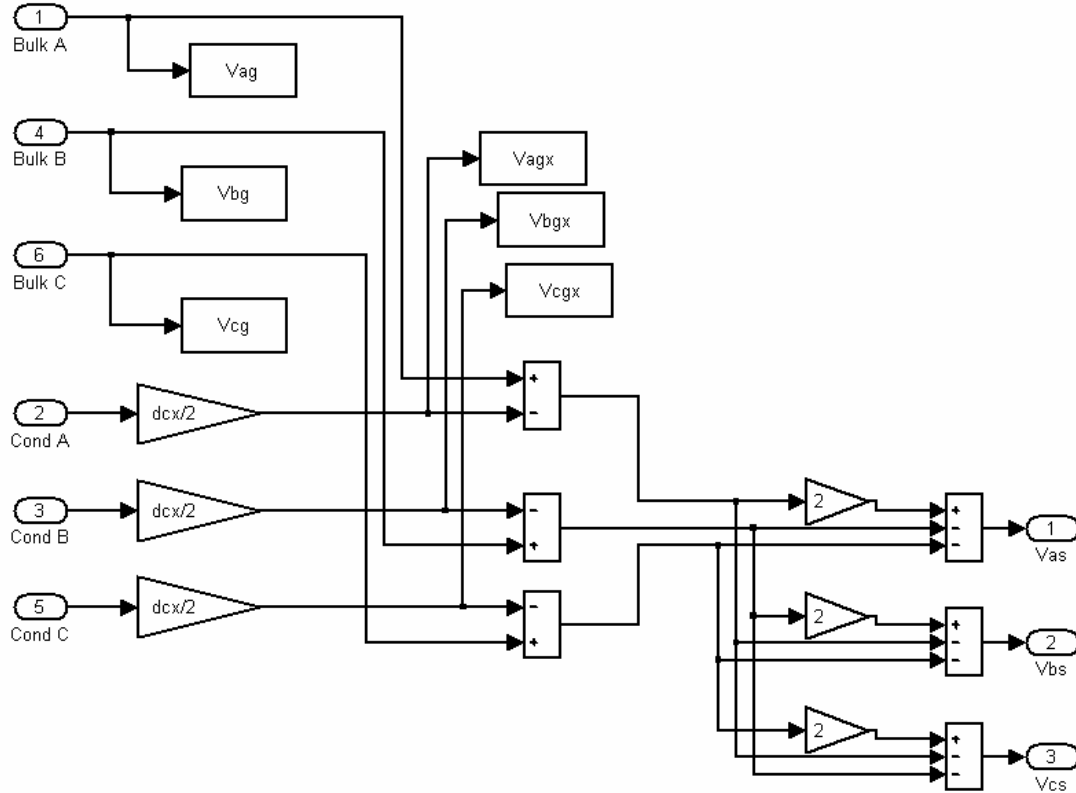

Figure 50. CMLC Simulation

For the simulations, the bulk inverter output was already in terms of the bus voltage. However, the conditioning inverter outputs were not, thus a multiplication by $V_{dcx}/2$ was necessary. The conditioning inverter voltages were then subtracted from the bulk inverter voltages to create v_a, v_b, and v_c. In order to get them in terms of v_{as}, v_{bs}, and v_{cs}, Equation (2.1) was used and is implemented above.

The motor was simulated using a simple three-phase RL load. The values were determined by measuring the phase resistance and inductance of actual 1/4-HP motor.

The measured resistance and inductance were 12 Ω and 6.6 mH, respectively. This motor modeling simplification made algorithm verification easier.

E.   SUMMARY

This chapter covered the coding necessary to run the algorithms. dSpace greatly simplified the coding by allowing the use of Simulink to create the models and then download them into the DSP card. The dSpace HIL system made control strategy changes easy via quick program modifications rather than hardware changes. Chapter VI utilizes this code to do both simulations and run hardware tests.

VI.   RESULTS

A.   OVERVIEW

Prior to testing the actual 3x3 CMLC hardware, simulations of the hardware were used to fine-tune the control algorithms. The uncoupled control algorithms, along with the ideal model of the CMLC with motor load (a series connected 6.6-mH inductance and 12-Ω resistance) were simulated in Simulink. The ideal model is laid out in Chapter V. Results were evaluated using Matlab. The evaluation criteria consisted of the THD of the output current and voltage, and the spike width observed in the voltage.

After the initial simulations, the system was then tested with the actual hardware built at NPS. The CMLC was used to power a 1/4-HP (208 V_{ll}, 1.2 A), 3-phase, wye-connected, 60-Hz induction motor. The motor was initially operated at 10 Hz and no load. The algorithms were tested with a DSP update frequency of 18 kHz, and a switching frequency of 3.6 kHz. In order to test the tracking ability of the reference sine wave generation, the bulk inverter frequency was varied from to 10 to 20 Hz. Final testing involved comparing the previously developed, joint controlled SPWM algorithm against the uncoupled controller using the hybrid algorithm developed in this thesis for the conditioning inverter. The comparison testing was done operating the motor at 60 Hz, under full load (1/4 HP). The hybrid algorithm was chosen due to its implementation simplicity. Since the algorithm required less calculations then the original, the DSP update frequency could be increased to improve results. The operating frequency of the motor was increased six fold (from the initial starting point of 10 Hz). This required the DSP update frequency to be increased for like comparisons. However, the DSP update frequency could only be increased to 30 kHz, the limit of the 20-MHz DSP card with the uncoupled controller programming. To further improve results the switching frequency was increased to 7.2 kHz. This provided results comparable with the 10 Hz tests. Measurements for the hardware tests were obtained using the Tektronix TDS3012B digital oscilloscope and the HP3561A spectrum analyzer.

B.   SIMULATIONS

The algorithms and hardware model were programmed in Simulink. Figure 51 below shows the overall Simulink block diagram for the entire system with load. For a detailed description of the blocks, please refer to Chapter V.
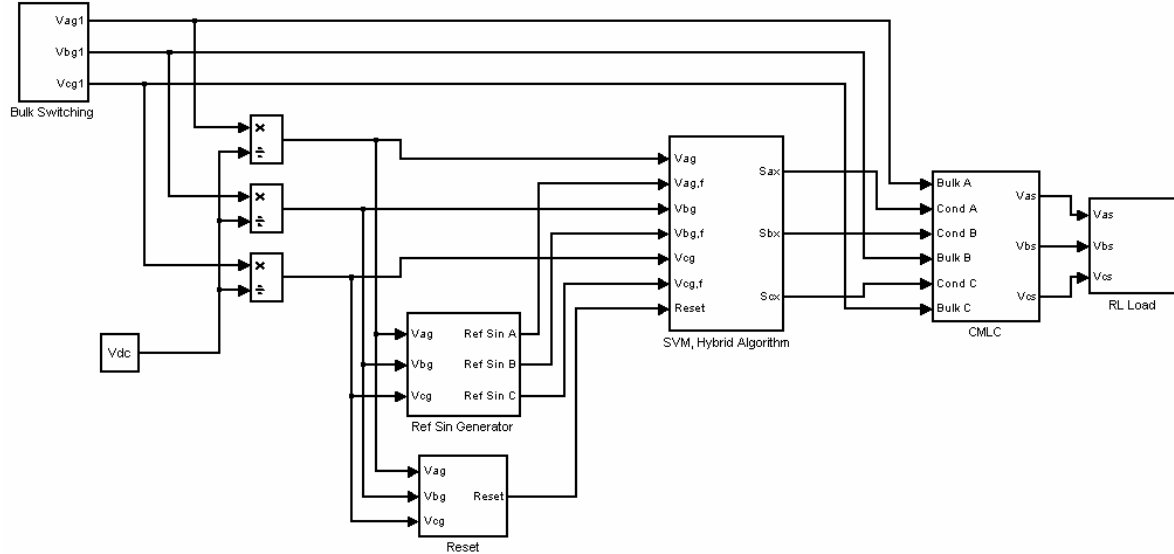

Figure 51.   Simulated System

1.   SVM Simulations

Figures 52 and 53 depict the output current with frequency spectrum and a blow-up view of the transition spike for the conditioning inverter using the SVM algorithm without the reset. The first 60 harmonics are contained in Figure 52.
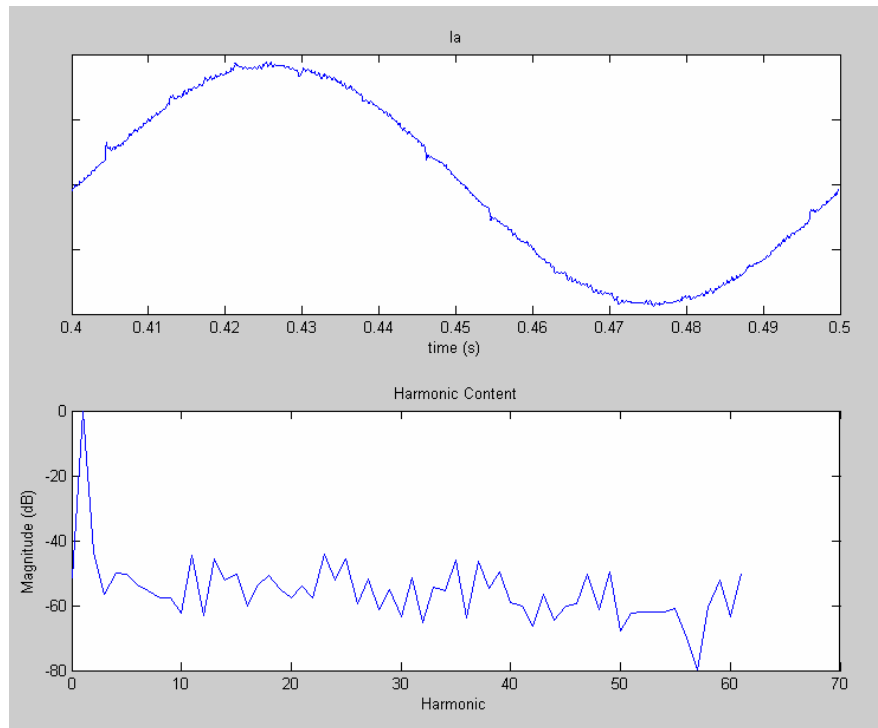
Figure 52.   Current Simulation Results for SVM Algorithm w/o Reset
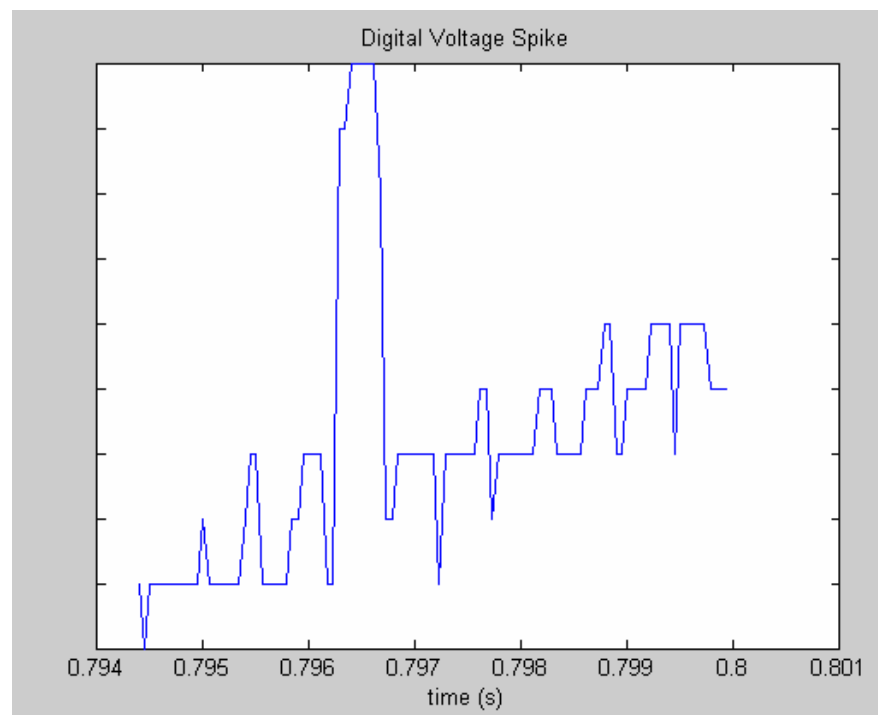

Figure 53.   Voltage Spike Simulation for SVM Algorithm w/o Reset

The calculated THD using Matlab was 1.97% for the first 60 harmonics. The spike width was measured to be 480 μs. These measurements are used as a basis of comparison for the other algorithms.

The next set of simulations was done for the system with the conditioning inverter controlled by the SVM algorithm using the reset to reduce spike width. Figures 54 and 55 below show the current waveform with THD and the voltage spike width, respectively.
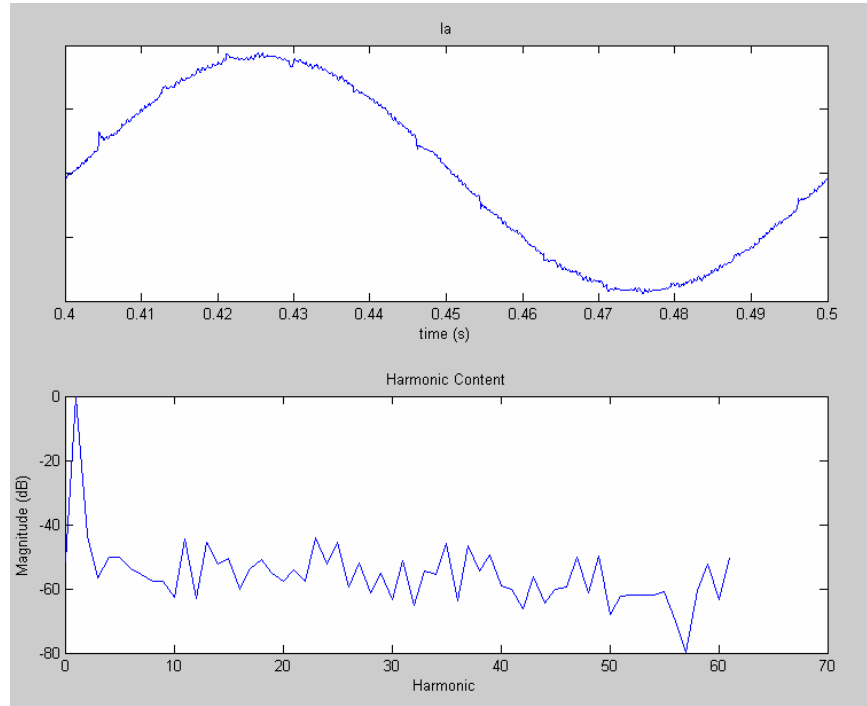

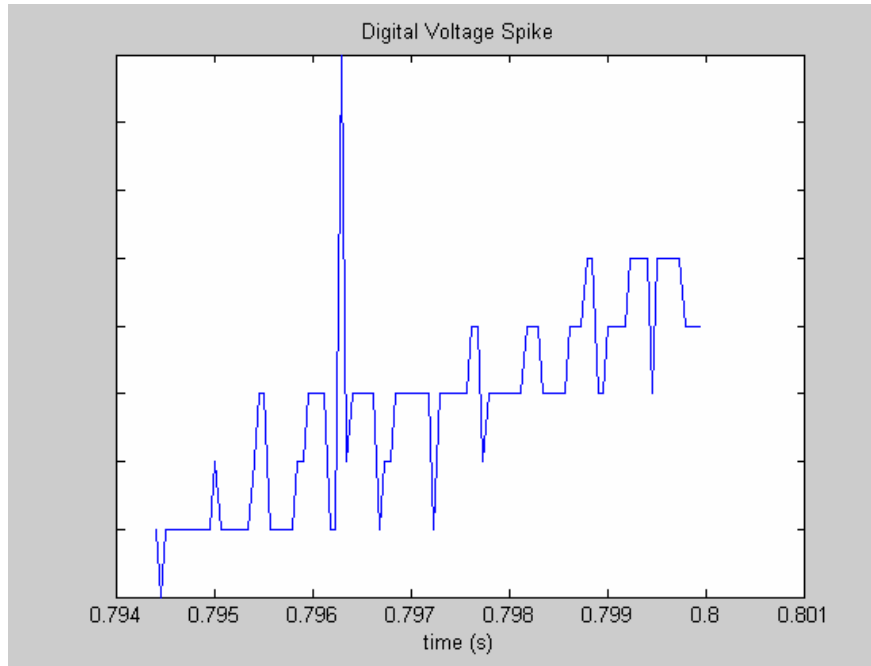Figure 54.   Current Simulation Results for SVM Algorithm with Interrupt

Figure 55.   Voltage Spike Simulation for SVM Algorithm with Reset

The current THD was also 1.97%. This was unexpected and is discussed below. The spike width was reduced to 105 μs, which is well within the expected range of less than two DSP update cycles (111 μs).

To obtain a further understanding of the harmonic distortion introduced by the spikes, the spectrum of two created sine waves with similar spike widths were evaluated. One sine wave had a spike duration of 83 μs and the other had a spike duration of 417 μs. Figure 56 shows the waveforms and the harmonic distortion.
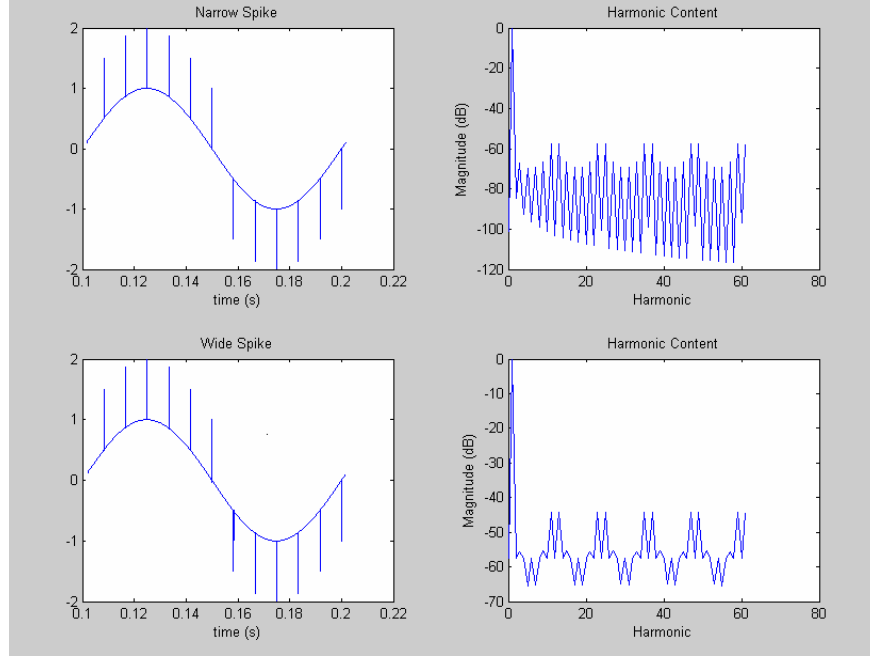
Figure 56.   Harmonic Distortion for Different Spike Widths

The THD for the narrow spike is 0.45% while the wide spike THD is 2.16%. This suggests that there should be some difference in the THD between the two algorithms.

With this known, further simulations were run to determine the error in THD calculations. The problem appeared to be a resolution issue. Therefore, the simulations were rerun with a step size 10 times smaller than the original 55.6 μs. This new arrangement required a phase delay on the reset to ensure it operated at 55.6 μs (the time delay that it would operate for hardware tests) verses 5.6 μs. The corrected THD measurement for the SVM algorithm without reset is 1.34% resulting in a 31% decrease.

2.   Hybrid Algorithm Simulations

Next, the hybrid algorithm developed in Chapter III was evaluated. Figure 57 shows the current waveform with the harmonic content through the first 60 harmonics for the hybrid algorithm.
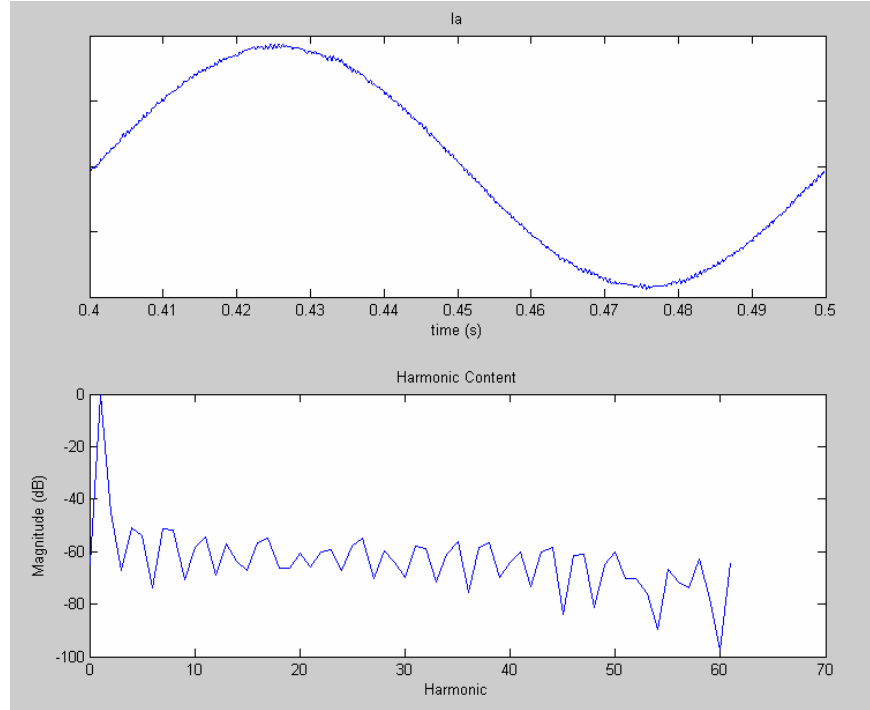
Figure 57.   Current Simulation Results for Hybrid Algorithm

The THD was calculated to be 1.00% using Matlab. As can be seen in the output waveform, there are no spikes present. This is the expected result since it is less than the result for the algorithm with spike reduction (1.34%).

When actual hardware is used, there are spikes present in the output. The spikes are the result of the time delays introduced by the A/D converters. The time delays cause latency in the commanded output states of the CMLC. The A/D converters are required to sense the bulk inverter output waveforms for the uncoupled control algorithms.

C.   HARDWARE RESULTS

With the algorithms already programmed in Simulink, HIL was implemented using interface blocks provided by dSpace. These blocks were discussed in detail in Chapter V. Figure 58 shows the overall Simulink block diagram of the system with the hardware connections while Figure 59 is a picture of the complete test setup.
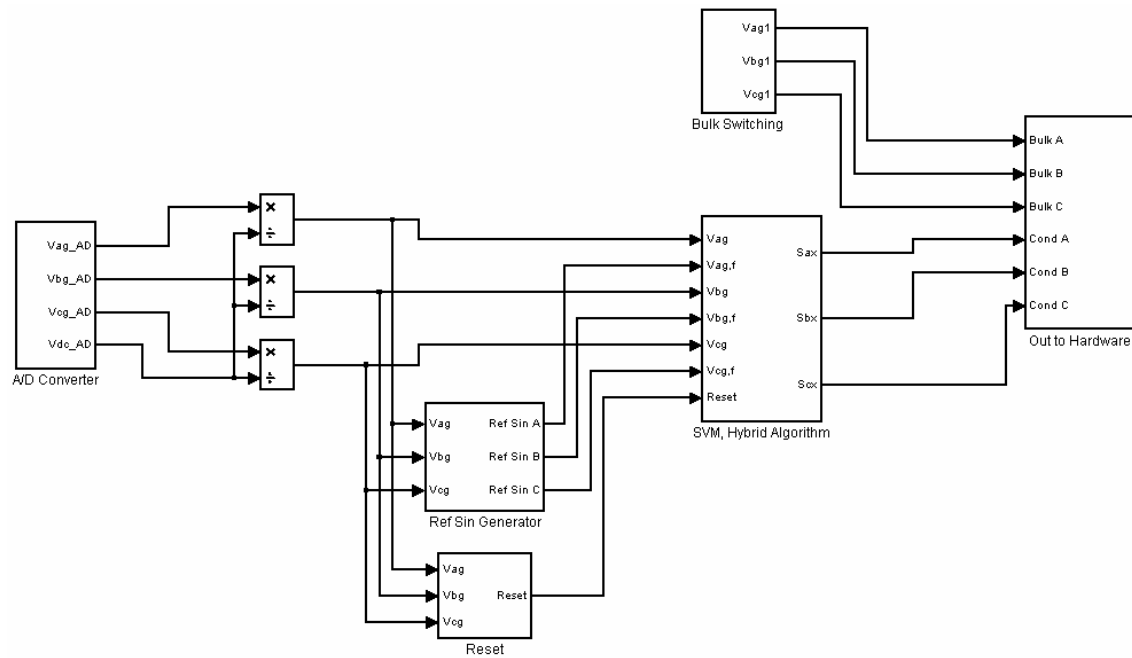
Figure 58.   Complete System with Hardware Connections

Figure 59.   Hardware Test Setup.

1. SVM Hardware Tests

Initially the tests were done using the SVM algorithm for the conditioning inverter without the reset to establish a baseline. Figure 60 shows phase-A current along with the harmonic content for the first 60 harmonics. Figure 61 shows the voltage spike width related to the bulk inverter switching.

Figure 60.   Current Total Harmonic Distortion, SVM Algorithm w/o Reset

Figure 61.   Voltage Spike for SVM Algorithm w/o Reset

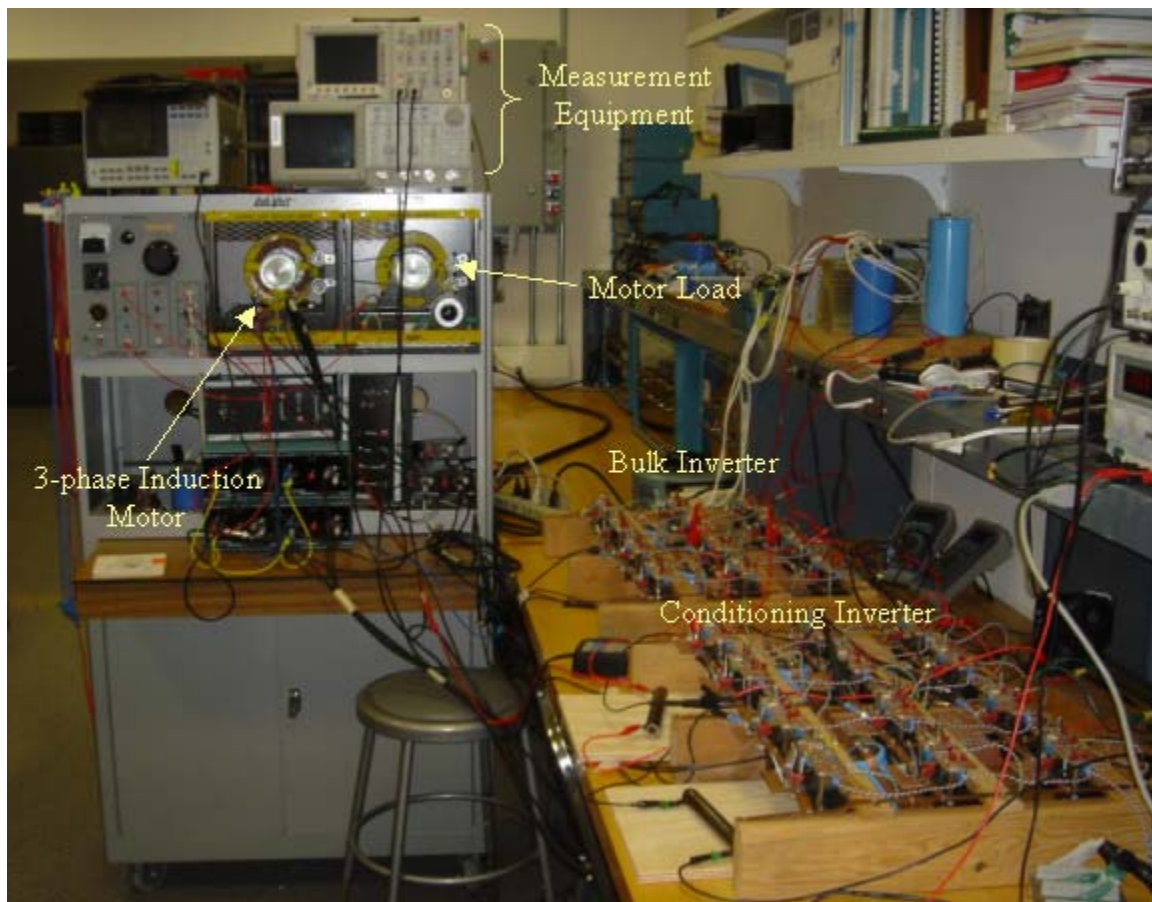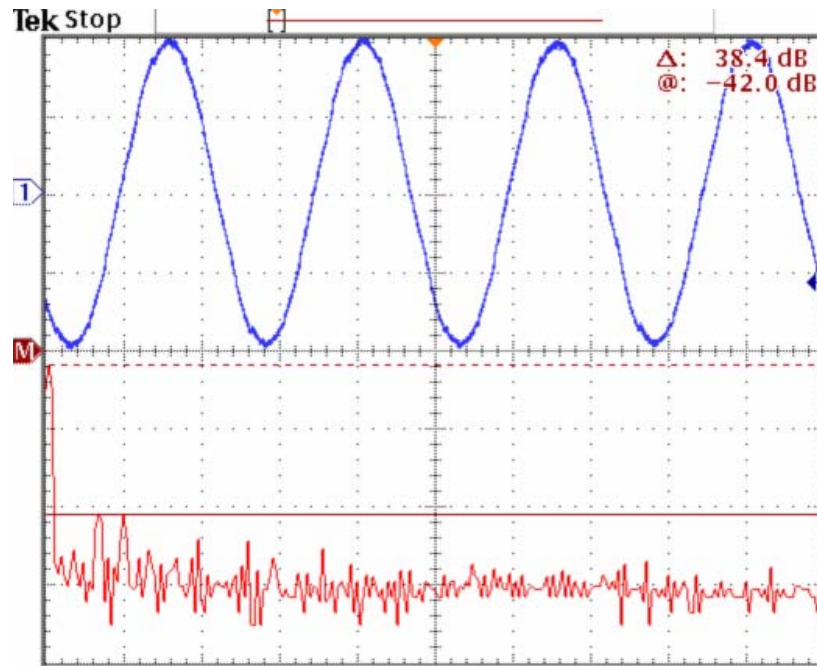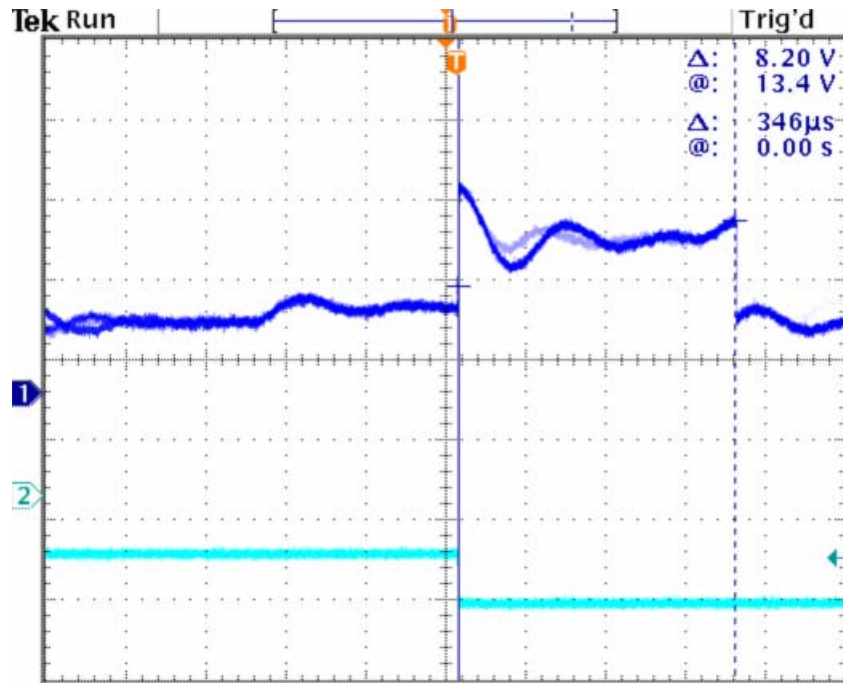By observing Figure 60, it is apparent that the difference between the highest harmonic and the fundamental is 38.4 dB (seen in the upper corner of screen capture). The total calculated THD is approximately 2.32% for the first 60 harmonics. The hardware THD data is 17% higher than the "ideal" noiseless simulation result of 1.97%. The increase was expected due to additional noise introduced by the lab environment and the use of an actual rotating machine (1/4-HP induction motor).

Figure 60 shows a spike width of 346 μs. *Waveform 1* is v_{as} while *Waveform 2* is v_{ag}. *Waveform 2* was used to trigger the oscilloscope to capture changes in the bulk inverter where the spiking occurs. Multiple samples were captured resulting in an average spike width of 357 μs. The actual width could be as long as two SVM update cycles, (555 μs, since the SVM is operating at 3.6 kHz). These results are used as a baseline for comparison with the other algorithms.

The CMLC was next tested with the conditioning inverter controlled with the SVM algorithm using the reset. Figures 62 and 63 show the current waveform along with the harmonic content and the voltage spike width, respectively.
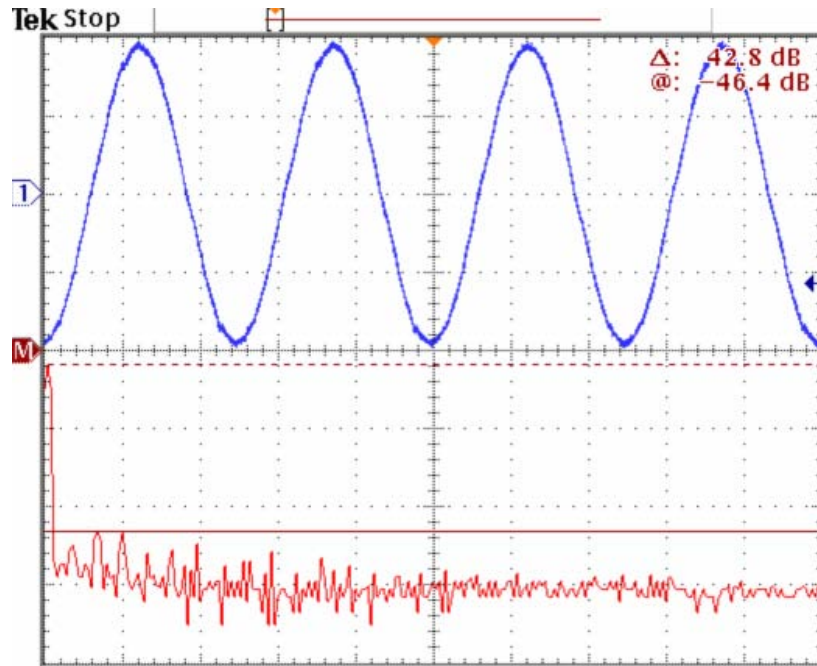
Figure 62.   Current Total Harmonic Distortion SVM Algorithm with Reset
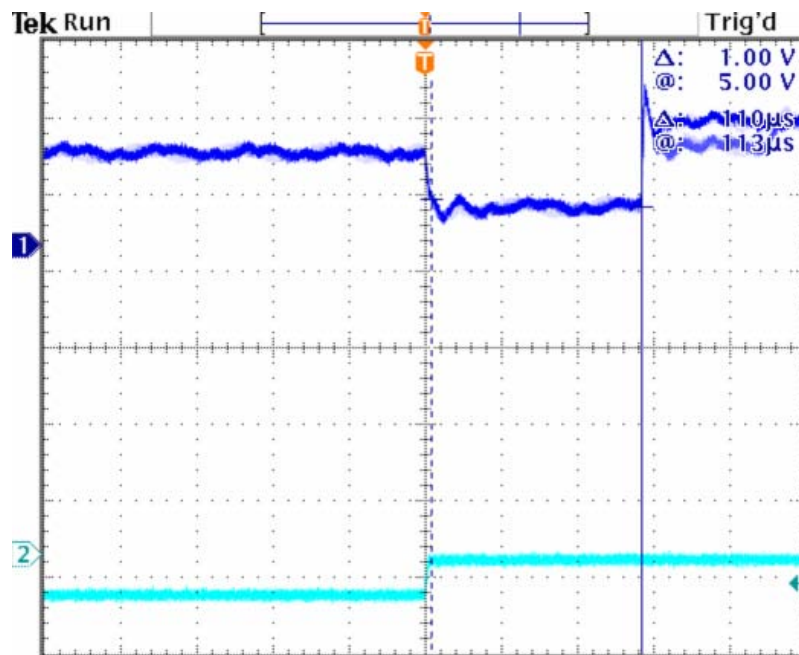
Figure 63.   Voltage Spike for SVM Algorithm with Reset

The measured THD for current was approximately 1.74%. The hardware THD was 40% higher than the "ideal" simulations. Once again this increase was expected due to additional noise introduced by the lab environment and the use of an actual rotating machine (1/4 HP induction motor). The reset reduced the THD by 25% when compared

73

to the SVM algorithm without the reset. This matched to within 20% of the 31% decrease in THD between the two algorithms for the simulation. Figure 63 shows that the spike width was reduced to 110 μs, slightly higher than the simulations, but still less than two DSP update cycles (111 μs).

2.   Hybrid Algorithm Hardware Results

After the testing of the SVM algorithms, the system was tested with the hybrid algorithm controlling the conditioning inverter. Figure 64 shows the current waveform with the harmonic content through the first 60 harmonics, and Figure 65 shows the spike width.

Figure 64.   Current THD for the Hybrid Algorithm

Figure 65.   Voltage Spike for Hybrid Algorithm

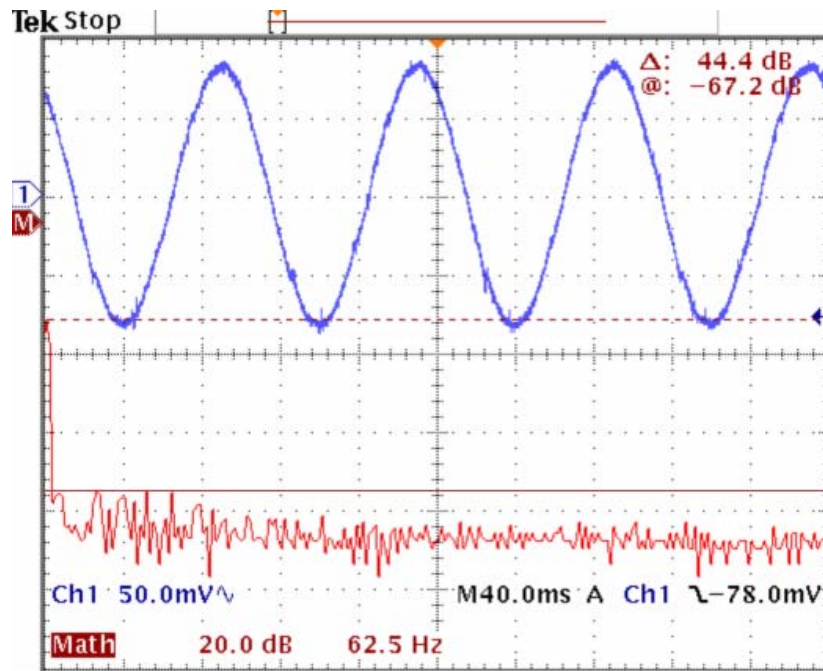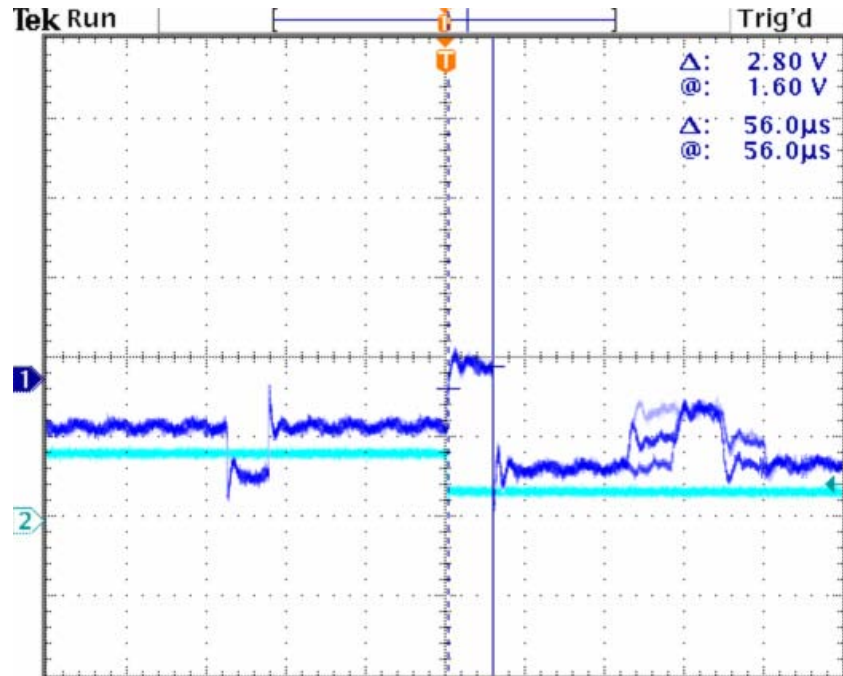The first 60 harmonics for the hybrid algorithm summed up to 1.78%. This was surprising given that the spike width was reduced to 56 μs, nearly half of what it was for the best results from the SVM algorithm (110 μs). This is probably related to the electrical noise in the laboratory. Individual harmonic measurements were found to vary by about ±1.5 dB.

After examining the steady-state response, the tracking ability of the reference sine-wave generator was analyzed. The tracking response was performed for all the algorithms with nearly identical results. Therefore, the results are only presented once. This testing was done by varying the bulk inverter frequency from 10 Hz to 20 Hz. Depending on the application, the desired tracking response can change. For instance, a ship propulsion system requires very slow tracking response due to the high mass of the propeller, thus allowing the reference sine-wave generator to use fewer updates per cycle than a lower inertial application. For this thesis, testing was done using both six updates per cycle and three updates per cycle. Figure 66 shows the results for a dynamically changing bulk inverter frequency, at a rate of 10 Hz/s, updating the frequency six times per cycle.
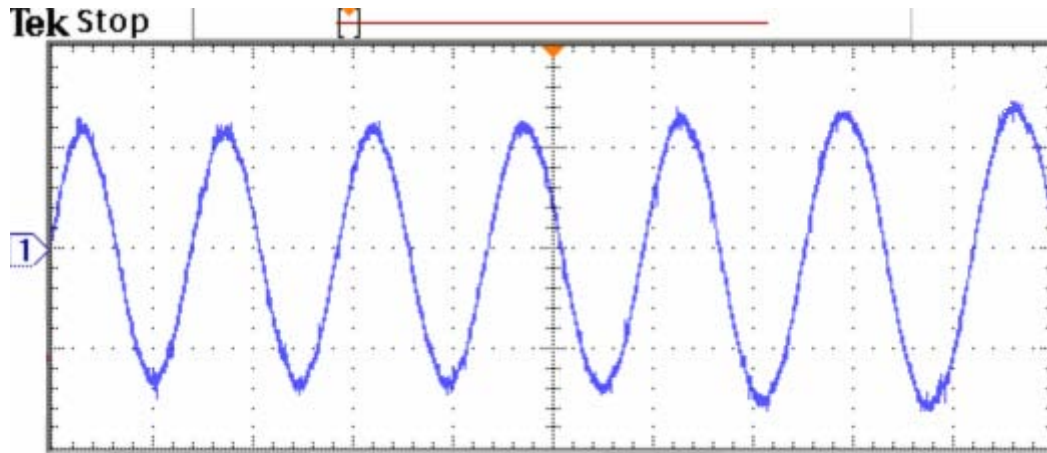
Figure 66. I_A Dynamic Response Hybrid Algorithm

Due to the changing frequency of the sine wave, THD measurements were not
appropriate. However, Figure 66 does show little to no additional distortion introduced
in the sine wave due to the varying frequency. This suggests that the reference sine wave
generator is tracking the bulk inverter frequency accurately.

D.   COMPARISON WITH SPWM ALGORITHM

A final test was done comparing the uncoupled controlled CMLC (utilizing the
hybrid algorithm to control the conditioning inverter) with the jointly controlled CMLC
(using the SPWM algorithm developed in Reference 7). The tests were run at 60 Hz (or
rated motor speed), with the motor operating at full load (of 1/4 HP). Furthermore, only
the first 20 harmonics were used to measure THD. The first 20 harmonics were used to
allow a direct comparison to the results for the joint controller achieved in Reference 7.
Since the testing was done under load, the rated motor frequency was used. The increase
in frequency from 10 Hz decreased the performance of the uncoupled controller. Since
the frequency was increased six-fold, the error associated with the reference frequency
calculations also increased six-fold. To reduce the error, the system was operated at a
higher DSP update rate. This higher rate was possible due to the fewer number of calcu-
lations required by the hybrid algorithm compared to the SVM algorithm. To help fur-
ther increase the DSP update rate, the frequency calculations were only updated three
times per cycle instead of six times per cycle as in previous tests. The update rate was
increased from 18 kHz to 30 kHz. Lastly, the switching frequency was increased to 7.2

kHz from 3.6 kHz. Figure 67 shows the results for the joint control algorithm while Figure 68 shows the results for the uncoupled control algorithm.
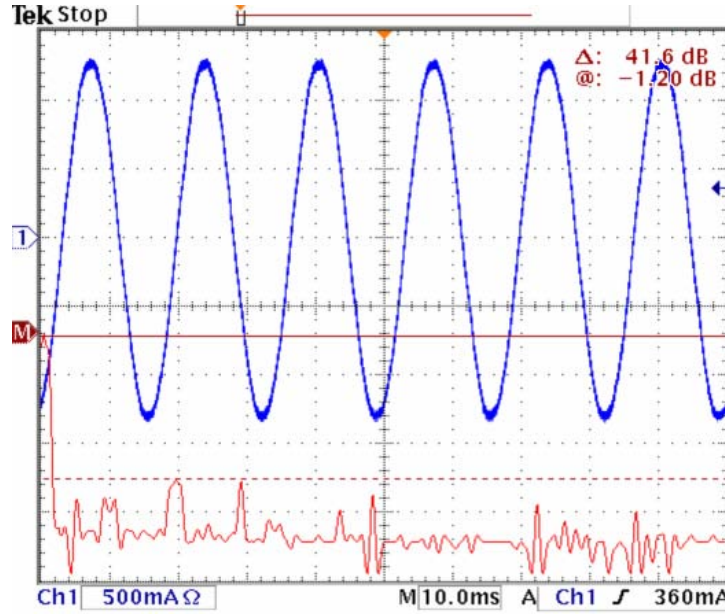

Figure 67.   Current THD for Joint Control Algorithm at 60 Hz
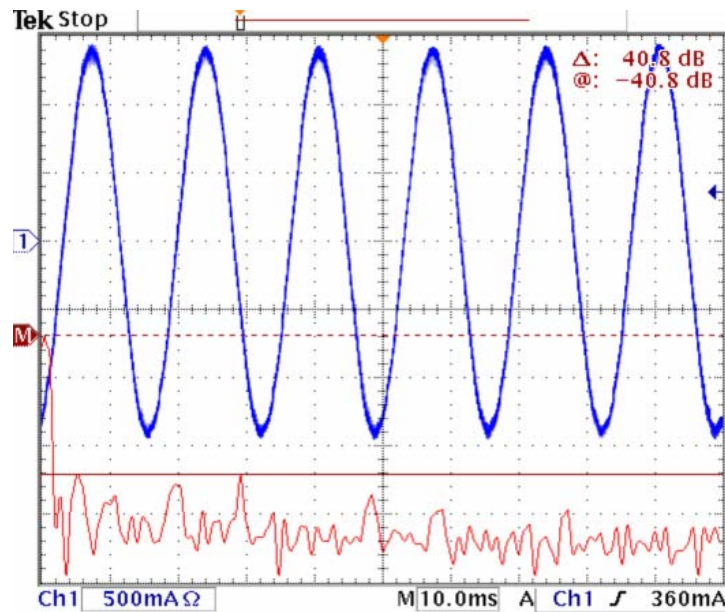

Figure 68.   Current THD for Uncoupled Control at 60 Hz

The current THD for the joint controller and uncoupled controller was 1.37% and 1.89%, respectively. By eliminating the frequency calculation errors, the THD for the uncoupled controller was reduced to 1.57%. This error elimination was done by replac-

ing the frequency calculations with a constant frequency. Figure 69 shows the THD for the uncoupled controller with the frequency calculations eliminated. Further reduction in THD can be accomplished by reducing the spike width. Unfortunately, the controller was limited to a 30-kHz update rate by the DSP. A faster DSP would reduce both the error in frequency calculations and the spike width, resulting in a lower THD for the uncoupled controller.
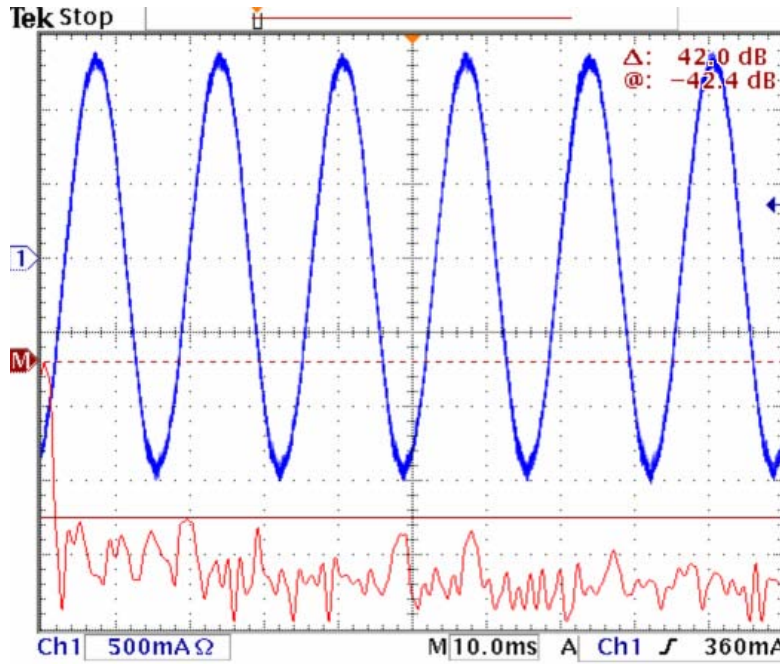
Figure 69.   Current THD for uncoupled control without frequency calculations

E. SUMMARY

Table 4 summarizes the hardware test results for the static testing. An 80% decrease in current THD was achieved by switching from a single bulk NPC inverter to the CMLC utilizing an uncoupled controller.   There was also a 25% decrease in current THD when a spike reduction technique was used in conjunction with the conditioning inverter control algorithm. The uncoupled controller was unable to match the performance of the joint controller. However, testing showed that by using a higher speed DSP, the uncoupled controller could nearly match the results of the joint controller. Since the Navy is only interested in uncoupled control for this topology, these results are promising. Chapter VII summarizes the conclusions.

Algorithm	Current THD	Voltage THD
Bulk Converter (alone)	8.28%	15.18%
Uncoupled Control: SVM algorithm w/o reset (10 Hz)	2.32%	5.93%
Uncoupled Control: CMLC SVM algorithm with reset (10 Hz)	1.74%	4.30%
Uncoupled Control: Hybrid algorithm (10 Hz)	1.78%	4.36%
Joint Control: SPWM (60 Hz, 20 harmonics)	1.37%	
Uncoupled Control: Hybrid algorithm (60 Hz, 20 harmonics)	1.89%	
Uncoupled Control: Hybrid algorithm (no frequency errors)	1.57%	

Table 4.   Summarized Hardware Test Results

THIS PAGE INTENTIONNALY LEFT BLANK

VII. CONCLUSIONS

A.   SUMMARY OF FINDINGS

The goal of this thesis was to develop an uncoupled control algorithm for the 3x3 CMLC residing at NPS. Two actual algorithms were developed. One algorithm was based on common SVM techniques with the addition of a reset while the other employed a new PWM technique based on the *g-h* transform. In addition, an ancillary technique was introduced to generate the reference sine wave from the bulk inverter output. The dSpace 1103 system was used to implement the algorithms for HIL testing.

Two variations of SVM control were used. One was a standard SVM algorithm based on the *g-h* transform. The second utilized an identical control algorithm with a reset to detect changes in the bulk inverter output changes. The spike reduction technique improved the output current THD of the system by 25% to 1.74%.

A second unique algorithm was developed to take advantage of the properties of the *g-h* transform. This hybrid algorithm worked similar to a SPWM technique in that it used a triangle waveform to pulse-width modulate the switching states. However, these switching states were found by transforming the commanded voltage into the *g-h* reference frame, and then transforming them back directly into analog switching states. The use of the *g-h* transform eliminates the need to generate the third harmonic necessary for full DC bus utilization in SPWM techniques. Also, by using a triangle PWM technique, the algorithm was very responsive to changes in the bulk inverter output state, reducing the digital spiking caused by the discrete nature of the DSP. The hybrid algorithm showed a THD of 1.78% through the first 60 harmonics.

Finally, a simple technique was introduced to generate the reference sine wave from the bulk inverter. This greatly reduced the amount of coding necessary to implement the uncoupled control algorithm, and proved to work well even with a varying bulk inverter frequency. It is also scalable, allowing the user to update the frequency of the reference sine wave anywhere from 1 to 12 times (for a 3x3 CMLC) during a single cycle. Another benefit of this technique is the ability to determine the maximum calculated frequency error, as it is directly related to the DSP update rate. This means that the accu-

racy improves with the speed of the DSP or the reduction in commanded output frequency.

The research conducted for this thesis is beneficial for future naval development of the *All-Electric Ship*. As the need for higher power high fidelity drives increases, the CMLC with uncoupled control offers significant benefits over existing topologies. These improvements include:

- high power density and low cost due to the use of a COTS bulk converter with no modifications,
- high fidelity due to the use of a small specially designed conditioning converter, and
- high reliability due to system redundancy by having two converters.

B.   FUTURE WORK

The navy is moving towards the *All-Electric Ship*. In order to remain part of this paradigm shift, NPS needs to expand research in the area of high-power, high-fidelity drives. This includes further research into CMLC. Future research might include:

- removing the secondary power supply,
- constructing a high power CMLC,
- constructing a higher-level CMLC, and
- implementing algorithms on higher speed DSPs.

LIST OF REFERENCES

[1]   Robert W. Ashton, Thomas H. Fikse, Joseph R. Sullivan, and Thong N. Ly, "An Assessment of Industry-Based High Power Electronic Modules for Naval Use," Naval Surface Warfare Center, Carderock Division, Technical Report No. NSWCCD-984-TM-2003/24, 2003

[2]   K. A. Corzine, M.W. Wielebski, F.Z. Peng, and J. Wang, "Control of Cascaded Multi-Level Inverters," *Proc. IEEE Electric Machines and Drives Conference, Vol. 3*, pp. 1549-1555, 2003.

[3]   M. Collins, "DD(X) IPS revolution in shipboard power," NAVSEA PEO-510 Internal Presentation, February 2003.

[4]   Alstom, "Mermaid Pods," [http://www.alstom.com/static/html/acom-AGF_NavPage-NavPage_StandardLeft_1069324214761.html], last accessed March 2005.

[5]   Tom Fiske, private conversation at Naval Postgraduate School Power Systems Lab, 2 May 2005.

[6]   K.A. Corzine, "Operation and Design of Multilevel Inverters," Developed for the Office of Naval Research, December 2003.

[7]   Jacob L. Barlow, *Hardware-In-The-Loop Control of a Cascaded Multi-LEVEL Converter*, Master's thesis, Naval Postgraduate School, Monterey, California, 2003.

[8]   R. Krishnan, *Electric Motor Drives Modeling, Analysis, and Control*, pp. 209-212, Prentice Hall, Englewood Cliffs New Jersey, 2001.

[9]   Zhong Du, Leon M. Tolbert, and John N. Chiasson, "Modulation Extension Control for Multilevel Converters Using Triplen Harmonic Injection with Low Switching Frequency," presented at the 2005 Applied Power and Electronics Conference, Austin, March 2005.

[10]   Quiang Song, Wenhua liu, GanguiYan, and Yuanhua Chen, "DSP-Based Universal Space Vector Modulator for Multilevel Voltage Source Inverters," *Proc. 29th Annual Conference of the IEEE*, Vol. 2, pp 1727-1732, Nov. 2003.

[11]   G. Carrara, S. Gardella, M. Marchessoni, R. Salutari, andG. Sciutto, "A new Multilevel PWM Method: A theoretical analysis," *IEEE Trans. Power Electronics*, Vol. 7, No. 3, pp. 497-505, July 1992.

[12]   J. K. Steinke, "Control strategy for a three phase AC traction drive with a 3-level GTO PWM inverter," *Proc. IEEE Power Electronics Specialists Conference*, Vol. 1, pp. 431-438, April 1988.

[13]   DSPACE, "Solutions for Control," Company Product Catalogue, 1997.

[14]   DSPACE, "DS1103 PPC Controller Board," Company Technical Sheet, 2003.

[15]   DSPACE, "Connector and LED Panels for Single-Board Hardware," Company Technical Sheet, 2003.

[16]   United States Coast Guard, "USCGC Healy," [http://www.uscg.mil/-pacarea/healy], last accessed May 2005.

[17]   Nicola Celanovic, *Space Vector Modulation and Control of Multilevel Converters*, Ph. D. Dissertation, Virginia Polytech Institute, Blacksburg Virginia, 2000.

[18]   Xuan Hou, Yongdong Li, and Yongheng Liu, "A Novel General Space Vector Modulation Algorithm for Multilevel Inverter Based on Imaginary Coordination," *Power Electronics and Drive Systems*, Vol. 1, pp. 392-296, 2003.

[19]   United States Navy, "Navy Fact File – Aircraft Carriers," [http://www.chinfo.navy.mil/navpalib/ships/carriers/], last accessed March 2005.

[20]   T. Doyle, H. Stevens, and H. Robey, "An historical overview of Navy electric drive," *Naval Symposium on Electric Machines*, Newport Rhode Island, July, 1997.

[21]   Electronics Academy, "Cycloconverters and Control of Induction Motor Part-I," [http://www.e-shikshalaya.com/cyclo_file/cyclo%28part8%29.htm], last accessed April 2005.

[22]   D. Finney, "AC motor variable frequency drives-consideration of the most economic and technically viable converter power circuits for drives above 500 kW," *Proc. IEEE Colloquium on Very High Power Converter Devices and Applications*, pp. 6/1-6/4, December 1988.

INITIAL DISTRIBUTION LIST

1.   Defense Technical Information Center
        Ft. Belvoir, Virginia

2.   Dudley Knox Library
        Naval Postgraduate School
        Monterey, California

3.   Chairman, Code EC
        Department of Electrical and Computer Engineering
        Naval Postgraduate School
        Monterey, California

4.   Robert Ashton, Code EC/Ah
        Department of Electrical and Computer Engineering
        Naval Postgraduate School
        Monterey, California

5.   Alexander Julian, Code EC/Ah
        Department of Electrical and Computer Engineering
        Naval Postgraduate School
        Monterey, California